DESIGN OF A TOUCH TRIGGER PROBE FOR A COORDINATE MEASURING MACHINE

A THESIS SUBMITTED TO
THE GRADUATE SCHOOL OF NATURAL AND APPLIED SCIENCES
OF
MIDDLE EAST TECHNICAL UNIVERSITY

BY

EMRE KARUÇ

IN PARTIAL FULFILLMENT OF THE REQUIREMENTS
FOR
THE DEGREE OF MASTER OF SCIENCE
IN
MECHANICAL ENGINEERING

DECEMBER 2007

Approval of the thesis:

DESIGN OF A TOUCH TRIGGER PROBE FOR A COORDINATE MEASURING MACHINE

submitted by **EMRE KARUÇ** in partial fulfillment of the requirements for the degree of **Master of Science Mechanical Engineering, Middle East Technical University** by,

Prof Dr. Canan ÖZGEN ____________________
Dean, Graduate School of **Natural and Applied Sciences**

Prof Dr. Kemal İDER ____________________
Head of Department, **Mechanical Engineering**

Asst. Prof. Dr. Melik DÖLEN ____________________
Supervisor, **Mechanical Engineering Dept., METU**

Examining Committee Members:

Prof. Dr. S. Engin KILIÇ ____________________
Mechanical Engineering Dept., METU

Asst. Prof. Dr. Melik DÖLEN ____________________
Mechanical Engineering Dept., METU

Asst. Prof. Dr. Yiğit YAZICIOĞLU ____________________
Mechanical Engineering Dept., METU

Asst. Prof. Dr. A. Buğra KOKU ____________________
Mechanical Engineering Dept., METU

Assoc. Prof. Dr. Veysel GAZİ ____________________
Electric and Electronics Engineering Dept., TOBB ETU

Date: 05.12.2007

I hereby declare that all information in this document has been obtained and presented in accordance with academic rules and ethical conduct. I also declare that, as required by these rules and conduct, I have fully cited and referenced all material and results that are not original to this work.

Name, Last name : Emre KARUÇ

Signature :

ABSTRACT

DESIGN OF A TOUCH TRIGGER PROBE FOR A COORDINATE MEASURING MACHINE

KARUÇ, EMRE
MS., Department of Mechanical Engineering
Supervisor : Asst. Prof. Dr. Melik DÖLEN

December 2007, 173 pages

Coordinate Measuring Machines (CMMs) have been widely used in industry in order to determine the form / dimensional tolerances of workpieces with very complicated geometrical shapes. Therefore, CMM is an important tool during the manufacturing and quality control phases. Workpiece to be measured on a CMM is probed via touch trigger probe through its stylus tip. In other words, by virtue of the touch trigger probes CMM can acquire the dimensional data of the workpiece that is to be measured. Therefore the probe has become the most vital and fundamental part of the CMM. In this thesis, a novel type of touch trigger probe / scanning probe is proposed. The proposed probe can also be used as a scanning probe for different applications. The main purpose of this thesis is to develop a novel type of touch trigger / scanning probe that has different kinematic stage and sensing stage than the other probes currently used in the industry. Giant Magnetoresistive (GMR) sensors are used for building the sensing stage of the proposed probe. GMR sensors are selected due to their outstanding sensitivity to small disturbances. Furthermore, in order to test the proposed probe; an anvil gauge setup is designed and proposed in this study. Finally, proposed probe is tested on a three-axis computer controlled electrical discharge machine (EDM), and the results acquired from those experiments are discussed.

Keywords: Coordinate Measuring Machine (CMM), Touch-Trigger Probe, Measurement Probe, Probe Performance, GMR.

ÖZ

KOORDİNAT ÖLÇME TEZGAHI İÇİN DOKUNMATİK SONDA TASARIMI

KARUÇ, Emre
Yüksek Lisans, Makina Mühendisliği Bölümü
Tez Yöneticisi : Yrd. Doç. Dr. Melik DÖLEN

Aralık 2007, 173 sayfa

Günümüzde Koordinat Ölçme Makinaları, karmaşık geometriye sahip iş parçalarının form ve boyutsal toleranslarının belirlenmesinde oldukça yoğun bir şekilde kullanılmaktadırlar. Bu sebepten dolayı Koordinat Ölçme Makinaları hem üretim hem de ölçüm süreçleri boyunca büyük bir önem arz etmektedirler. Boyutsal olarak ölçüsü alınmak istenen bir iş parçası dokunma tetiklemeli sonda ile incelenebilir ve ölçüleri elde edilebilir. Başka bir deyişle, dokunma tetiklemeli sondalar sayesinde Koordinat Ölçme Makinaları, ölçülecek olan herhangi bir iş parçasının boyutsal olarak ölçüm değerlerini verebilirler. Bu nedenledir ki, bu tür sondalar Koordinat Ölçme Makinalarının en temel ve en önemli aksesuarları haline gelmişlerdir. Bu tezde alışılmışın dışında olan, dokunma tetiklemeli / ölçüm sondası tasarlanıp önerilmiştir. Aynı zamanda önerilen bu sonda değişik uygulamalar için de tarama amaçlı sonda olarakta kullanılabilir. Bu tezin ana amacı ise, günümüzde endüstride sıkça kullanılan dokunma tetiklemeli sondalardan daha farklı bir yapısı ve algılama mekanizması olan, alışılmışın dışında olan bir sonda geliştirmektir.

Tasarlanan sondanın algılama mekanizması için Dev Manyetik Direnç etkisiyle çalışan algılayıcılar kullanılmıştır. Bu tezde Dev Manyetik Direnç etkisiyle çalışan algılayıcıların kullanılmasındaki ana sebep ise, önemsiz sayılabilecek bir harekete göze çarpan bir şekilde tepki vermeleridir. Bunun yanında, önerilen sondanın test edilebilmesi için de bir test tertibatı tasarlanıp üretilmiştir. Sonunda, bu tezde önerilen sonda üç ekseni bilgisayar tarafından kontrol edilen bir elektro erozyon tezgahı üzerinde incelenmiş ve bu deneyler sonucu elde edilen değerlerde tartışılmıştır.

Keywords: Koordinat Ölçme Makinaları, Dokunma Tetiklemeli Sonda, Ölçüm Sondası, Sonda Performansı, Dev Manyetik Direnç.

ACKNOWLEDGMENTS

Many people made valuable contributions to this thesis. First among them, a very special thanks goes out to my thesis supervisor Asst. Prof. Dr. Melik Dölen, without his effort, motivation, guidance, advice, criticism, insight and encouragement throughout three years, I would not have considered completing my graduate research. His early comments shaped the structure of whole thesis and his insightful final editing strengthened the flow of the thesis. I doubt that I will ever be able to convey my appreciation fully, but I owe him my eternal gratitude. I would like to thank the other members of my committee, Prof. Dr. S. Engin KILIÇ, Asst. Prof. Dr. A. Buğra Koku, Asst. Prof. Dr. Yiğit Yazıcıoğlu, and Assoc. Prof. Dr. Veysel Gazi for the assistance they provided.

I wish to thank Mr. Ahmet Gönüllü and Mr. Mehmet Emin Aydoğan of MAKİM for their helpful suggestions and discussions, taking time out from their busy schedule, technical and financial support and allowing me to use the 3-axis computer controlled Electrical Discharge Machine (EDM) throughout the experimental phases of my research and also I wish to thank Mr. Asım Gökbulut of GÖKBULUT MAKİNE for his willingness to manufacture the designed probes and anvil gauge setup without encountering any problems.

I would also like to thank my family for their endless love, financial support, patient support, trust, and encouragement.

In conclusion, I recognize that this research would not have been possible without the financial assistance of Asst. Prof.Dr. Melik Dölen and Makim Machinery Industry Ltd. Co (Ankara).

TABLE OF CONTENTS

ABSTRACT.. iv

ÖZ.. vi

ACKNOWLEDGEMENTS.. viii

TABLE OF CONTENTS... ix

LIST OF TABLES... xii

LIST OF FIGURES... xiii

LIST OF SYMBOLS... xviii

CHAPTERS

1. INTRODUCTION.. 1

2. REVIEW OF THE STATE OF THE ART…………………………………... 4

2.1 Introduction……………………………………………………………. 4

2.2 Fundamentals of Probing……………………………………………. 5

2.3 Probing Process…………………………………………………….... 5

2.4 Requirements for Probing Systems ………………………………... 6

2.5 Principles for Measuring Probing Systems…………………………. 7

2.6 Principles for Touch Trigger Probing Systems……………………... 7

2.7 Kinematic Resistive Probe Structure………………………………... 8

2.7.1 Kinematic Resistive Probe Working Principle………………. 9

2.7.2 Electrical Switching …………………………………………. 10

2.8 Strain Gauge Probe Technology……………………………………. 11

2.8.1 Measuring Contact Force…………………………………….. 12

2.8.2 Rejection of False Triggers…………………………………... 13

2.9 Optical Probe Systems……………………………………………… 16

2.10 Analog Scanning Probes…………………………………………... 17

2.11 Laser Probes……………………………………………………….. 21

2.12 Future Challenges in Coordinate Metrology………………………. 22

2.13 Giant Magnetoresistive (GMR) Effect 23

2.14 Use of Giant Magnetoresistors (GMR) in Hard Drive
Read Head………………………………………………………… 25
2.15 Giant Magnetoresistive (GMR) Materials…………………………... 31
2.16 GMR sensors……………………………………………………… 35
2.17 Application Areas of the GMR Sensors …………………………….. 40
2.18 Conclusion ……………………………………………………….. 43
3. GMR SENSOR CHARACTERISTICS ……………………………………... 44
3.1 Introduction……………... 44
3.2 Results of GMR Sensor Tests with Disc Magnets …………………… 47
3.3 Conclusion……………………..…………………………………... 50
4. PROBE DESIGNS………………………………………………………… 52
4.1 Introduction………... 52
4.2 Major Probe Design–1……………………………………………... 52
4.3 Major Probe Design–2……………………………………………... 58
4.4 Alternative Probe Design–1………………………………………... 59
4.5 Alternative Probe Design–2………………………………………... 60
4.6 Alternative Probe Design–3………………………………………... 62
4.7 Alternative Probe Design–4………………………………………... 64
4.8 Alternative Probe Design–5………………………………………... 66
4.9 Finite Element Analysis of Spring Plates…………………………….. 68
4.10 Finite Element Modeling of Probe…………………………………... 85
4.11 Verification of FEA Results ………………………………………… 91
4.12 Manufacturing Process………………………………………………. 93
4.13 Conclusion ………………………………………………………….. 94
5. ANVIL GAUGE DESIGNS…………………………………………………. 95
5.1 Introduction…………………………………………….................... 95
5.2 Major Design.. 95
5.3 Alternative Design…………………………………………………… 97
5.4 Calibration Results of the Major Anvil Gauge Design……………….. 98
5.5 Manufacturing Process……………………………………………….. 101
5.6 Conclusion……………….…………………………….................... 101
6. KINEMATIC MODEL……………………………………………………. 103

6.1 Kinematical Model of The Probe ………………………………………. 103
6.2 Calculation of Stylus Displacements…………………………………. 109
6.3 Conclusion ………………………………………………………………… 112
7. PROBE INTERFACING…………………………………………………….. 114
7.1 GMR Signal Processor……………………………………………… 114
7.2 Conclusion …………………………………………………………….. 119
8. EXPERIMENTS and RESULTS ……………………………………………. 120
8.1 Introduction……………………………………………………………. 120
8.2 First Probe Tests…………………………………………………….. 124
8.3 First Probe Test Results…………………………………………....... 125
8.4 Second Probe Tests…………………………………………………. 140
8.5 Second Probe Test Results………………………………………….. 141
8.6 General Specification of EDM 145
8.7 Conclusion …………………………………………………………….. 145
9. CONCLUSION AND FUTURE WORK…………………………………….. 147
APPENDICES
A. SOURCE CODE OF THE PROBE'S FIRMWARE……………………. 150
B. DATA SHEET OF GMR SENSORS…………………………………… 153
B.1 Characteristics of AA type GMRSensors……………………… 153
C. MATLAB DOCUMENTS OF THE KINEMATIC MODELS OF THE PROBES………………………………………………………………… 156
C.1 M-File Program of the Kinematic Models of the Probes………… 156
D. FIRST PROBE TEST RESULTS…………………………….............. 158
E. SECOND PROBE TEST RESULTS………………………….............. 165
REFERENCES……………………………………………………………….. 168

LIST OF TABLES

Table 2.1 Comparison of the Kinematic Resistive and Strain Gauge Probes............ 16
Table 4.1 Results obtained from the analysis 69
Table 4.2 Results obtained from the analysis (Contact Force [0.2 N] in X direction).. 74
Table 4.3 Results obtained from the analysis (Contact Force [0.2 N] in Y direction….. 77
Table 4.4 Results obtained from the analysis (Contact Force [1 N] in Z direction ... 81
Table 4.5 Mechanical properties of the probe system... 86
Table 4.6 Results of the first test.. 88
Table 4.7 Results of the second test.. 90
Table 8.1 Table of results at equator.. 138
Table 8.2 Table of results below equator... 139
Table 8.3 Table of results.. 144
Table A.1 C source code of the probe's firmware 150
Table B.1 Magnetic Characteristics 154
Table B.2 General Characteristics.. 154
Table C.1 MatLab source code of the kinematical model 156

LIST OF FIGURES

Figure 2.1 Kinematic Resistive Probe structure.. 8
Figure 2.2 Generation of the trigger in Kinematic Resistive Probe............................. 9
Figure 2.3 Electrical circuit through kinematics and the close up view of the contact patch…..... 10
Figure 2.4 The TP 20 Touch trigger probe by Renishaw... 11
Figure 2.5 Strain Gauge mounted in to the probe body 12
Figure 2.6 Strain Gauge probe measuring the contact force 13
Figure 2.7 Evaluation of the signal 14
Figure 2.8 Various types of touch trigger probes.. 15
Figure 2.9 Compact strain gauge probe by Renishaw... 15
Figure 2.10 Optical Touch trigger probe for inspection of soft materials 17
Figure 2.11 Renishaw’s SP600Q Compact Analog Scanning Probe for Small CMMs 19
Figure 2.12 Renishaw’s SP80 isolated optical metrology system 19
Figure 2.13 Renishaw SP25M probe 20
Figure 2.14 Renishaw’s SP25M patented pivoting motion systems with two diaphram springs 21
Figure 2.15 CMM Laser scanning probe by Laser Design Inc. 22
Figure 2.16 GMR effect without external field... 24
Figure 2.17 GMR effect with an applied external magnetic field 25
Figure 2.18 Evolvement chart of the HDD Technology 26
Figure 2.19 Inside of a hard disk drive 28
Figure 2.20 End of the actuator arm (close up view of the Figure 2.19) 29
Figure 2.21 GMR read sensor / spin valve (close up view of the Figure 2.20) 29
Figure 2.22 Detailed structure diagram of the GMR Head assembly 30
Figure 2.23 HDD Actuator arm and GMR assembly.. 30
Figure 2.24 The GMR head in HDD 31

Figure 2.25 Relationship between the resistivity of a magnetic material and the thickness of the material 32
Figure 2.26 Cross Sectional structure of the basic GMR material 32
Figure 2.27 Spin up and spin down movement of the electrons 33
Figure 2.28 Spin States of the magnetic layers in the case of an applied external magnetic field 34
Figure 2.29 Comparison of the Conventional and magnetic sensing 36
Figure 2.30 Magnetic sensor technology field ranges 36
Figure 2.31 Typical GMR magnetic field sensor layout 39
Figure 2.32 NVE's AA00x-02 magnetic field sensor 39
Figure 2.33 GMR and a permanent magnet configuration providing the position information 40
Figure 2.34 Another GMR and a permanent magnet configuration providing the position information 41
Figure 2.35 Simple pressure sensor implementation 41
Figure 2.36 Accelerometer implementation 42
Figure 2.37 Current detection 42
Figure 2.38 Speed and direction sensing 42
Figure 2.39 Speed sensor 43
Figure 3.1 Front view configuration of the GMR sensor chip and the disc magnet .. 45
Figure 3.2 Top view configuration of the GMR sensor chip and the disc magnet 45
Figure 3.3 Configuration of two GMR sensor chip 46
Figure 3.4 Test with disc magnets 46
Figure 3.5 Another view of test with disc magnets 47
Figure 3.6 Results of GMR sensor tests with disc magnet (velocity = 20 [mm/s]) ... 47
Figure 3.7 Region of operation when GMR sensor used with disc magnet 50
Figure 4.1 Assembly of the major design-1 from different points of view 53
Figure 4.2 Inside view of the major probe design-1 53
Figure 4.3 Major Design-1 Part List-1 54
Figure 4.4 Major Design-1 Part List–2 54
Figure 4.5 The basis of the major probe designs 56
Figure 4.6 Main Probe Body 57
Figure 4.7 Top lid of the major probe designs 57

Figure 4.8 Assembly of the major design-2 from different points of view................ 59
Figure 4.9 Assembly of the alternative design-1 from different points of view........ 60
Figure 4.10 Assembly of the alternative design-2 from different points of view...... 61
Figure 4.11 Assembly of the alternative design-3 63
Figure 4.12 Close-up view of the linear adjustment system..................................... 63
Figure 4.13 Assembly of the alternative design-4 65
Figure 4.14 Close-up views of the main probe body and the carriage system........... 65
Figure 4.15 Assembly of the alternative design-5 67
Figure 4.16 Close-up view of the carriage system.. 67
Figure 4.17 The simplified model of the designed probe 86
Figure 4.18 Displacement results of the center obtained from FEA tests................. 87
Figure 4.19 Stress Tensor, Von Misses results obtained from FEA tests 89
Figure 4.20 Simulated stylus displacement values at different evaluation angles..... 89
Figure 4.21 Designed model for verification purpose 91
Figure 4.22 Top view of the analyzed model.. 92
Figure 4.23 Cantilever Beam with an end moment... 92
Figure 4.24 Max. Stress result of the FEA software... 93
Figure 5.1 Major Anvil Gauge Design.. 96
Figure 5.2 Anvil gauge design with an angled part 96
Figure 5.3 Anvil Gauge Device 97
Figure 5.4 Alternative anvil gauge design 98
Figure 5.5 Calibration data and GMR sensor-bar magnet data plot 99
Figure 5.6 Fitted Curve (n= 2) 100
Figure 5.7 Best Fitted Curve (n= 5) 100
Figure 6.1 Simplified schematic of the measurement probe................................... 103
Figure 6.2 Reference frames for kinematic analysis... 104
Figure 6.3 Axis convention... 110
Figure 6.4 Quasi-static behavior of GMR sensor 110
Figure 7.1 GMR signal processor board 115
Figure 7.2 GMR signal processor board and the probe 115
Figure 7.3 Signal conditioner for GMR A 116
Figure 7.4 Signal conditioner for GMR B 117
Figure 7.5 Signal conditioner for GMR C 117

Figure 7.6 Signal processor 118
Figure 8.1 Granite table and the marbles used for the elevator mechanism 121
Figure 8.2 Granite is put on to a metal block 121
Figure 8.3 Sensor locations and test axes of the probe 123
Figure 8.4 Spring Steel plates used in the experiments a) SS-1 b) SS-2 c) SS-3 d) SS-4 124
Figure 8.5 Test latitudes 125
Figure 8.6 SS-1 (thickness: 0.40 mm) results 127
Figure 8.7 SS-2 (thickness: 0.30 mm) results 128
Figure 8.8 SS-2 (thickness: 0.40 mm) results 128
Figure 8.9 SS-3 (thickness: 0.30 mm) results 129
Figure 8.10 SS-3 (thickness: 0.40 mm) results 129
Figure 8.11 SS-4 (thickness: 0.30 mm) results 130
Figure 8.12 SS-4 (thickness: 0.40 mm) results 130
Figure 8.13 SS-1 (thickness: 0.40 mm) results at latitude 22.5 º below equator 131
Figure 8.14 SS-1 (thickness: 0.40 mm) results at latitude 45 º below equator 131
Figure 8.15 SS-1 (thickness: 0.40 mm) results at latitude 67.5 º below equator 132
Figure 8.16 Newly defined test axes 133
Figure 8.17 SS-4 (thickness: 0.30 mm) test results after a newly defined test axes 133
Figure 8.18 SS-1 (thickness: 0.40 mm) test results after a newly defined test axes 134
Figure 8.19 SS-4 (thickness: 0.30 mm) results at latitude 22.5 º below equator 134
Figure 8.20 SS-4 (thickness: 0.30 mm) results at latitude 45 º below equator 135
Figure 8.21 SS-4 (thickness: 0.30 mm) results at latitude 67.5 º below equator 135
Figure 8.22 Tests with metal block and anvil gauge apparatus 136
Figure 8.23 Arrangement of the steel block and the anvil gauge apparatus on the granite table 136
Figure 8.24 Stylus tip is fit inside a hole on the steel block 137
Figure 8.25 Second probe mounted on EDM 140
Figure 8.26 Test Setup 140
Figure 8.27 Inside view of the second probe, bearings are used for raising the top lid……… 141

Figure 8.28 GMR sensor locations under the top lid 141
Figure 8.29 SS-4 (thickness: 0.30 mm) results 142
Figure 8.30 SS-4 (thickness: 0.30 mm) results at latitude 22.5 º below equator 143
Figure 8.31 SS-4 (thickness: 0.30 mm) results at latitude 45 º below equator 143
Figure 8.32 SS-4 (thickness: 0.30 mm) results at latitude 67.5 º below equator 144
Figure B.1 NVE’s AAxxx-02 type GMR sensors.. 153
Figure B.2 GMR Voltage vs. Applied Magnetic Field Graph 155
Figure D.1 SS-1(thickness: 0.40 mm) at equator... 158
Figure D.2 SS-2(thickness: 0.30 mm) at equator... 159
Figure D.3 SS-2(thickness: 0.40 mm) at equator... 159
Figure D.4 SS-3(thickness: 0.30 mm) at equator... 160
Figure D.5 SS-3(thickness: 0.40 mm) at equator... 160
Figure D.6 SS-4(thickness: 0.30 mm) at equator... 161
Figure D.7 SS-4(thickness: 0.40 mm) at equator... 161
Figure D.8 SS-1(thickness: 0.40 mm) at latitude 22.5 º below equator.................. 162
Figure D.9 SS-1(thickness: 0.40 mm) at latitude 45 º below equator..................... 162
Figure D.10 SS-1(thickness: 0.40 mm) at latitude 67.5 º below equator................ 163
Figure D.11 SS-4(thickness: 0.30 mm) at latitude 22.5 º below equator................ 163
Figure D.12 SS-4(thickness: 0.30 mm) at latitude 45 º below equator................... 164
Figure D.13 SS-4(thickness: 0.30 mm) at latitude 67.5 º below equator................ 164
Figure E.1 SS-4(thickness: 0.30 mm) at equator 165
Figure E.2 SS-4(thickness: 0.30 mm) at latitude 22.5 º below equator 166
Figure E.3 SS-4(thickness: 0.30 mm) at latitude 45 º below equator 166
Figure E.4 SS-4(thickness: 0.30 mm) at latitude 67.5 º below equator 167

LIST OF SYMBOLS

b	Vertical distance between centers (mm)
r	Radial distance (mm)
a	Axial distance (mm)
k	Spring coefficient of spring plates (N/m)
k_x	Spring coefficient of spring plates in x-direction (N/m)
k_y	Spring coefficient of spring plates in y-direction (N/m)
k_z	Spring coefficient of spring plates in z-direction (N/m)
F	Applied force to the stylus tip (N)
E	Modulus of Elasticity of the material (MPa)
σ_{max}	Max. stress on the beam (MPa)
M	Applied moment (N.mm)
c	distance from neutral axis to extreme fibers (mm)
I	Moment of Inertia (mm^4)
b	Width of the beam (mm)
t	Thickness of the beam (mm)
$V(x)$	Voltage Values (V)
p_i	Constants of the polynomial fitted curve
n	Degree of the polynomial
x_i	Measured displacement values (mm)
ε_x	Small angles representing the orientation wrt. x-axis (rad)
ε_y	Small angles representing the orientation wrt. y-axis (rad)
ε_z	Small angles representing the orientation wrt. z-axis (rad)
δ_x	Minute displacements about the corresponding origin of the probe (mm)
δ_y	Minute displacements about the corresponding origin of the probe (mm)
δ_z	Minute displacements about the corresponding origin of the probe (mm)
L_0	Distance between spring plate and ball center (mm)

L_1 Magnet plate holder shaft length (mm)

L_m Vertical distance between magnet plate center and bottom of the magnet plate (mm)

R_m Radius of the magnet plate (mm)

R Radius of the GMR chip positions in the main probe body (mm)

Δx Displacement along the x-axis (mm)

Δy Displacement along the y-axis (mm)

Δz Displacement along the z-axis (mm)

h Vertical distance between the centerline of GMR's and spring plate (mm)

r_A Radial displacements along A (mm)

r_B Radial displacements along B (mm)

r_C Radial displacements along C (mm)

a_A Axial displacement along A (mm)

a_B Axial displacement along B (mm)

a_C Axial displacement along C (mm)

k_1 Constant of quasi-static behavior of the sensor in the linear region (V/m)

k_2 Constant of quasi-static behavior of the sensor in the linear region (V/m)

R_v Resistance of the multi turn pots (Ω)

R_f Resistance of the passive RC circuit (Ω)

C_f Capacitor of the passive RC circuit (μF)

δ Displacement amount of the stylus tip (mm)

A Constant matrix

$\hat{x}_i$ Estimated displacement value of the stylus tip (mm)

CHAPTER I

INTRODUCTION

The goal of this thesis is to develop a novel touch-trigger / scanning probe for Coordinate Measuring Machines (CMMs). The probe developed in this study has different mechanical and sensing concept than the conventional probe design currently used in the industry.

CMMs, one of the effective metrological instruments, are widely used in most manufacturing plant to verify the geometry of a manufactured part [1]. CMMs are able to measure the position with fine resolutions (even nanometers). They provide coordinate information about part geometry as feedback of the manufacturing process, allowing for the analysis of both product and process quality. The two basic design goals of a CMM are to maximize throughput and acquire a large size of data. There are numerous configurations of CMMs, including designs that measure in polar, cylindrical, and Cartesian coordinates [2].

One of the major accessory elements of a CMM that has a vital effect on CMM's accuracy and speed is the type of probe it uses. Most recently, CMMs use passive probes (actuating device is not in the probe) that have several defects limiting their accuracy and speed. So in order to avoid those defects coming from those probes, two basic contact probe types are designed and the first type of passive probe developed is the touch trigger probe. The operation principle of touch trigger probe is to contact with the workpiece using a vector move and records the XYZ coordinate after it stops. After the establishment of the contact between the workpiece and the stylus tip of the touch trigger probe, due to the machine's inertia, probe will move in the probing direction respectively. Afterwards probe moves away from the workpiece and then goes to another location and repeats the same process in a point to point fashion in order to obtain the workpiece dimensional information [2], [3].

Since the above-mentioned technique is slow, a second type of passive probe is developed which is the contact-scanning probe. This probe is moved along the surface of the workpiece while keeping the contact between the stylus tip of the touch trigger probe and the workpiece. While it moves across the part's surface, the probe deflection is used to determine deviations in the part surface. Even though this type of probing is much faster than the touch trigger probing application, this probe is prone to errors from deflection of the probe tip [2], [4].

Furthermore, non-contact laser scanning probes have also been utilized in the industry in addition to contact scanning techniques. Laser probes greatly increase the measurement speed, but errors caused by deviations in surface reflectivity can slow down the performance [2], [5]. Another progress in CMM probe technology is the application of multi-sensor technique to CMMs. Those improved CMMs have capability to change probes (i.e.: touch trigger to laser) during measurement process, taking the advantage of each exchanged probe's performance [2], [6].

Dominantly, touch trigger probes are used on CMMs, and most of these probes utilize a kinematic seating mechanism to sense the trigger signal for the probe stylus. Since touch trigger probes are dominantly used on CMMs and machine tools for the dimensional measurement and in accordance with that a probe sometimes can be described as the heart of a CMM, they can be named as key technological advancement in coordinate metrology [7]. Therefore, in this thesis a novel type of touch trigger / measurement probe utilizing Giant Magnetoresistor (GMR) sensor technology is presented. Due to their outstanding sensitivity to a small disturbances or displacements, a GMR sensor based prototype touch trigger probe is developed.

The main contribution of this thesis is to develop a touch trigger probe that has different characteristics compared to the other probes used in the industry. The designed probe can also be used as a contact-scanning probe respectively. There are two main goals of the research presented in this thesis. The first goal is the development a novel type of touch trigger probe utilizing GMR sensor technology; a prototype probe; and an experimental setup. This work will serve as a basis for the analysis of the probe. The second goal is to experimentally verify that such probe can also be used in the measurement processes.

The organization of this thesis is as follows: Chapter 2 describes the state of the art in the relevant fields. Chapter 3 focusses on the characteristics of the GMR sensor. The major probe design, alternative designs, and the results of the finite element analysis of the proposed probe are presented in Chapter 4. An experimental setup; anvil gage design, for the tests of the GMR sensor and the probe is presented in Chapter 5. The electronic interface for the probe is described in Chapter 6. In Chapter 7, probe, models, and analysis are presented. In Chapter 8, performed experiments and the obtained results are presented. Finally, in Chapter 9 future works and conclusions are described.

CHAPTER 2

REVIEW OF THE STATE OF THE ART

2.1 Introduction

Measurement is an essential process of our every day lives. Looking back over the evolution of measurement, one can easily find out that it is directly correlated to the progress of humankind since breakthroughs in industrial metrology directly contribute to the advancements in manufacturing field [1].

Dimensional parameters represent vital quality characteristics of workpieces. Therefore, the measuring action for testing compliance of those characteristics includes the important sub-process of probing the workpiece's related surface. In accordance with the particular needs encountered during the measurement processes, different types of probing systems for different measurement tasks have been developed [8].

Moreover, CMM supplementary elements are the most vital part of the whole measuring system dramatically. Correct selection and use of those auxiliary elements can extremely improve the measuring capability of CMMs. Standard supplementary elements include devices such as probe changers, non-traditional probes, touch trigger probes, temperature compensation, rotary tables, programmable fixtures and part handling apparatuses. All of these previously mentioned systems have a significant role in determining the CMM performance [1].

The probe system, itself is one of the fundamental elements of the CMM dramatically. The probe system of CMM including the probe and stylus is the most fundamental part of the whole system. Thus, due to its function in the measuring procedure, it also causes larger errors than other parts of the CMM [9].

2.2 Fundamentals of Probing

Measuring the length of a workpiece is comparing the distance between two points on the surface of the workpiece with a standard length [8], [10]. Geometrical quantities to be measured on a workpiece apply to distances and positions of chosen measured points on the surface of the workpiece. For that reason, probing the desired point on the surface with a sensing element via touching (stylus tip) or by sensing it in a non-contact fashion is necessary. Therefore, the probe is one of the critical components of the CMM and is responsible for the total accuracy of a measurement task. Most commonly used probes for the probing tasks are tactile and optical probing systems. Their working principal is based on mechanical interactions with the measured workpiece [8], [11], [12], [13].

2.3 Probing Process

The measurement process can be classified into four successive tasks; positioning, probing, measuring and evaluating.

- Positioning is to bring the workpiece into the measuring range of the probing system. Actually, during this task the probe system is moved in order to determine the safe zone to avoid the crash of the workpiece and the probe [8], [14].
- Probing is to make the physical contact between the touching element (i.e.: stylus tip) and the surface of the workpiece.

- Measuring is to compare the measured dimensions to a pre-selected reference points by the measurement standards.
- Evaluation process covers the transformation of the probing system's position vector (directed from probe coordinate system to the center of the stylus ball) in to probed point's position vector (directed from machine coordinate system to the contact point established between workpiece and the stylus tip) [8].

2.4 Requirements for Probing Systems

This headline can be divided into three groups; application specific requirements, metrological characteristic and system specific properties (which also include the economic aspects). The measurement behaviour of the probing system can be described via the metrological characteristics. For different tasks, exceptional requirements on the probing system may appear.

- Application specific requirements; to perform the variety of measurement tasks the measurement system and the probing system have to fulfill some requirements come from the nature of measurement process. (i.e.: scanning or discrete point probing mode, probing force reaction, accessory elements, articulations, and weight of the probing systems).

- Metrological characteristics define the possible quality of the results measured with particular system.(i.e.: reproducibility, response characteristic without backlash and with high sensitivity, pretravel and overtravel).

- System specific properties defines the costs, time and additional equipment needed for performing measurements for a given probe.(weight, size, applicability with certain CMM) [8].

2.5 Principles for Measuring Probing Systems

The heart of a measuring probing system is a length measurement transducer with a quite small measuring range. Measuring tactile probes are able to obtain data without stopping while they are moving; which is called three-dimensional scanning. In consideration of application in measuring probing systems, physical effects with a linear responses are held in high regard [16].

2.6 Principles for Touch Trigger Probing Systems

After the invention of touch-trigger probe in 1970s, these devices have become the main component of CMMs and machine tools. The touch-trigger probe can also be called as a switching probe or touch probe respectively. Most of the touch trigger probes utilize a kinematic seating arrangement for the stylus (Figure 2.1). The tripod mechanism, which also functions as the stylus holder, is seated on this kinematic arrangement. The tripod can be distorted when a force is applied to the stylus tip. Each tripod (rod) leg is supported by a kinematic seat with two balls. On the other hand, other probe designers use cylinders to replace balls in the kinematic seating arrangement. A preload spring is put on top of the tripod to create a force to make the tripod sit at the rest position before and after the interaction between the stylus tip and the workpiece during the measurement task. The probe tip at the end of the stylus shaft contacts the workpiece in the coordinate measurement process. The probe tip is usually a ruby ball with high quality sphericity [17].

For the measurement task on a computer-controlled machine, the probe is directed to approach the workpiece at a constant speed when it comes within the probe approach distance (safe zone). Before the mechanical interaction between the stylus tip and the workpiece, the tripod structure is held in its rest position via the spring. Due to this kinematic arrangement, there will not be any generated trigger signal when the probe tip initially contacts with the workpiece. After the first contact is achieved, the probe will continue to move along the probing direction so the probing force will increase respectively. When the force is large enough to tilt the tripod and cause a physical quantity to reach a threshold (voltage) setting. Actually, this behaviour is not only due to the design of the probe system, more importantly the machine's inertia plays an important role for the travel of the stylus tip after the first contact is achieved. A trigger signal is generated when the physical quantity exceeds a threshold in the sensing system. The trigger signal is used by the CMM or machine tool to lock the position counters or transducers to record the point coordinates at the trigger instant [17], [18].

2.7 Kinematic Resistive Probe Structure

The basic requirements for a touch-trigger probe are:

- Conformance so that the stylus deflects when it meets the surface of the workpiece, applies a low force to the component and allows time for the machine to decelerate before backing off the surface.
- Mechanical repeatability so that the stylus always returns to the same location relative to the machine quill / spindle when it is not in contact with the part.
- Electrical repeatability so that the probe always triggers at the same stylus deflection in any particular direction [17].

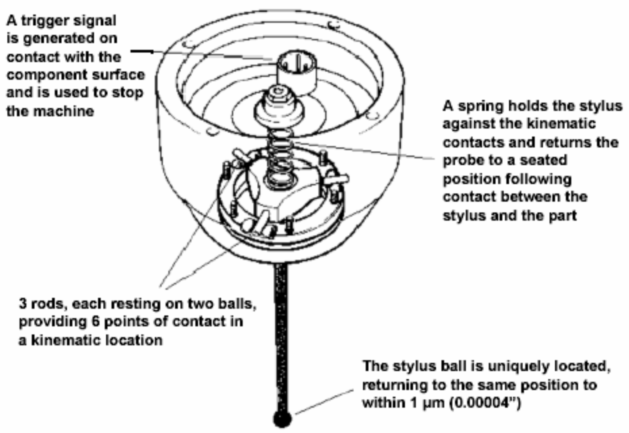

Figure 2.1 Kinematic Resistive Probe structure [19]

The contact elements are made of tungsten carbide, a very hard and stiff material, to provide that the contact zones are very small. An electrical circuit runs through the contacts, and it is the resistance through this circuit that is measured by the probe's electronics [17].

2.7.1 Kinematic Resistive Probe Working Principle

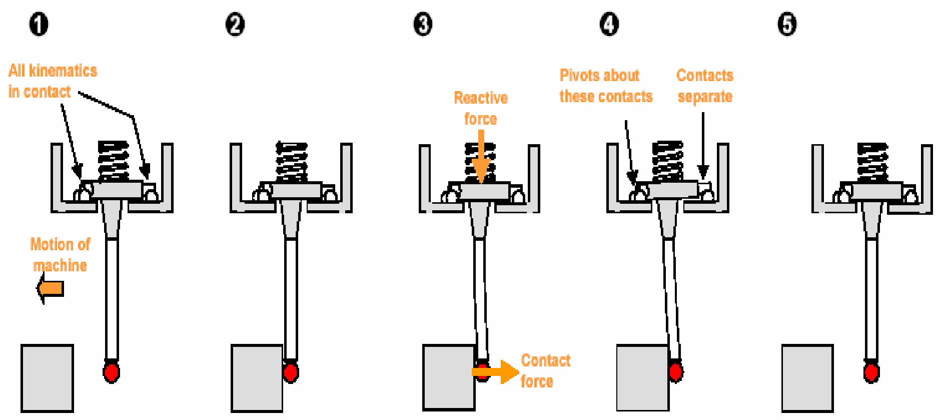

Figure 2.2 Generation of the trigger in Kinematic Resistive Probe [17]

1) Probe is in the seated position and it is moving towards the workpiece,

2) First contact is established,

3) Probe's stylus still moving along the approach direction, contact force is increasing,

4) Finally, one of the tripod leg structure is held up and through the probe's electronics a trigger signal is generated,

5) Machine backs off surface and probe's stylus reseats its resting position [17], [19].

2.7.2 Electrical Switching

An electrical circuit is built through the kinematic contacts. The ball plate is isolated from the tungsten carbide spheres, while the cylinders and the stylus carrier are also insulated from one another (Figure 2.3). Wires in the ball plate carry the current between the contact patches. Due to the load of the spring, the contact elements experience elastic deformation (Figure 2.3), creating small contact areas through which the current can move along. The resistance across each contact patch is inversely related to the area of the contact patch (R = ρ/A). Due to nature of this mechanism, whilst the force between the stylus and the component is forming, the reactive moment that is generated in the probe mechanism causes the forces between some contact elements to increase, whilst the force between others will decrease. This behaviour is due to the kinematical constraints. As the force between two contact elements reduces, the contact patch area gets smaller, thus resulting an increase in the resistance between those contact elements. With all six contact patches wired in series, the contacts with the lowest force between them greatly affects the overall resistance in the probe circuit. When the resistance reaches a threshold level that is defined, the probe's output is set to triggered (Figure 2.3). Furthermore, the balls and rods are still in contact when the trigger signal is generated, so in other words the stylus is in a defined position, providing repeatable measurement task [17], [18], [19].

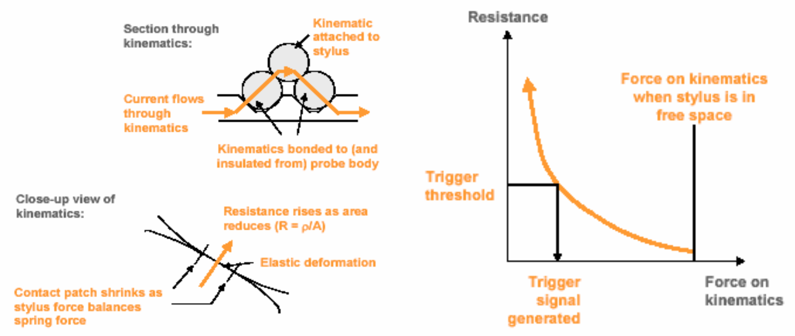

Figure 2.3 Electrical circuit through kinematics and the close up view of the contact patch [17]

Their simplicity, compact size and low cost has made kinematic resistive probes the most popular type in industrial use. Renishaw's, the TP20 is a compact 5-way, or 6-way, kinematic touch-trigger probe system. The two-piece design, comprising probe body and detachable stylus module(s), connected using a highly repeatable magnetic kinematic coupling. This provides the facility to change stylus configurations either manually or automatically without the need for requalification of the stylus tips, thereby giving significant time savings in inspection routines. Modules offering a range of trigger forces allow the probe performance to be best matched to the measurement task. A set of probe extensions is also available, as is a 6-way module. The stylus mounting thread accepts styli from the Renishaw M2 range. The TP20 system is easily retrofitted and is compatible with existing touch trigger probe interfaces, extensions, and adaptors [21].

Figure 2.4 The TP 20 Touch trigger probe by Renishaw [21]

2.8 Strain Gauge Probe Technology

A new form of sensing technology has addressed the performance limitations of the kinematic resistive probe mechanism; silicon strain gauges. This has been made possible by modern compact electronics and solid state sensing, which Renishaw has engineered for probes as small as 13 mm (0.5 in.) in diameter. Although strain gauge probes still use a kinematic mechanism to retain the stylus, they do not use the resistance through the contact elements as the means to sense a trigger. Instead, a set of strain gauges is positioned on carefully designed webs in the probe structure above the kinematics (Figure 2.5). These gauges measure the contact force applied to the stylus and generate a trigger once the strain exceeds a threshold value. This provides a low trigger force, and, since the sensing is not dependent on the kinematics, a consistent trigger characteristic in all directions [8], [17], [19].

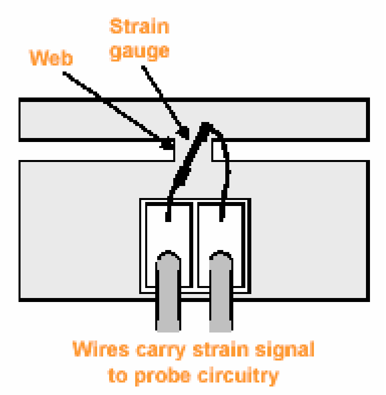

Figure 2.5 Strain Gauge mounted in to the probe body [17]

2.8.1 Measuring Contact Force

Figure 2.6 shows a schematic of a strain gauge probe. At low contact forces, the kinematics remains seated and the force is transmitted through them to the probe structure. The strain gauges – three measuring gauges aligned to sense in the X, Y, and Z-axes – are mounted on thin webs. They detect forces in the structure and their outputs are summed together so that once a force threshold is breached in any direction, a trigger signal is generated. This threshold force is typically a few grams – much lower than the trigger force on an equivalent resistive sensor. The strain gauges are highly sensitive to forces on the structure, and will detect vibrations on the machine whilst the stylus is not in contact with the surface of the part. Filtering circuitry inside the probe establishes whether the strains seen at the gauges are the result of a real and persistent deflection of the stylus. To achieve this, a short and highly repeatable delay is inserted into the detection circuit from the moment the force threshold is first breached, after which a persistent and increasing force must be seen before a trigger is issued at the end of the delay period [8], [17].

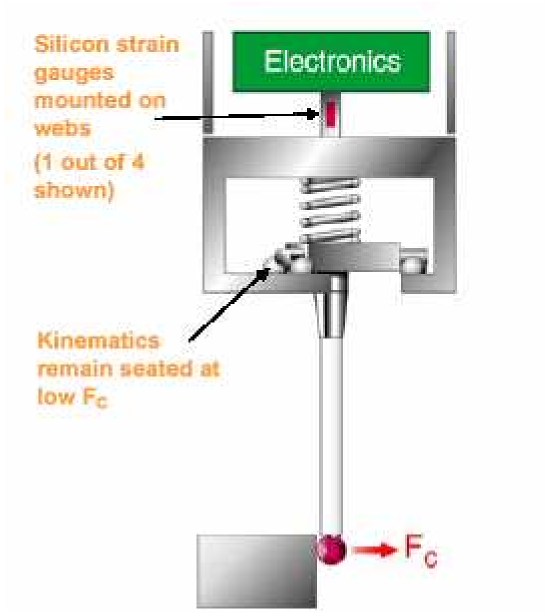

Figure 2.6 Strain Gauge probe measuring the contact force [17]

2.8.2 Rejection of False Triggers

Figure 2.7 illustrates the case where there is significant noise on the summed strain gauge output value, caused by vibration on the machine. In this case, the threshold is breached by one particular vibration and the fixed delay timer starts. However, the force drops below the threshold and remains at a lower level so that, once the delay period has expired, the electronics can identify that a real trigger has not occurred, so no trigger signal is issued. Meanwhile, Figure 2.7 also shows the case where the stylus meets the surface. Once the stylus strikes the surface, random vibrations are quickly damped out as the strain gauges measure the contact force.

The force seen at the gauges rises persistently, so that once the timer starts, the force never falls below the threshold again. At the end of the repeatable delay period, a trigger signal is issued. This repeatable delay is easily removed with probe calibration. The net effect is an apparent reduction in the radius of the stylus ball, equal to the distance moved by the machine during the fixed delay period. Provided the machine moves at a constant speed during this period, measurement repeatability is unaffected. This means that the probe must be calibrated at the same-programmed feed rate at which measurements will occur, making strain gauge probes suitable only for automated CMMs and CNC machine tools. A further consideration is the programmed target position – the point beyond the expected position of the surface towards which the machine is programmed to move during the probing cycle. Manufacturing engineers must ensure that as the machine moves towards this target position, it does not start to decelerate before the stylus meets the surface. The over-travel distance must therefore take account of both the likely variation in surface position, as well as the deceleration profile of the machine [17].

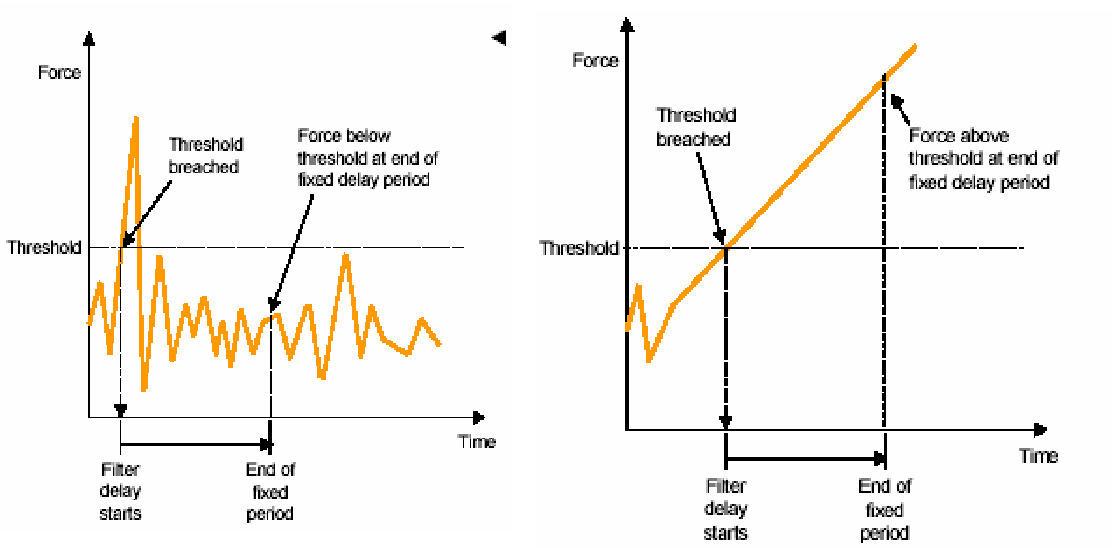

Figure 2.7 Evaluation of the signal [17]

Figure 2.8 Various types of touch trigger probes [20]

The TP200 probe uses micro strain gauge transducers to deliver excellent repeatability and accurate 3D form measurement even with long styli. The sensor technology gives sub-micron repeatability and eliminates the lobing characteristics encountered with kinematic probes. The solid state ASIC electronics within the probe ensure reliable operation over millions of trigger points. TP200 has been designed to have higher tolerance to vibration. This helps to overcome the problem of 'air' trigger generation which can arise from vibrations transmitted through the CMM or when using long styli with faster positioning speeds [22].

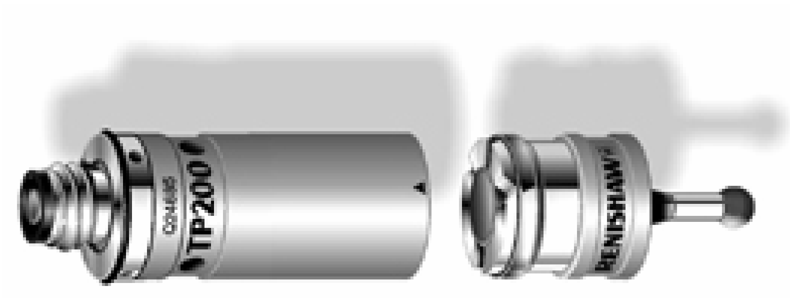

Figure 2.9 Compact strain gauge probe by Renishaw [22]

Table 2.1 Comparison of the Kinematic Resistive and Strain Gauge Probes

	Kinematic Resistive Probe	**Strain Gauge Probe**
Pros	- Simple mechanism, - Low mass (so low inertia at the triggering instant), - Cost – effective, - Easy to retrofit to all types of CMM.	- Improved repeatability, - Low and almost uniform pre-travel variations in all directions, - More accurate measurement, - Low bending deflection (leading low hysteresis), - Low trigger force (few gm.), - Support much longer styli,
Cons	- Directional dependent pre-travel variation, - Micro-degradation of contact surfaces, - Exhibit re-seat failures over time, - Limiting the length of stylus, - Resistance through the contact elements as the means to sense trigger.	- Extra mass - (filtering circuitry), - Expensive,

2.9 Optical Probe Systems

They measure by triangulation, focusing, reflecting, image processing, and combinations of these principles. The optical probe systems enable measurement of those parts which cannot be measured by contact probing or whose measurement would require a considerable effort (i.e.: films, foils, PCBs or components made of plastic materials).

The OTP6M optical trigger probe utilizes a visible laser spot (Class 2) to provide a non-contact inspection solution for use on CMMs. The system comprises a Wolf & Beck laser probe (OTP6-LD), which operates using the optical triangulation principle, and a Renishaw interface (OPI 6). OTP6M can be used to measure pliable or delicate materials as the sensing beam causes no distortion of the surface. It is easily retrofitted to standard touch trigger probe applications. It provides repeatable Z-axis measurement and has edge-triggering capability [23].

Figure 2.10 Optical Touch trigger probe for inspection of soft materials [23], [20]

2.10 Analog Scanning Probes

Analog scanning probes are a type of contact probe used to measure contoured surfaces such as sheet metal assemblies. The analog scanning probe remains in contact with the work piece surface as it moves and produces analog readings rather than digital measurements. Continuous analog scanning (CAS) is a relatively new technology. It adds versatility to CMMs by offering dramatically increased levels of data acquisition, which speeds and improves the accuracy of measurement and inspection operations. CAS technology is based on continuous rather than point-to-point acquisition of data with specialized probes and software. It is particularly useful for gauging and surface-mapping complex, contoured shapes, including crankshafts and cams, turbine engine blades and prosthetic devices. It is also suitable for inspecting the form of large sheet metal assemblies, such as automobile bodies. Continuous analog scanning systems can acquire 10 to 50 times more data than traditional touch trigger probes in a given amount of time. The added data provides users with more confidence in the measuring and inspection process. More confidence may be needed if there are large gaps between data points using point-to-point probing techniques. CAS allows users to scan irregular shapes. This is particularly valuable for measuring work piece features that change continuously, such as the arc on a turbine blade. The ability to acquire data in this manner also allows CAS systems to be used in reverse engineering applications where a new part has to be built to match or fit an existing part. Form and shape measurement require a different approach than prismatic parts measurement. CMMs used in form measurement applications must be capable of collecting large amounts of data quickly, and measurement software must be capable of processing this data accurately. Because of this, special scanning routines not found in other CMM software packages are required. For example, scanning software must have a filtering ability to distinguish between subtle changes in the surface direction and variability in the work piece surface finish, such as the rough area on a turbine blade. Filters can also eliminate the effects of vibration caused when the probe tip moves along the work piece surface. Nonscanning CMMs use probe center coordinates for measurement in that the data generated by the machine is the location of the ball's center point. In scanning applications, the data must be shifted by the radius of the probe, using the parallel curve function, to represent the real surface of the work piece. During analysis, spline functions are used to remove the mismatch between the scanned points and the nominal points. This way, deviations from the nominal to the actual can be calculated. Two types of CAS systems are used in measuring and inspection applications: closed-loop and open loop. In a closed-loop system, the probe automatically detects changes in surface direction of the part and adjusts itself to maintain contact with the part surface. Closed-loop scanning is particularly useful for digitizing unknown complex shapes. In the past, closed-loop scanning was performed at a relatively low speed, although improvements in controller technology have helped increase closed-loop scanning speeds markedly in the last five years. Five years ago, closed-loop scanning could be performed at only 10 mm/sec. New systems can perform closed-loop scanning at 50 mm/sec., with extremely high accuracy. Open-loop scanning is a high-speed data-gathering technique used with continuous analog probes on parts whose geometry is well defined by surface points and vectors, or CAD data. The CMM drives the probe along a path using dimensional information from a data file. An example would be a sheet metal assembly such as an automobile hood. The probe head is driven along a vector perpendicular to the nominal surface and records the magnitude of the error between the actual surface and the nominal. CMMs now available can perform open-loop scanning at up to 150 mm/sec [24].

Figure 2.11 Renishaw's SP600Q Compact Analog Scanning Probe for Small CMMs [25]

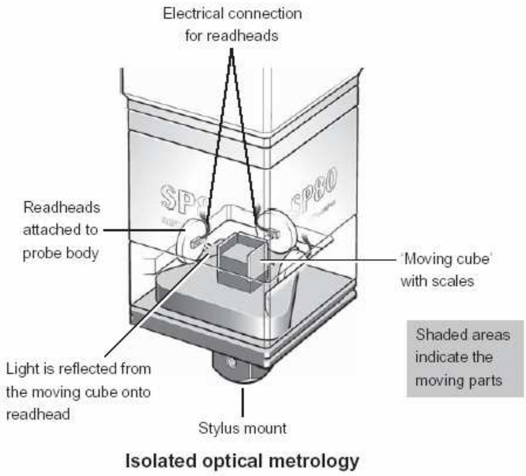

Figure 2.12 Renishaw's SP80 isolated optical metrology system [26]

Figure 2.12 represents the Renishaw probe SP80 utilizing the isolated optical metrology system. The SP80 can carry styli up to 500 mm(19.69 in) long and 500 g (17.64 oz) mass, including star configurations. The isolated optical metrology system can detect sources of variable error such as thermal and dynamic effects. In contrast, probes with displacement sensors mounted to stacked axes suffer from latency under changing inertial loads, and can not detect thermal growth in their mechanisms. The readheads for each axis are fixed to the body of the probe, and measure the deflection in each direction. Any inter-axis errors caused by the arc motion of each pair of parallel-acting springs are directly measured by the sensor system. Isolated optical metrology systems have no moving wire connections [26]. Renishaw's SP25M scanning probe, is actually two sensors in one, enabling scanning and touch-trigger probing in a single probe system. SP25M gives highly accurate scanning performance with stylus lengths from 20 mm to 400 mm (0.79 in to 15.75 in) using M3 stylus range. By optical measurement via two mirrors on the scan module all movements of the stylus can be measured without any inter-axis error and with a resolution of about 0.01 μm. The kinematics is much simpler (fewer moving parts) and can be made very small. As hinges there are two membrane springs. One is flexible for rotations around its centre and translations in the Z-direction creating a pivot point, while the other is flexible for translations in any direciton [27].

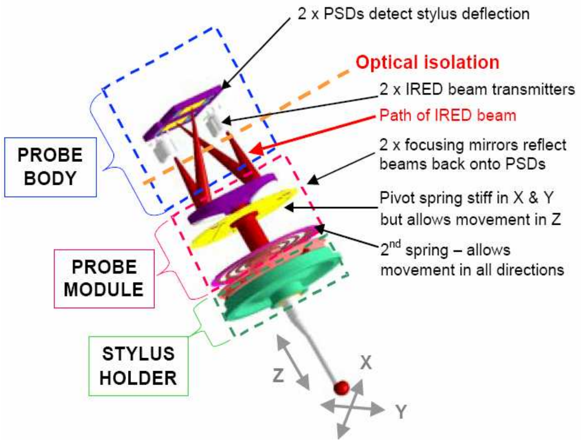

Figure 2.13 Renishaw SP25M probe [27]

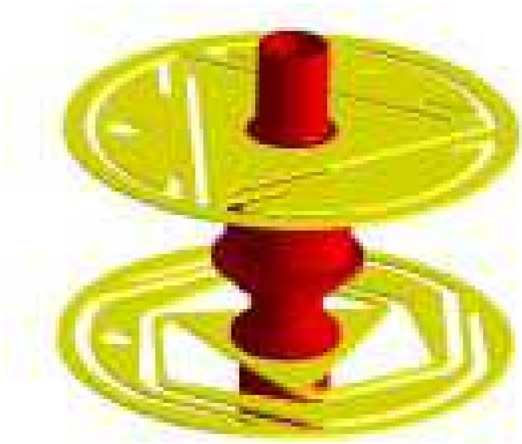

Figure 2.14 Renishaw’s SP25M patented pivoting motion systems with two diaphram springs [27]

2.11 Laser Probes

Noncontact trigger probes are used in the same manner as touch trigger probes. However, with non-contact probes, a beam of light operating as an optical switch contacts the workpiece. The non-contact probe is permanently set to a specific stand-off distance at which the light beam is triggered and measurements are taken. Because the probe never comes into contact with the workpiece surface, damage is eliminated, and measurement speed is greatly improved. Laser probes project a laser beam onto the surface of the part, the position of which is then read by triangulation through a lens in the probe receptor. The technique is much like that used by surveyors to find a position or location with bearings from two fixed points that are a known distance apart. Laser probe triangulation provides the actual position of the feature on the workpiece being measured [24].

Figure 2.15 CMM Laser scanning probe by Laser Design Inc. [28]

2.12 Future Challenges in Coordinate Metrology

Co-ordinate metrology has reached a very high state of development concerning versatility and accuracy for common engineering parts. However, this high accuracy often cannot be achieved when measuring very small (<< 1mm) and very large features (>>1m). For small features, the limiting component particularly is the probing system, since conventional probing systems cannot be downscaled. Today metrologists are confronted with the broad size spectrum of 3D measuring tasks in engineering. They are ranging from micro-mechanical components with sub-millimeter features up to part sizes of several meters. For the common midsize engineering parts, commercial CMMs with highly accurate geometry and probing heads can even fulfill most challenging demands. Nevertheless, the extension of CMM metrology to smaller structures is mainly limited by the probing system, while the limitation to measure very large structures with high accuracy is particularly the machine geometry and its stability [29]. Here one can see metrology influencing developments such as:

- higher precision,
- miniaturization, (electronic devices, sensors, actuators etc.)

- improvements in economy,
- increasing reliability,
- potential higher accuracies,
- higher measurement speeds,
- using very light and small designs in probing systems,
- designs that are independent from the environment of the measurement task,
- performing a complete error mapping of CMMs [8].

2.13 Giant Magnetoresistive (GMR) Effect

In 1988, scientists discovered the “Giant Magneto Resistive” effect, a large change in electrical resistance that occurs when thin stacked layers of ferromagnetic and nonmagnetic materials are exposed to a magnetic field [30]. The GMR effect was discovered in 1988 [31], [32], [33]. It is the phenomenon that the resistance of a material depends on the angle between magnetization directions at different locations in the material [33].

The "Giant Magnetoresistive" (GMR) effect was first discovered; Fe/Cr/Fe trilayers; in the late 1980s by two European scientists: Peter Gruenberg of the KFA research institute in Julich, Germany, and Albert Fert of the University of Paris-Sud. The scientists observed very large resistance variations (6 percent and 50 percent, respectively) in materials composed of alternating very thin layers of various metallic components. On the other hand, physicist did not believe that effect was physically possible so the results obtained from the experiments took the scientific community by surprise. The experiments executed by two European scientists were performed at low temperatures and in the presence of very high magnetic fields. The materials used in the experiments are developed in particular place/way, that cannot be mass-produced, but the obtained results during the experiments of sent scientists around a new horizon to see how they might be able to support the power of the Giant Magnetoresistive effect [34]. In accordance with the relative orientations of the magnetic moments in alternate ferro-magnetic layers, a significant change in electrical resistance seen in ferro-magnet / para-magnet multilayer structure and this resistance changes as a function of an applied field. In other words, the GMR effect is dependent to the electrical resistivity of the electrons in a magnetic metal on the direction of the electron spin, either parallel or anti-parallel to the magnetic moment of the films. Electrons which have a parallel spin experience less scattering and therefore have a lower resistance. When the moments of the magnetic layers are anti-parallel at low field, the electrons will not experience low scattering rate in both magnetic layers, so those electrons have higher resistance respectively [35]. When an external magnetic field is applied, the moments of the magnetic layers are aligned as seen in Figure 2.17, electrons with their spins parallel to these moments pass freely through the solid, resulting a lower electrical resistance. The following diagrams show how GMR effect works [30].

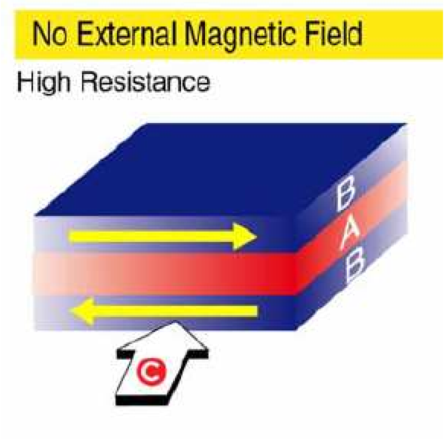

Figure 2.16 GMR effect without external field [30]

As illustrated in Figure 2.16, **A** is a conductive, non-magnetic inter-layer between top and bottom layer **B**. Magnetic moments in alloy **B** layers face opposite directions due to the anti-ferromagnetic coupling. As a result, resistance to current **C** is high [30]. As illustrated in Figure 2.17, due to an applied external magnetic field **D** defeats the anti-ferro-magnetic coupling, which result the alignment of the magnetic moments in alloy **B (top and bottom)** layers, so the electrical resistance decreases dramatically [30].

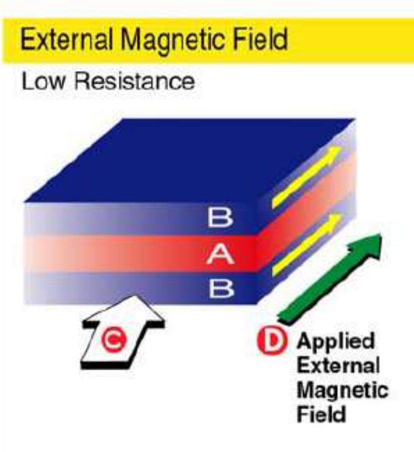

Figure 2.17 GMR effect with an applied external magnetic field [30]

2.14 Use of Giant Magnetoresistors (GMR) in Hard Drive Read Head

In hard disk drive (HDD) storage industry, Giant magnetoresistive (GMR) head technology is the latest progress. Anisotropic Magnetoresistive (AMR) technology is currently the fundamental, high-performance read head technology used in today's hard drives. As the years went by AMR heads have been replaced by thin film inductive heads and the AMR heads took the previous standard in the marketplace. As GMR heads provide increased areal density, improved performance, and reliability; those heads have become the most dominant technology since 2000 [36]. From the first hard drive in 1954, the International Business Machines (IBM) is the major leading company in the development of HDD technologies. By connecting the head and disk permanently, IBM's Winchester technology, first introduced in 1973, increased storage density [34], [36]. Thin film inductive (TFI) technology, introduced in 1979, was another vital development. The technology used in read/write head before thin film inductive; wired, packed magnetic cores; had been the standard in the industry. Later on IBM introduced Anisotropic Magnetoresistive (AMR) technology into hard disk drives (HDD) products in 1991. The major advantage of the AMR technology is to enable the storage of more data per disk, and it reduced the number of heads and disks required per drive for a desired capacity. AMR heads have been improved their evolution from the beginning of their introduction, and those heads can support areal densities as high as 3.3 gigabits/inch^2 for now [36].

Nowadays, AMR head technology has been passed with the entrance of Giant magnetoresistive (GMR) or spin valve heads in to the HDD industry. Furthermore, GMR heads extended the areal density to greater than 10 gigabits/inch^2 (more than three times the areal density provided by AMR heads). As a result, GMR heads bring more powerful workstation capacity to the average desktop PC user because of having more than twice the sensitivity of AMR heads. Thence, this optimizes HDD performance for storage intensive multimedia business and entertainment programs, allowing television-like video, picture, and sound quality. Beyond GMR, the next step in hard drive technology will be “Synthetic Spin Valve” GMR, which will be followed by Colossal MR (CMR) [36].

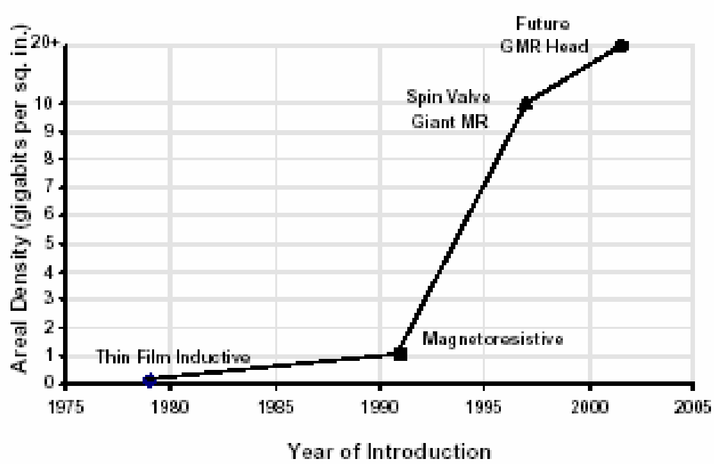

Figure 2.18 Evolvement chart of the HDD Technology [36]

As the years went by, the demand for higher areal densities and data rates increases. Therefore, heads of increased sensitivity are required to support high quality read-back signals. Due to the GMR’s outstanding performance, GMR heads enable hard drive products to offer maximum storage capacity with a minimum number of heads and disks. Moreover, less amount of components (i.e., heads and disks) provide greater reliability, lower power requirements, and lower storage costs. More importantly increased signals from GMR heads also help to overcome system noise problems. GMR heads are used in the today's latest technology drives, which have capacities of up to 75 GB and areal densities of approximately 10 to 15 Gbits/inch^2 [36].

The advantages of GMR over AMR can be listed as below:

- More sensitive for changing the disk magnetization,
- Less mechanical spacing required for the same performance,
- Able to support areal densities of more than 10 gigabits/inch^2,
- Fewer heads and disks required for the same storage capacity.

The GMR head configuration, basically consists of four magnetic thin films:

1. A **sensing (free)** magnetic layer, as its name implies, this is the sensing layer. This layer is made of a nickel-iron alloy, and is passed over the surface of the data bits to be read. This magnetic layer is free to rotate in reaction to the magnetic patterns on the disk.

2. A non-magnetic conducting **spacer** layer made from copper, and is placed between the free and pinned layers in order to separate them magnetically.

3. A magnetic **pinned** layer made of cobalt material is held in a firm magnetic orientation by virtue of its adjacency to the exchange layer.

4. An **exchange** layer made of an "antiferro-magnetic" material, typically put together from iron and manganese, and fixes the pinned layer's magnetic orientation [30], [37].

Sensing, spacer, and pinned layers control the resistance of the sensor in response to magnetic fields from the sensor. In accordance with the spin orientation of the conducting electrons and the difference in the magnetization directions of the free and pinned layers, a change in the resistance of the GMR sensor is obtained [36], [37].

By the help of the exchange layer, located adjacently to the pinned layer, the magnetic orientation of the pinned layer is fixed and held in place. As the data bit on the disk passes under the GMR element, the magnetic orientation of the free layer changes in response to bits (tiny magnetized regions) on the disk by rotating relative to the magnetic orientation of the pinned layer. Consequently, this magnetic rotation generates a considerable amount of change in sensor resistance or signal. Since the layers are too close to each other, electron scattering will cause some electrons to move from one layer to the other layer. When an electron’s spin matches the magnetic orientation of the layer in which it flows, those electrons experience lower resistance. As a result, the net resistance changes and provides a signal that can be sensed by the appropriate electric circuits [34], [37].

The configuration of the HDD is illustrated in Figure 2.19.

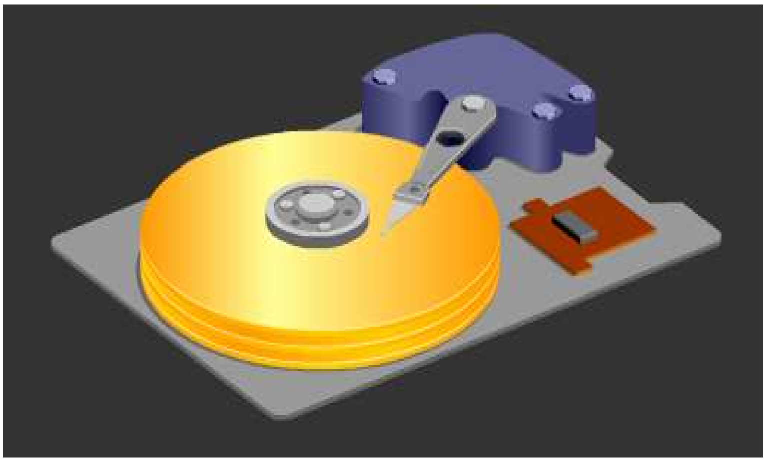

Figure 2.19 Inside of a hard disk drive [34]

As illustrated in Figure 2.19, the head is located at the end of the actuator arm, and moves over the disc to read and write data.

Figure 2.20 End of the actuator arm (close up view of the Figure 2.19) [34]

As can be seen from the Figure 2.20, only an inductive write element and its copper coil can be seen. The GMR read sensor is located below the coils.

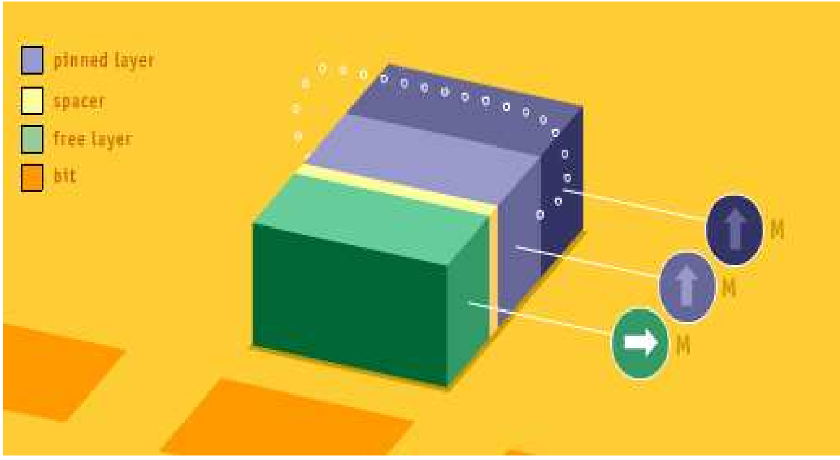

Figure 2.21 GMR read sensor / spin valve (close up view of the Figure 2.20) [34]

According to the Figure 2.21, as the magnetic bits on the hard disk pass under the head, the magnetic orientation in the sensing (free) layer changes as indicated by the white arrow.

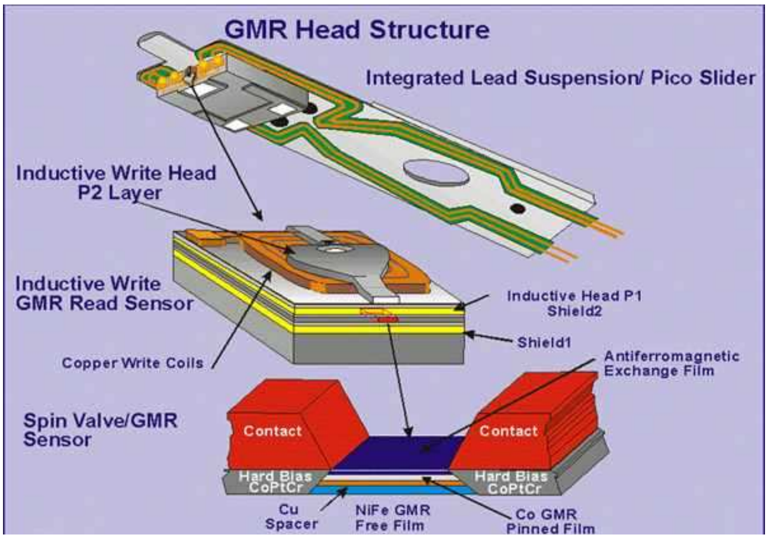

Figure 2.22 Detailed structure diagram of the GMR Head assembly [34], [37]

In order to visualize the GMR heads; for the dimensional purpose; used in the hard disks more close to real, Figure 2.23 will be the more realistic one. However, in Figure 2.23 only the inductive write element and its copper coil can be seen [34]. The GMR read sensor is located below the coils.

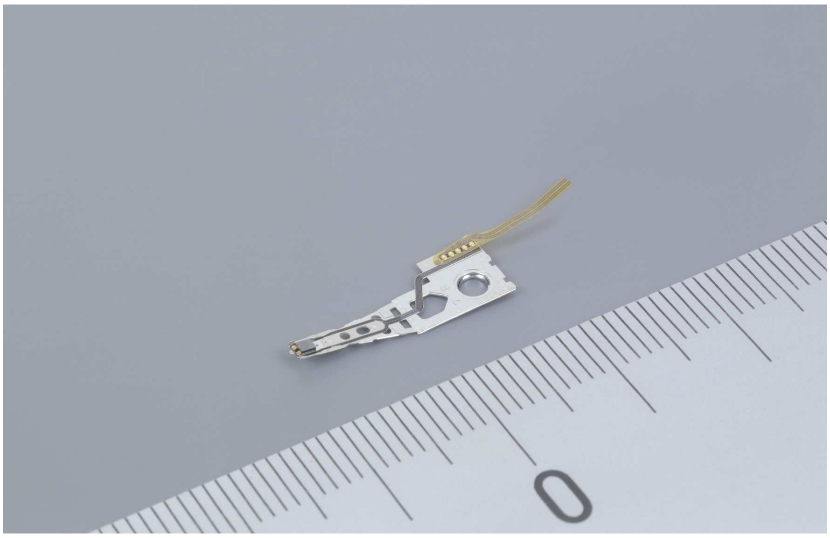

Figure 2.23 HDD Actuator arm and GMR assembly

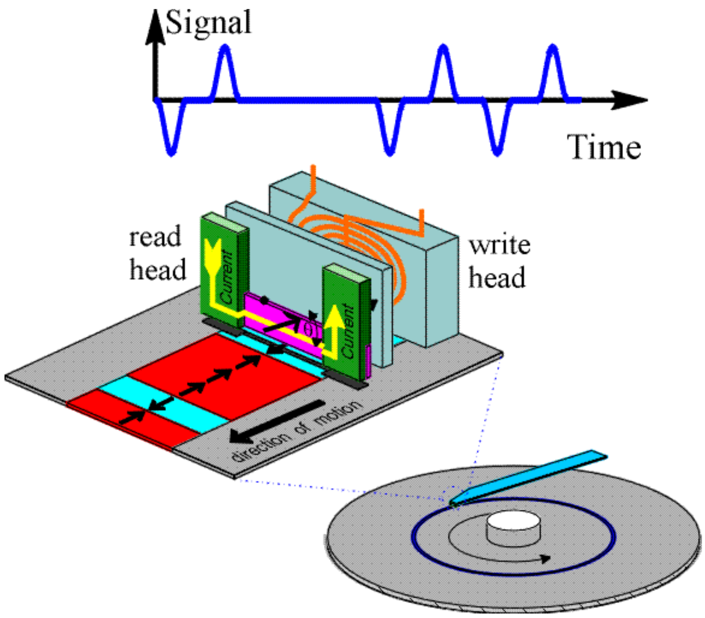

Figure 2.24 The GMR head in HDD [38]

2.15 Giant Magnetoresistive (GMR) Materials

The materials are basically composed of iron, nickel, cobalt and copper. Several alloys of these materials are settled in layers as thin as (i.e.: 5 atomic layers) and as thick as 18 microns in order to manufacture the GMR sensor element. As the thickness of the conductors decreases to a few atomic layers, the GMR effect shows itself more obvious since the effect is based partially on the increasing resistivity of conductors. In the case of bulk material form, conducted electrons in these materials can travel a long distance before scattering, due to a collision with another atomic particle. The average length that the electron travels before being scattered is called the mean free path length. However, considering the case where materials are very thin, an electron cannot travel the maximum mean free path length. As a matter of fact, the electron will reach the boundary of the material and scatter there, instead of scattering off another atomic particle. So, this results in a lower mean free path length for very thin materials. Therefore, for this case the obtained result is the higher electrical resistivity because of the difficulty of the travel of the conducted electrons in this type of material. The chart below implies the relationship between the resistivity of a magnetic material (i.e.: iron or nickel) and the thickness of the material at very small dimensions [30], [39].

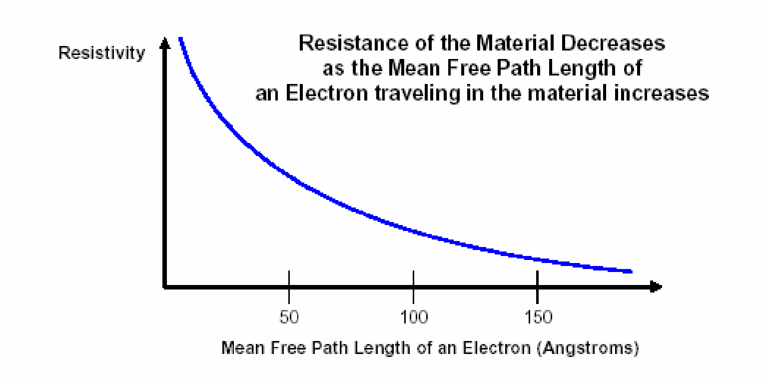

Figure 2.25 Relationship between the resistivity of a magnetic material and the thickness of the material [39]

In order to take the advantage of this effect, GMR films are manufactured with very thin layers of alternating magnetic and non-magnetic materials. This is done to allow magnetic variation of the electron spin in the materials. In order to make the GMR effect physically possible, the spin dependence of conducted electrons in magnetic materials, along with the increasing resistivity at very small material thicknesses, combine [39].

The Figure 2.26 shows a simplified structure of a typical GMR sensor film.

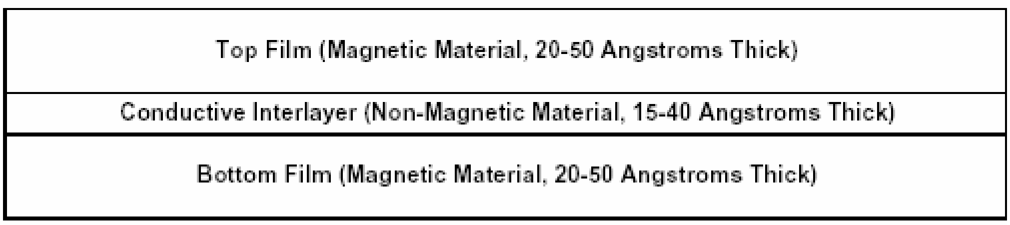

Figure 2.26 Cross Sectional structure of the basic GMR material [39]

As can be seen from Figure 2.26**,** there are two magnetic material layers, placed on top and bottom of the non-magnetic interlayer. The magnetic layers are formed to have anti-ferromagnetic coupling. In other words, the magnetization of these layers is opposite to each other when there is no external magnetic field applied to the material. Anti-ferromagnetic coupling can be visualized by imagining two bar magnets on either side of a thin sheet of plastic. The magnets couple head to tail (north pole to south pole) across the boundary formed by the plastic. In a similar fashion, the magnetization direction of the magnetic layers in the GMR film couple head to tail across the non-magnetic interlayer of the film. Therefore, the conduction of electrons in magnetic materials has a spin characteristic. When the material is magnetized in one direction, the electrons are referred to as spin up electrons. When the material is magnetized in opposite direction, the electrons are referred to as spin down electrons. Figure 2.27 shows some electron paths inside the GMR material structure. The two arrows on the top and at the bottom of the figure indicate the anti-ferromagnetic coupling. Considering that the electrons tend to scatter off the two GMR material boundaries as stated before in this chapter. This is due to the electrons from the spin up layer are trying to enter the spin down layer, and vice versa. As a result, due to the differences in the electron spins, the electrons will scatter at these interfaces [39].

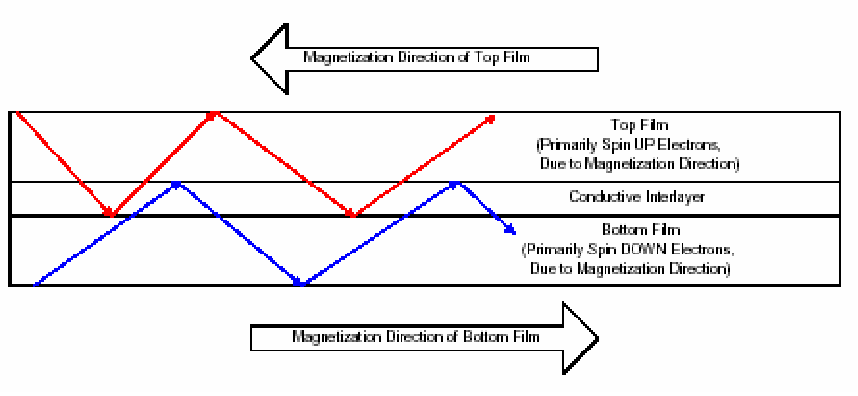

Figure 2.27 Spin up and spin down movement of the electrons [39]

As illustrated in Figure 2.27, spin up electrons scatter at interface with spin down layer and vice versa. So, the average mean free path of the electrons is short resulting in a relatively high electrical resistance. In the case of an external magnetic field of sufficient magnitude is applied to the GMR material, it will defeat the anti-ferromagnet coupling of the magnetizations between the two magnetic layers. At that point, all the electrons in both films will have the same spin. It will then become easier for the electrons two move between the layers.

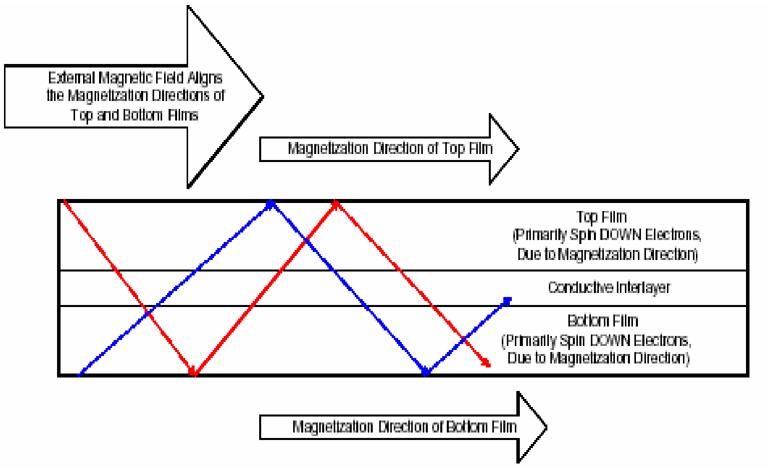

Figure 2.28 Spin States of the magnetic layers in the case of an applied external magnetic field [39]

As can be seen from Figure 2.28, spin states of the magnetic layers are same (aligning in the same direction). The mean free path length of electron has now increased which results in an overall lower electrical resistance for the GMR material.

Actually, not all GMR materials operate in the fashion as described above. All GMR materials based on varying the difference between the magnetization directions of adjacent layers in the GMR film structure, but some achieve this variation in different fashions [39].

The other most common type of GMR material is named as a spin valve GMR material. This type of material does not necessarily depend on anti-ferromagnetic coupling of the adjacent magnetic layers. As stated in the previous section in this case one of the magnetic layers is pinned, or fixed with respect to its magnetization direction. When the fixed layer is exposed to a magnetic field that is operating normally, the magnetization direction of the pinned layer will not move. Therefore, the externally applied magnetic field will control the direction of the other magnetic layer, named as the free layer. As the angle between the free layer and the pinned layer changes, the mean free path length that the electrons travel in the GMR film also changes, and as a result, the electrical resistance will change. Stabilization of the magnetization direction of the pinned layer in spin valve GMR materials can be done in several ways. However, here it is important to figure out that the layer is pinned in a robust manner; otherwise, the pinning can be opened by application of a large magnetic field and this will destroy the operation of the sensor dramatically. Therefore, in order to set the pinned layer of the film more properly, some of the GMR sensor manufacturers uses the application of large magnetic fields and high anneal temperatures. So this layer cannot be unpinned with the application of any magnetic field in the normal temperature range of operation. Therefore, the sensor cannot be damaged by the large magnetic fields [39].

2.16 GMR sensors

Over the previous years inductive and Anisotropic Magnetoresistive (AMR) based sensors for read heads in hard disks, data storage systems have been fully substituted by GMR based sensors. On the other hand, magnetic sensors based on the GMR effect are now finding their way in to industrial and automotive applications [40].

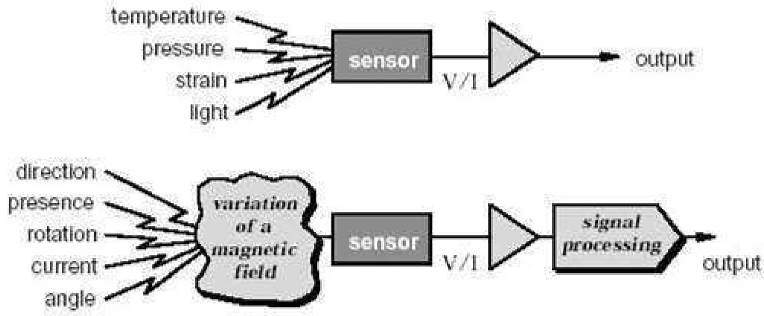

Figure 2.29 Comparison of the Conventional and magnetic sensing [38]

As can be seen from **Figure 2.29**, the output of conventional sensors will directly report desired parameters. On the other hand, magnetic sensor only indirectly detects these parameters [38].

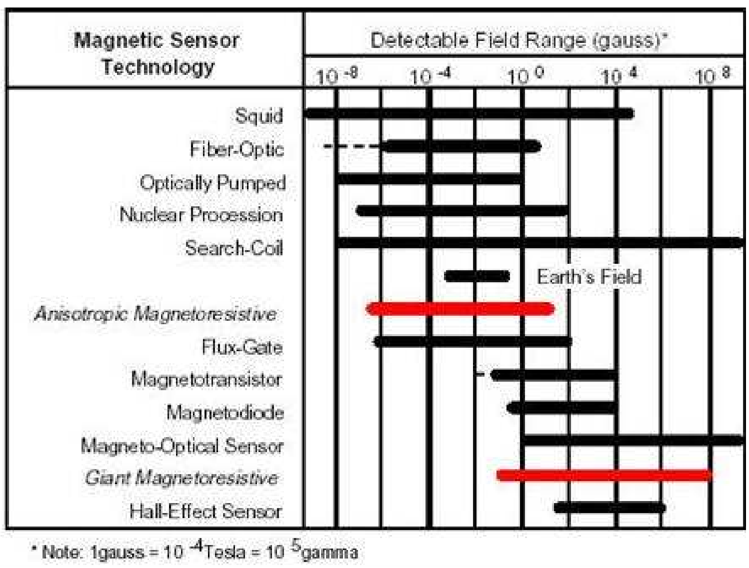

Figure 2.30 Magnetic sensor technology field ranges [38]

The giant magnetoresistance GMR effect offers interesting new possibilities for sensor applications. Most research efforts in the field of GMR have been related to application in magnetic recording or magnetic memories. Nevertheless, several non-recording GMR sensors have also been reported and the first commercial GMR sensors are available now. Throughout the literature on magnetic field sensors, the realization of a Wheatstone-bridge configuration is one of the major issues. The reason is that it is not trivial to obtain GMR elements with an opposite output signal on a single substrate. For comparison, in AMR sensors this can be achieved in an elegant way by choosing barber-pole structures with opposite signs of the slanting angle. For GMR sensors, this cannot be used since the GMR effect does not depend on the current direction. For most sensor applications, a bridge configuration is desired in order to eliminate the effect of the temperature dependence of the resistance of GMR materials. The first commercial GMR sensor was presented by Nonvolatile Electronics (NVE) around 1994 [30], [33], [39]. Their sensors are based on antiferromagnetically (AF) coupled multilayers [33], [41], [42]. A bridge configuration was realized by shielding two of four elements by a soft magnetic shield, which at the same time acts as flux concentrator for the other two magnetically active elements [33], [43]. However, because this bridge due to the type of multilayer is based on elements with and without output, instead of elements with opposite output, it is effectively a half-bridge and can only provide half of the output of a single GMR element. The second commercial GMR sensor is fabricated by Infineon Technologies [44] and is based on a hard–soft multilayer with AAF [33], [45], [46], [47]. Bridge configurations are realized by applying a spatially varying magnetic field to the sensor chip after deposition and patterning. Because of its angle dependence, it is suitable as a contactless potentiometer [33], [48], but the magnetic stability is insufficient for automotive or industrial applications: according to the specifications, the properties can be changed irreversibly by fields above 15 kArm. It is obvious that the field strength that is used to set the bridge elements after fabrication is also able to damage a sensor later. A GMR sensor based on an exchange-biased spin valve was described by IBM, but not commercialized [49]. A full Wheatstone-bridge configuration could be fabricated by setting the exchange-biasing direction of different elements in opposite directions by field cooling: a conductor is electrically isolated positioned on top of the GMR elements in such way that the current flowing through it induces a magnetic field with opposite directions in different elements. At the same time, the dissipation of the current is used to heat the GMR elements above the blocking temperature of the used exchange-biasing material Fe–Mn. On cooling down the exchange-biasing effect attains the direction of the locally induced magnetic field. This idea has not been commercialized, maybe because of the insufficient thermal stability and field range. The current through the patterned conductor is inherently limited and thus the magnetic field and temperature that can be obtained. Therefore, this concept cannot be applied to robust GMR materials. Recently, another bridge sensor based on exchange-biased spin valves has been reported in the literature by INESC [50], in which two of four elements are magnetically inactivated by positioning them on a roughened substrate region. Like the sensor from NVE, the bridge output is halved compared to that of a single element. The operation range of the sensor is limited to 150 Oe [33].

In this study, NVE's GMR sensors are considered. The NVE standard line of magnetic field sensors use a unique configuration employing a Wheatstone bridge of resistors and various forms of flux shields and concentrators. Using magnetic materials for shielding eliminates the need for a bias field with GMR sensors. NVE has developed a process to plates a thick layer of magnetic material on the sensor substrate. This layer forms a shield over the GMR resistors underneath, essentially conducting any applied magnetic field away from the shielded resistors. The configuration allows two resistors (opposite legs of the bridge) to be exposed to the magnetic field. The other two resistors are located under the plated magnetic material, effectively shielding them from the external applied magnetic field. When the external field is applied, the exposed resistors decrease in electrical resistance while the other resistor pair remains unchanged, causing a signal output at the bridge terminals. The plating process developed by NVE for use in GMR sensor applications has another benefit: it allows flux concentrators to be deposited on the substrate. These flux concentrators increase the sensitivity of the raw GMR material by a factor of 2 to 100. The flux concentration factor is roughly equivalent to the length of one shield divided by the length of the gap. This allows use of GMR materials that saturate at higher fields. For example, to sense a field from 0 to 100

Oersteds, NVE deposits a GMR sensor that saturates at a nominal 300 Oersteds and flux concentrators with a magnification factor of three [30], [39].

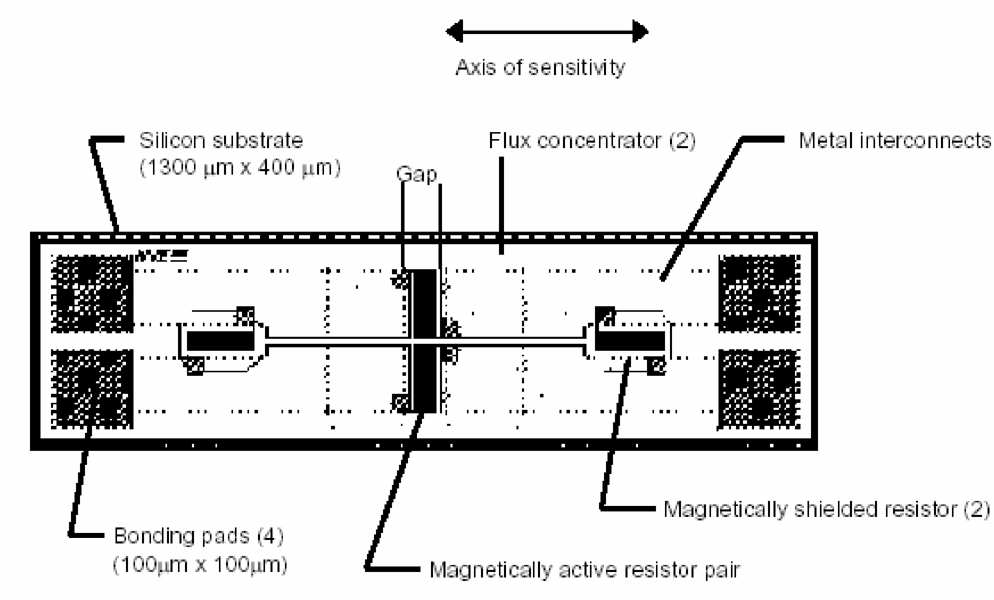

Figure 2.31 Typical GMR magnetic field sensor layout [39]

All of NVE's GMR Magnetic Field sensors have a primary axis of sensitivity. Figure 2.32 shows an AAxxx-02 Series GMR Magnetic Field Sensor with a cut away view of the die orientation within a package [39].

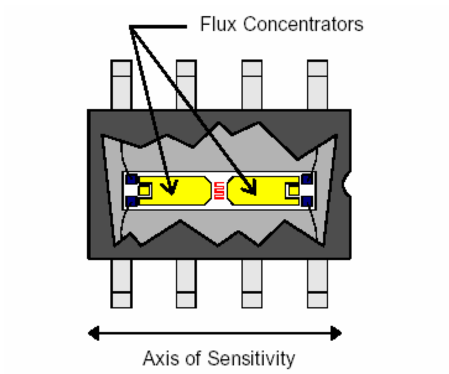

Figure 2.32 NVE's AA00x-02 magnetic field sensor [39]

The flux concentrators on the sensor die gather the magnetic flux along the axis shown and focus it at the GMR bridge resistors in the center of the die. The sensor will have the largest output signal when the magnetic field of interest is parallel to the flux concentrator axis. For this reason, care should be taken when positioning the sensor to optimize performance. Although sensor position tolerance may not be critical in gross field measurement, small positional variation can introduce undesirable output signal errors in certain applications [39].

2.17 Application Areas of the GMR Sensors

For automotive and industrial environments, magnetic sensors are often preferred because of their robustness, insensitivity to dirt and their contact free way of sensing. The main applications for GMR sensors are angle, rotation speed, and position sensing. Since GMR sensors exhibit excellent linearity and repeatability, and their high sensitivity allows them to be used to provide displacement information of actuating components in machinery and linear displacement transducers. These sensors have been used to resolve displacements down to one micron. A typical application for GMR sensors is proximity detection. While this can be done using other technologies, the sensitivity of the GMR device allows a greater design freedom when specifying mechanical tolerances and magnet strengths [33], [40], [51], [52].

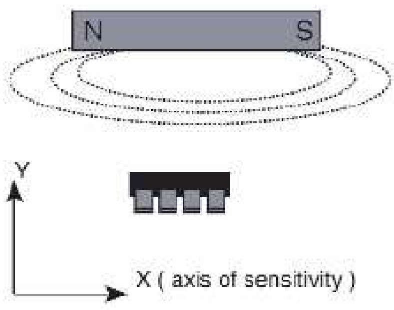

Figure 2.33 GMR and a permanent magnet configuration providing the position information [52]

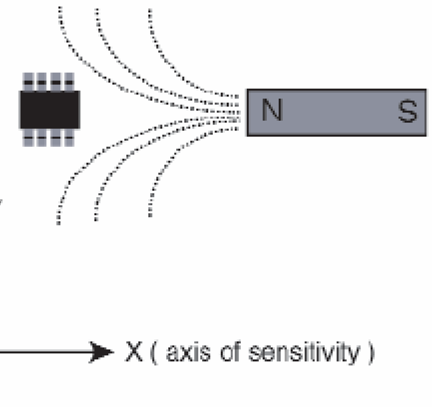

Figure 2.34 Another GMR and a permanent magnet configuration providing the position information [52]

Typical applications include displacement sensors, accelerometers, pneumatic cylinders, artificial limbs, micro movement sensors, pressure sensors, vehicle detection, gear tooth sensing, crank and camshaft timing, transmission & Wheel speed sensing, ABS sensor, rotary encoders, flow meters, live wire detection, isolated current detection, currency detection (magnetic inc detection on bank notes), unexploded ordnance (checking for anomalies in background magnetism of soil), geophysical survey, medical, Earth's magnetic field sensing [52].

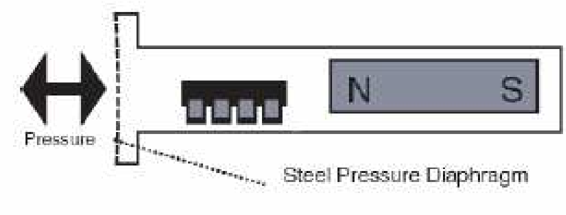

Figure 2.35 Simple pressure sensor implementation [52]

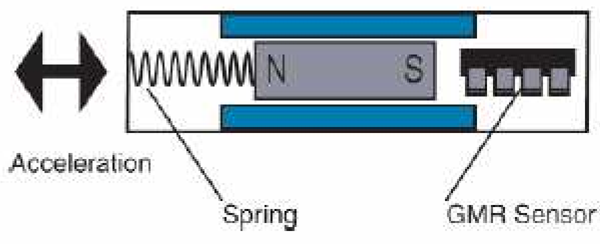

Figure 2.36 Accelerometer implementation [52]

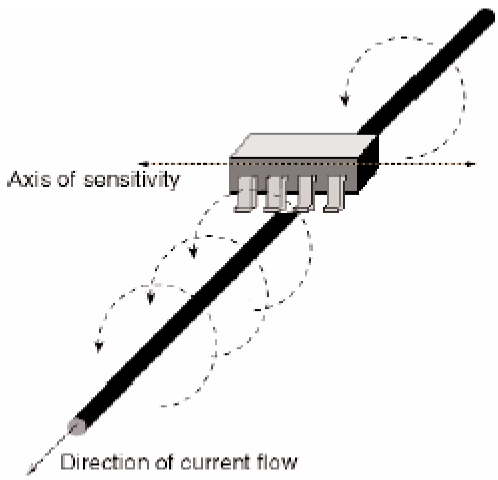

Figure 2.37 Current detection [52]

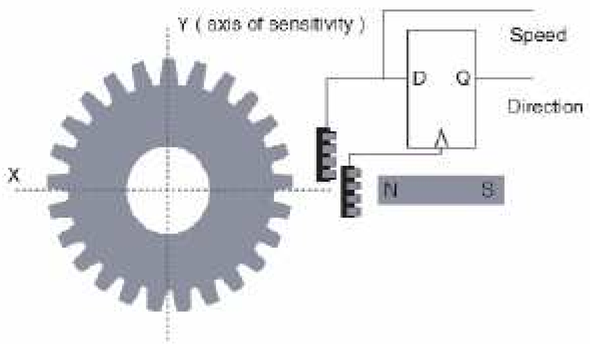

Figure 2.38 Speed and direction sensing [52]

As can be seen from Figure 2.38, the addition of another sensor permits the direction of rotation to be sensed as well as the speed. The second sensor must be located to be 90º out of phase to the first. This can be detected using a standard D-type flip flop circuit [52].

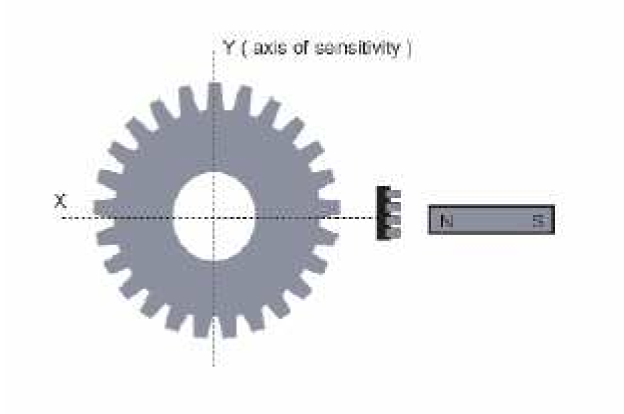

Figure 2.39 Speed sensor [52]

2.18 Conclusion

In this chapter, review of the state of the art in measurement technology, Giant Magnetoresistive (GMR) effect, and the basis of the GMR are described. Furthermore, the fundamental function and working principle of the touch trigger probes are presented. Different touch trigger probes with different sensing stage concepts are also described in this chapter. Moreover, together with the contact probes, non-contact probes are also mentioned. Besides, different application fields of the GMR sensors, the usage of the GMR effect in hard disc drive systems is also mentioned. Due to GMR sensor's outstanding sensitivity, GMR sensors are used for the formation of the sensing stage of the designed touch trigger / scanning probe.

CHAPTER 3

GMR SENSOR CHARACTERISTICS

3.1 Introduction

In order to avoid the ambiguities coming from the design failure, GMR sensor tests are performed. Furthermore, those tests play an important role during the design process. After those tests, operation region of those sensors (linear zone), place where they are going to be located and some design parameters (i.e.: axial distance and tangential distance) can easily be defined to obtain the best performance. Therefore, GMR sensor tests are performed with an extra effort.

During the tests, NVE GMR sensor AA006-02 (characteristics of this chip is given in Appendix B.1) is used due to its high sensitivity. Anvil gauge setup is dominantly used in those tests to define the axial distance more precisely. Moreover, the test configuration is formed similar to the probe's configuration just for the sake of the test's quality. GMR sensor, magnet plate and the magnets are located similar to the places where they are found in the probe body. Thus, in other words, same media is prepared for the GMR sensor, therefore the generated outputs will be the same while the sensor is functioning in the probe body.

During the tests, 2 GMR sensors are placed next to each other, so this configuration gave us an opportunity to compare the outputs coming from those sensors and to monitor the behaviour of the sensors. In brief, those tests showed us the major and specific characteristics of the GMR sensors. Setup configuration is formed as in Figure 3.1;

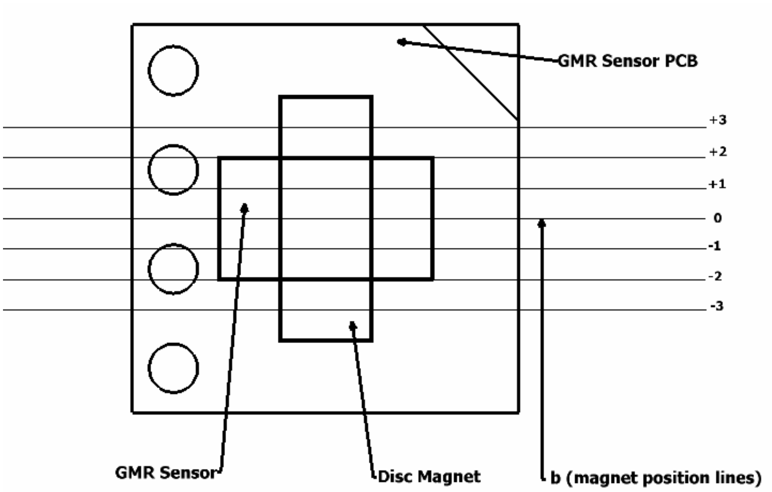

Figure 3.1 Front view configuration of the GMR sensor chip and the disc magnet

As can be seen from the above Figure 3.1, center axes of the GMR sensor chip and magnet are coincide with each other. GMR sensor PCB is attached on a table and the magnets are located on the magnet plate and afterwards the magnet plate is put on to the anvil gauge setup. In accordance with this formed setup magnet is moved up and down by 1mm (along the b-direction) respectively.

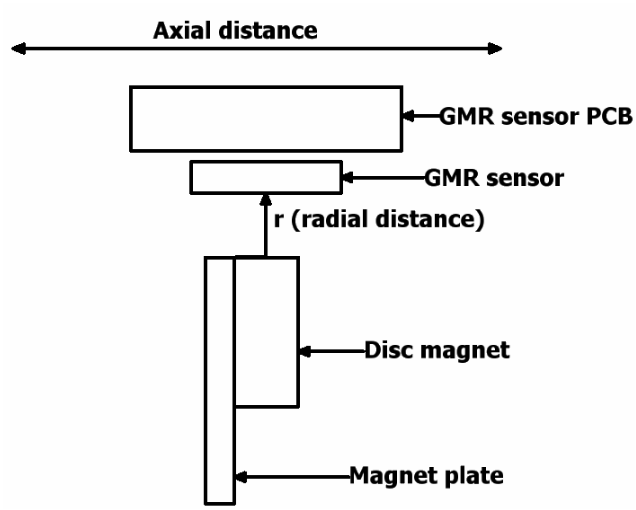

Figure 3.2 Top view configuration of the GMR sensor chip and the disc magnet

During the tests, magnet is driven through the axial distance travel span as defined in the above Figure 3.2. In accordance with that move, magnet is moved towards the GMR sensor chip by 0.50 mm. Starting from 0.50 mm radial distance and ending with 5.50 mm radial distance (radial distance is adjusted via comparator). This procedure is carried out for every magnet position line (b) as indicated in Figure 3.1. Thus, by virtue of those tests, the axial distance and the radial distance can be acquired. So the magnets and the length of the shaft that is holding the magnet plate can be defined respectively. In Figure 3.3, the configuration of the two GMR sensors can be seen. Since the centers of the GMR sensors are known, the length of the magnet plate holder shaft can easily be found in order to locate the sensors where their outputs lay on the linear zone.

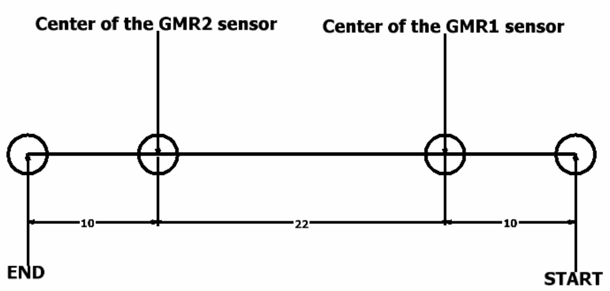

Figure 3.3 Configuration of two GMR sensor chip

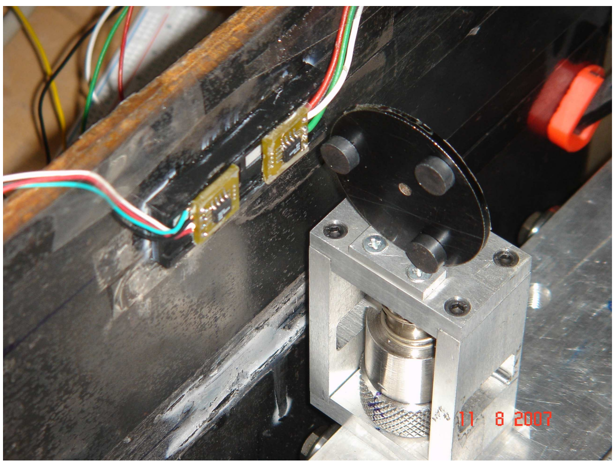

Figure 3.4 Test with disc magnets

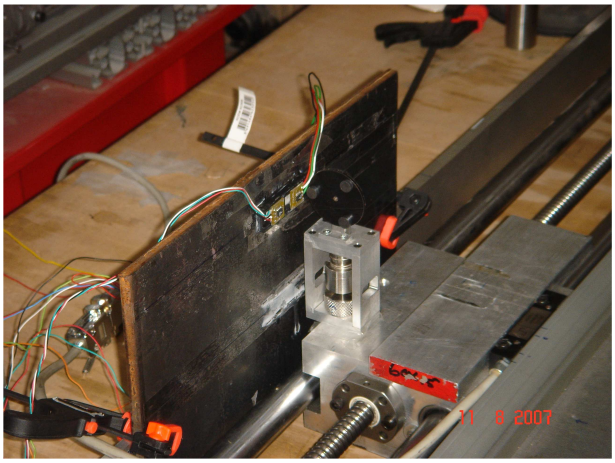

Figure 3.5 Another view of test with disc magnets

3.2 Results of GMR Sensor Tests with Disc Magnets

The most important thing is that, tests are performed via a spring steel magnet plate, so in the probe spring steel material will be used as a magnet plate holder not to encounter different and inconvenient results. Tests are performed via two GMR sensors.

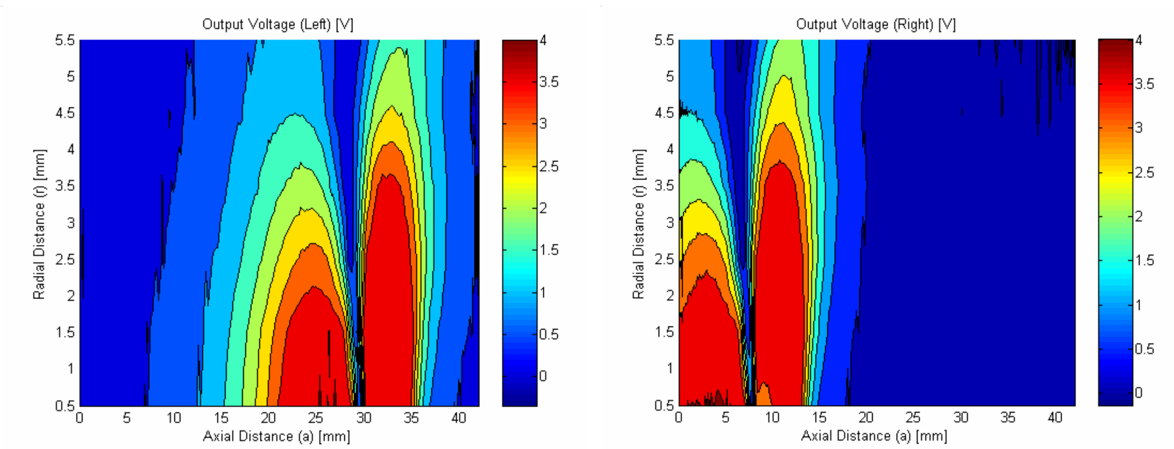

(a) Left sensor output when b = -3 [mm] **(b)** Right sensor output when b = -3 [mm]

Figure 3.6 Results of GMR sensor tests with disc magnet (to continue)

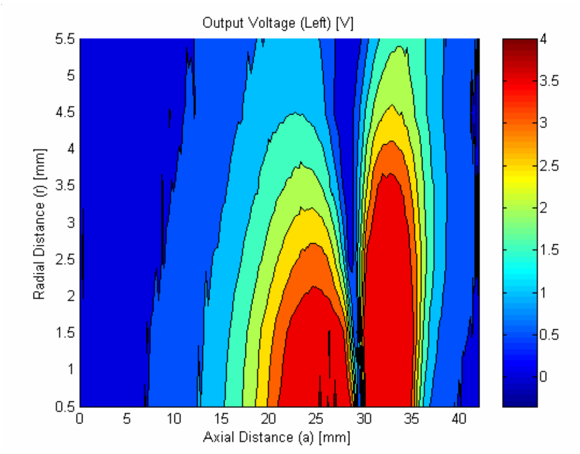

(c) Left sensor output when b = -2 [mm]

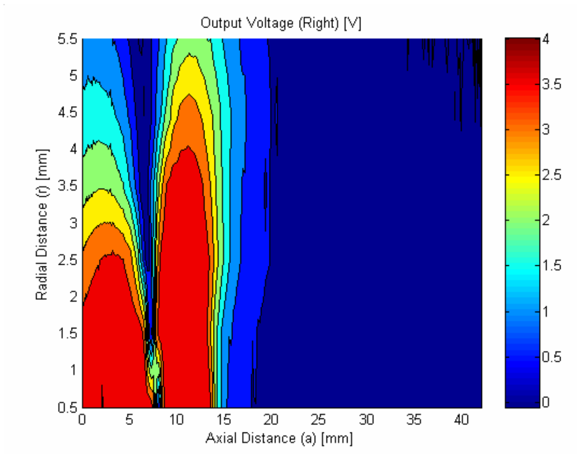

(d) Right sensor output when b = -2 [mm]

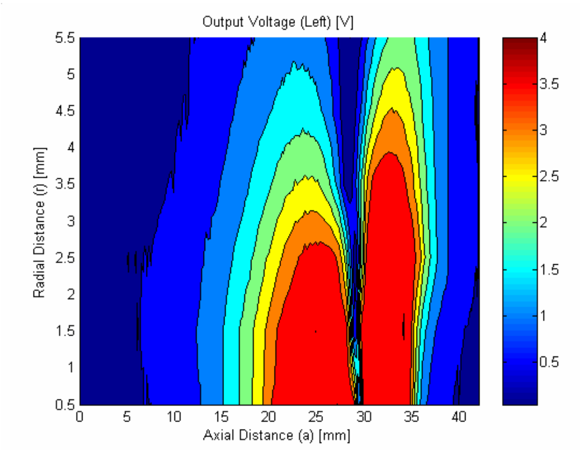

(e) Left sensor output when b = -1 [mm]

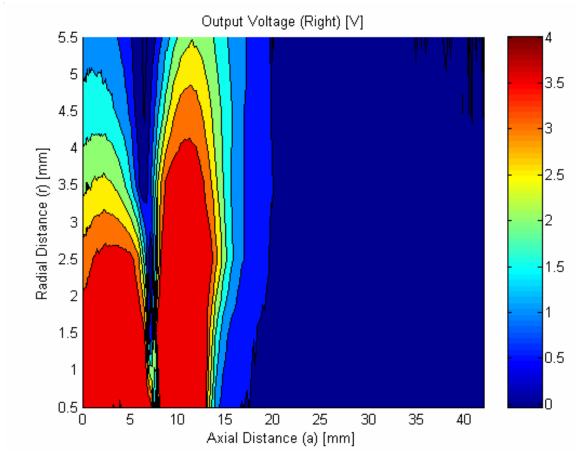

(f) Right sensor output when b = -1 [mm]

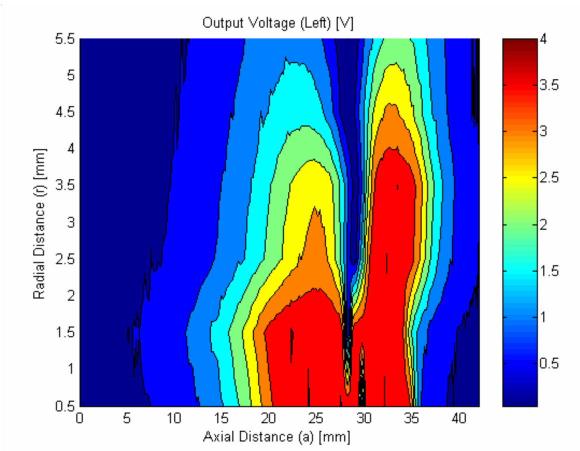

(g) Left sensor output when b = 0 [mm]

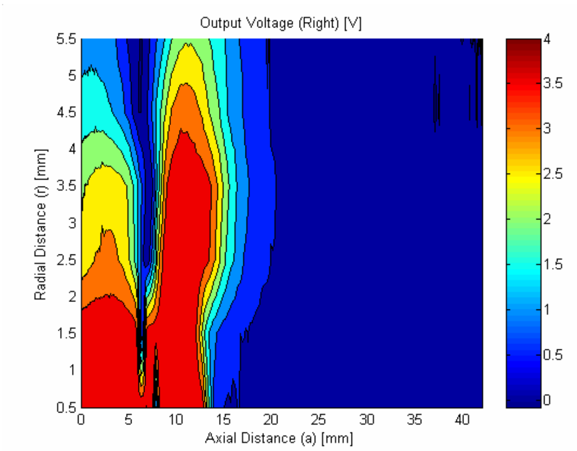

(h) Right sensor output when b = 0 [mm]

Figure 3.6 Results of GMR sensor tests with disc magnet (to continue)

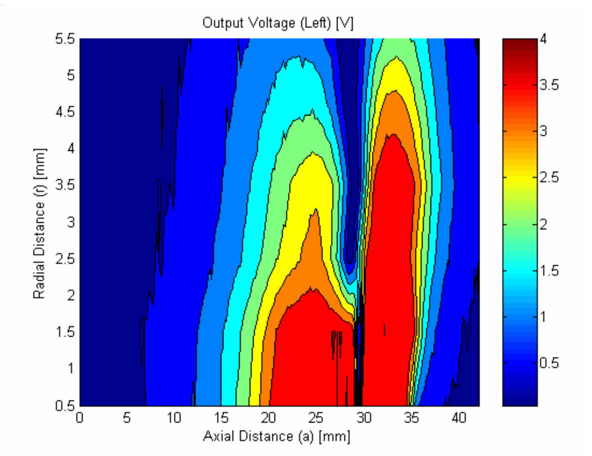

(i) Left sensor output when b = 1 [mm]

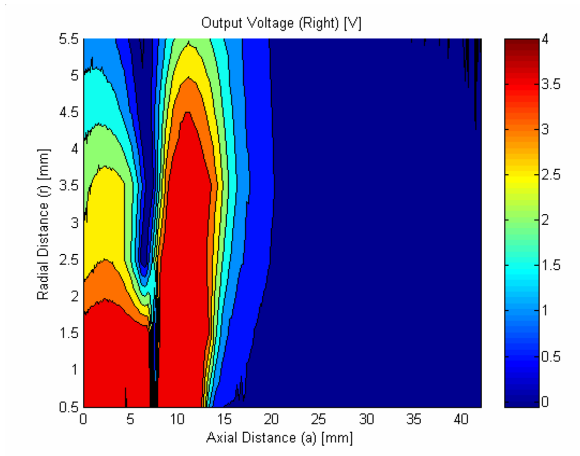

(j) Right sensor output when b = 1 [mm]

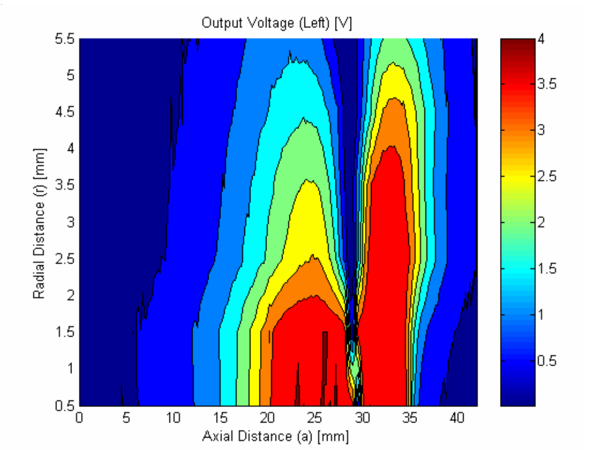

(k) Left sensor output when b = 2 [mm]

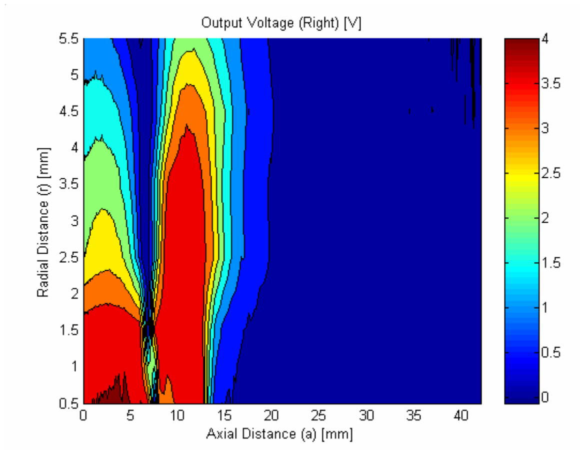

(l) Right sensor output when b = 2 [mm]

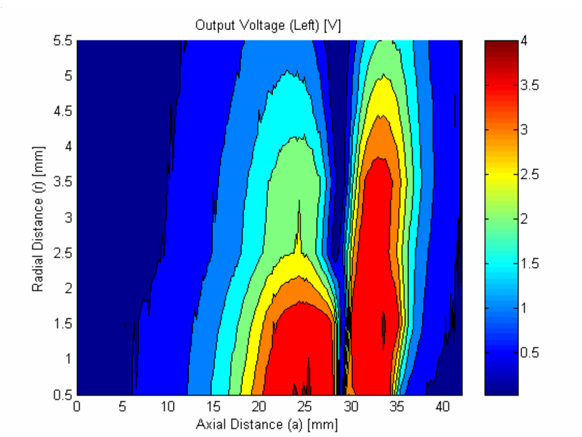

(m) Left sensor output when b = 3 [mm]

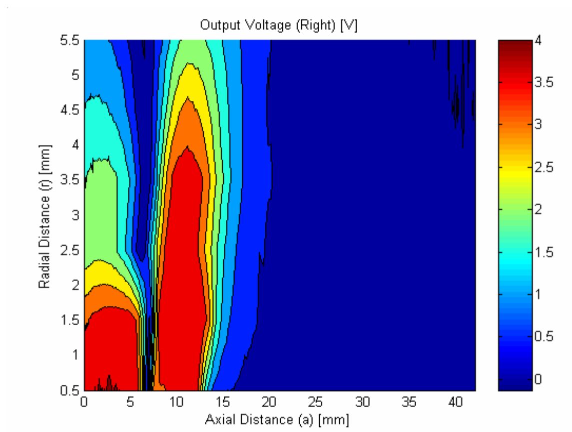

(n) Right sensor output when b = 3 [mm]

Figure 3.6 Results of GMR sensor tests with disc magnet (velocity = 20 [mm/s])

Region of operation is defined in the linear zone, as can be seen from **Figure 3.7**.

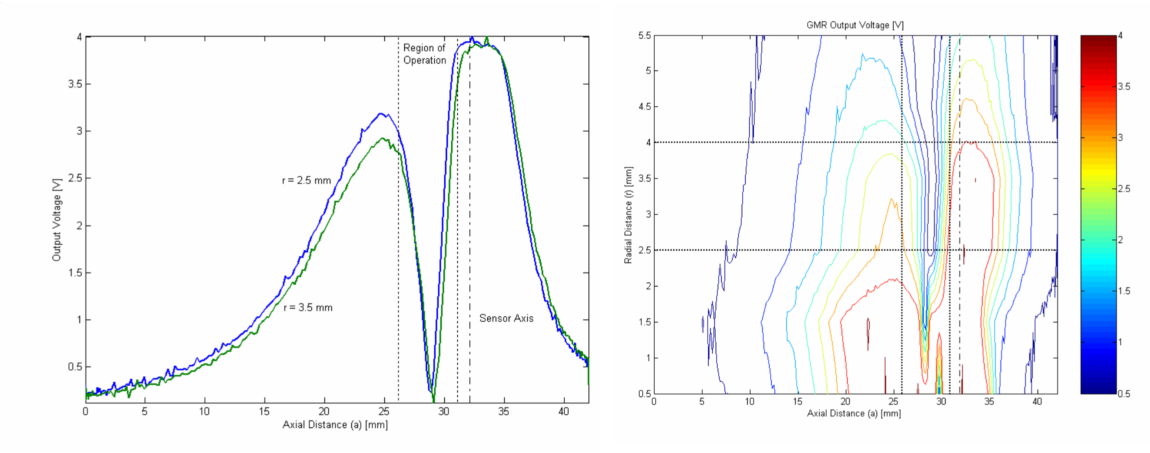

(a) Left sensor output when b = 0 [mm] **(b)** Contour plot for b = 0 [mm]

Figure 3.7 Region of operation when GMR sensor used with disc magnet

As can be seen from Figure 3.6, center of the GMR sensor located at right is at 10 mm. and center of the GMR sensor located at left side is at 32 mm. respectively. In accordance with the acquired data, defining radial distance between 2.50 – 4.00 mm. and b as zero, will not affect output voltages of GMR sensor within the region of operation. In that zone, voltage changes are close to each other. After those tests, as can be seen from Figure 3.7, operation region is defined precisely and the magnets are located within the defined locations as per Figure 3.7(a). Probe tests are performed via the data obtained during those tests dramatically.

3.3 Conclusion

In this chapter, GMR sensor tests and test configurations are described Since the behaviour of those sensors cannot be known at the beginning, tests are performed via those sensors in order to see their characteristics more precisely. Thus, performed tests, configuration of the test setup and results obtained from those sensors are also indicated in this chapter. As a result, acquired data and the graph showing us where to operate (Figure 3.7) will be the key parameter during the probe tests dramatically. More importantly, the results obtained in this chapter will be used during the design of the probe dramatically. Length of the magnet plate holder shaft is determined after the GMR sensor tests.

CHAPTER 4

PROBE DESIGNS

4.1 Introduction

In this thesis, different types of touch trigger probes are designed for the measurement processes in order to make the inspection more ideal for three dimensional prismatic parts and known geometries. All of the designed probes have the same sensing concept together with the same mechanical concept. In other words, the displacement of the tip of the stylus is transmitted to the magnet plate, where the magnets are fixed on it. Basically displacement values obtained from the tip is transferred to the magnet plate; so through the proper mounting of the Giant Magnetoresistor (GMR) sensors and magnets in the probe body, the probe will act as a touch trigger probe. Major differences of the designs are the fixing concept of the spring steel, location of the GMR sensors and the modifications carried out for the robust manufacturing processes.

4.2 Major Probe Design-1

Major design also known as the manufactured design consists of the parts as illustrated in Figures 4.1 – 4.2 – 4.3 and 4.4.

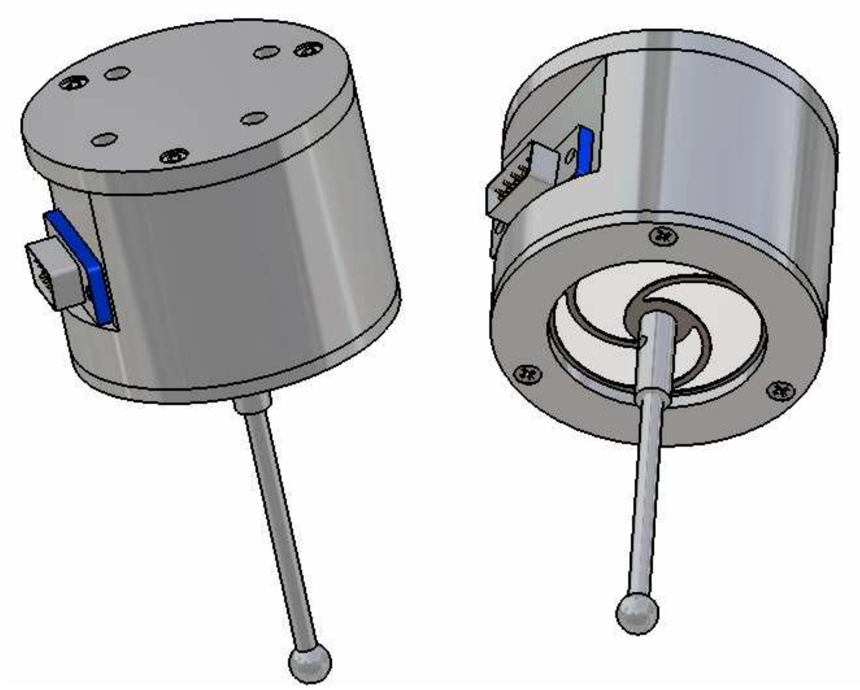

Figure 4.1 Assembly of the major design-1 from different points of view

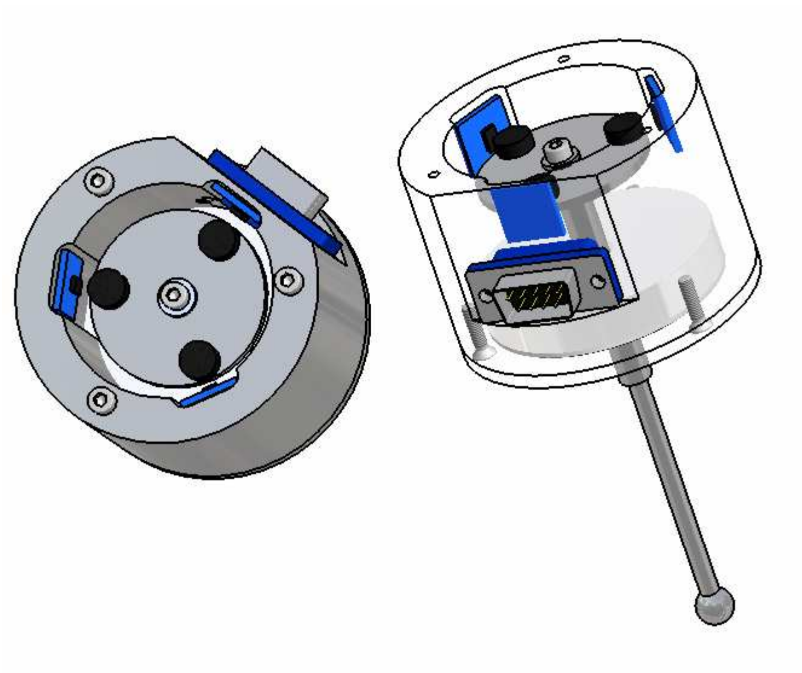

Figure 4.2 Inside view of the major probe design-1

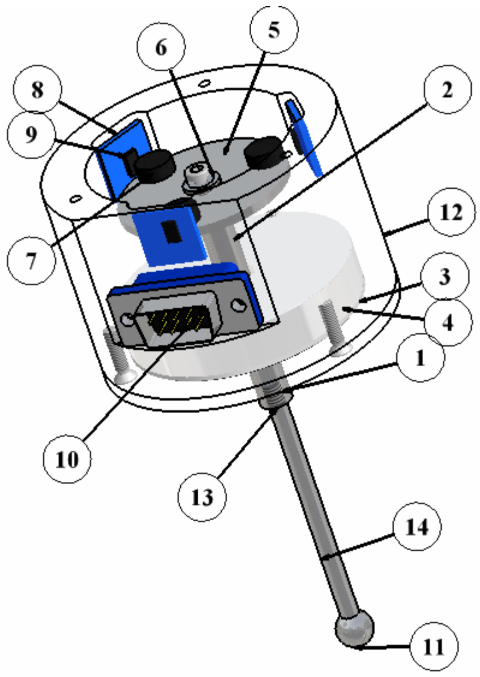

MAJOR DESIGN PART LIST		
ITEM	QTY	PART NUMBER
1	1	Bottom Lid
2	1	Top Portion of the Probe Shaft
3	1	The Ring
4	1	Polyamide
5	1	Magnet Plate
6	1	Washer
7	3	Disc Magnet
8	3	GMR Sensor PCB
9	3	GMR Sensor (AA006-02E Chip)
10	1	D-SUB9 Connector with Ribbon Cable
11	1	The Ball
12	1	Main Probe Body
13	1	Bottom Portion of the Probe Shaft-1
14	1	Bottom Portion of the Probe Shaft-2

Figure 4.3 Major Design-1 Part List-1

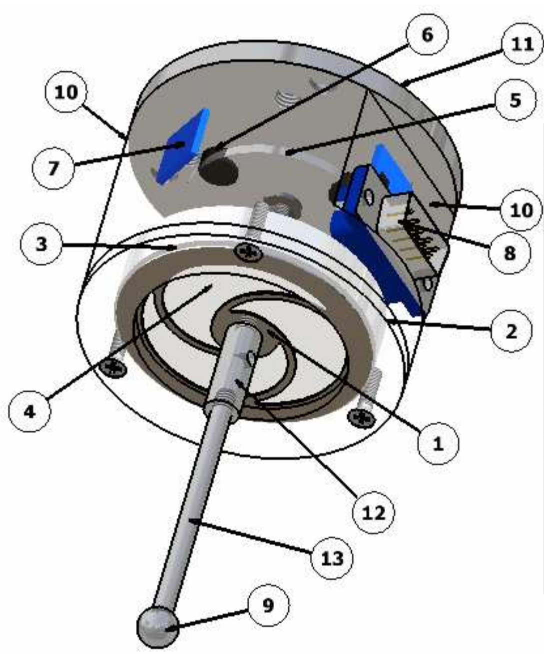

MAJOR DESIGN PART LIST		
ITEM	QTY	PART NUMBER
1	1	Spring Steel
2	1	Bottom Lid
3	1	The Ring
4	1	Polyamide
5	1	Magnet Plate
6	3	Disc Magnet
7	3	GMR Sensor PCB
8	1	D-SUB9 Connector with Ribbon cable
9	1	The Ball
10	1	Main Probe Body
11	1	Top Lid
12	1	Bottom Portion of the Probe Shaft-1
13	1	Bottom Portion of the Probe Shaft-2

Figure 4.4 Major Design-1 Part List–2

In accordance with the Figures 4.1 – 4.2 – 4.3 – 4.4, since the ball is attached to the bottom portion of the probe shaft-2, when the tip (ball) of the probe contacts with the surface of the workpiece the probe shaft (stylus shaft) starts to bend. Due to the bending behaviour of the stylus shaft, the arms of the spring steel (helical beams) starts to move up and down in accordance with the direction of the applied force to the stylus tip. The basic function of this design is to transmit the displacement amount of the stylus tip (ball) to the magnet plate also known as the sensing stage of the design. Through three Giant Magnetoresistor (GMR) sensors placed at the grooves at the main probe body, the displacement value of the center of the magnet plate can be easily found. Since the amount of the displacement value of the center of the magnet plate is known, the displacement value of the stylus tip can be obtained. The thing is that in this basic function of the probe is the concentricity of the axes of the components that are transmitting the displacement values. Due to the eccentric mounting of those parts, this kind of failure will affect the accuracy, functionality of the system in a bad way.

As can be seen from the Figures 4.3 and 4.4, due to the small value of the diameter of the stylus shaft, the bottom portion of the stylus shaft is manufactured in two parts. The ball is attached to the bottom portion of the probe shaft-2. The spring steel (having thicknesses; 0.20 – 0.30 – 0.40 mm) manufactured via water-jet is placed on the bottom portion of the probe shaft-1 and the center of the spring steel is fixed via the top portion of the probe shaft. Since the spring steel is a transition zone between the top and bottom parts of the probe shafts (stylus shafts), it has to be fixed peripherally. This is achieved by the polyamide, the ring, main probe body, bottom lid and three screws. The thickness of the ring that is placed on the spring steel is 1 mm. In other words, not to encounter any kind of bad scenarios during the probing action of the system, this ring and polyamide will act as security elements disabling the movement of the arms of the spring steel more than 1 mm in Z - direction. Although, the hole in the polyamide will stop the collision of the magnet plate and GMR sensor chip.

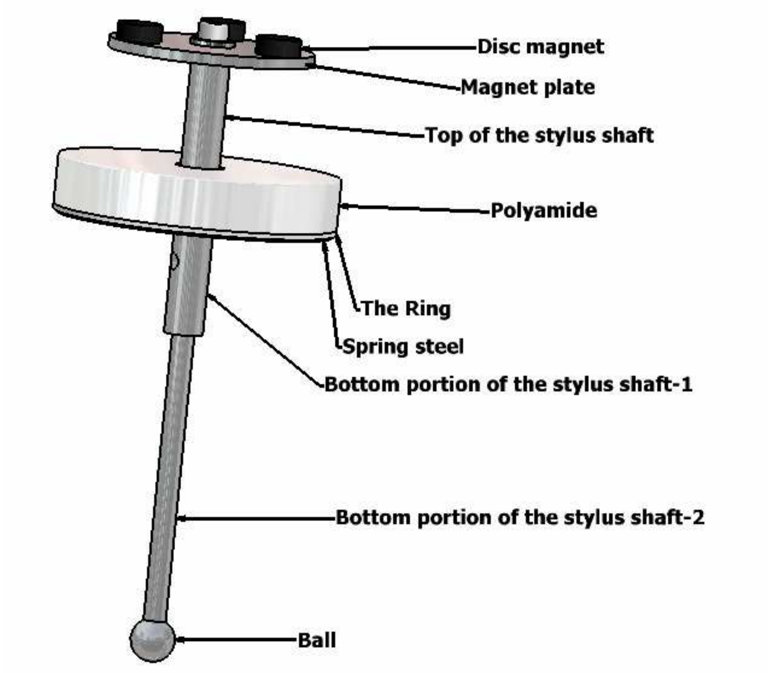

Figure 4.5 The basis of the major probe designs

As can be seen from the Figure 4.5, the movement of the stylus tip can be transferred to the magnet plate via the above-illustrated system. In order to avoid the ambiguities coming from the design, the magnets are placed on the magnet plate as per the results obtained from the tests to determine the directional sensitivity of the GMR AA006-02E sensor (characteristics of this chip is given in Appendix B.1). Those GMR sensors are soldered on to their PCBs and put at the grooves of the main probe body designed for them. Furthermore, the main probe body comprises another groove for the D-SUB9 connection for the probe electronic interface. The grooves for the GMR sensors also carry the cables coming from them to the GMR signal conditioner board. The GMR sensors are placed at their grooves by hot silicon.

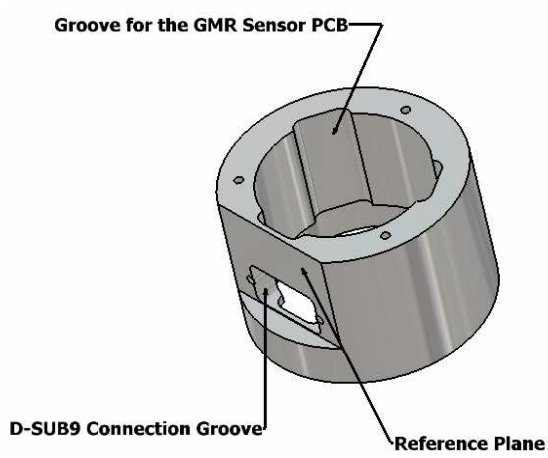

Figure 4.6 Main Probe Body

As can be seen from the Figure 4.6, the flat plane at the D-SUB9 connection zone is named as a reference plane. This flat plane is used to determine the perpendicularity of the plane of the spring steel. This is important for the performance of the system and as well as the mechanical repeatability of the system. Since the whole probe is tested on 3-axes CNC EDM, the top lid consists of four screw holes. By virtue of those holes, the probe is fixed to the EDM body.

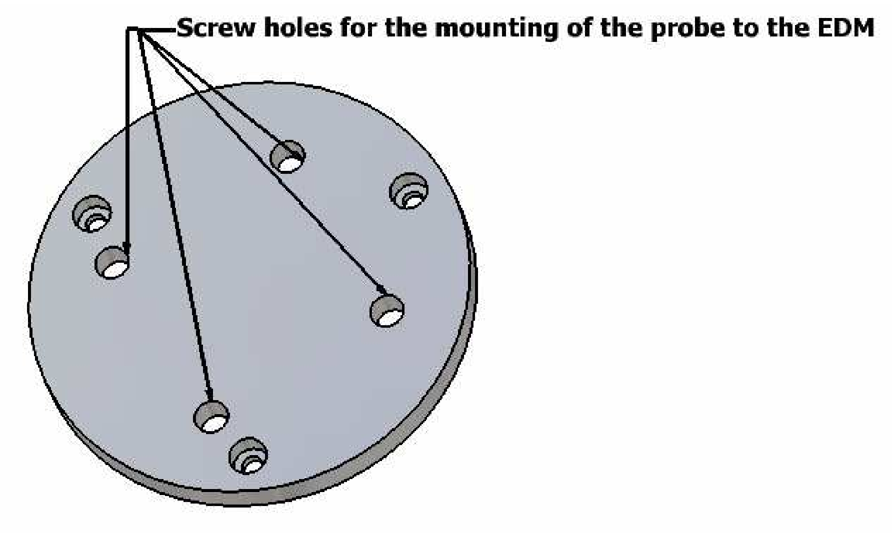

Figure 4.7 Top lid of the major probe designs

4.3 Major Probe Design–2

This design comprises the same parts as the major design–1. The main difference of this design is the location of the GMR sensors in the probe body. Since all the parts constituting the major design–1 are manufactured in two pieces, by changing the location of the GMR sensors in major design–1, one can obtain a new probe system, called as major design–2 that has different sensing stage characteristics.

During the GMR sensor tests, it is observed that the GMR sensor and the disc magnet settlement configuration used in the major design–2 gave reasonable results. Due to those results, changing the settlement configuration of the GMR sensor and the disc magnets, several different probe designs can be obtained with the same parts.

So in accordance with those results obtained during the tests, a new type of probe system utilizing different sensing characteristic of the GMR sensor came on the scene. Thereby, the results obtained from the major design–2, can be compared with the results coming from the first design, to see the best relevant probe system utilizing the GMR sensor technology.

As can be seen from Figure 4.8, in this design, GMR sensor PCBs are located under the top lid by hot silicon. As compared with the major design–1, the main difference is the location of the GMR sensors. The basis of the kinematics of the system and fixing method of the spring steel peripherally are same as the major design-1. So changing the location of the GMR sensors will result a new type of GMR sensor and disc magnet settlement configuration in this design affecting the accuracy, functionality and the repeatability of the system dramatically.

The main purpose of constructing this type of system is to observe the GMR sensor characteristics and responses more properly and to see how the whole system will function as a touch trigger probe system compared with other commercial touch trigger probes that are already in use in the industry.

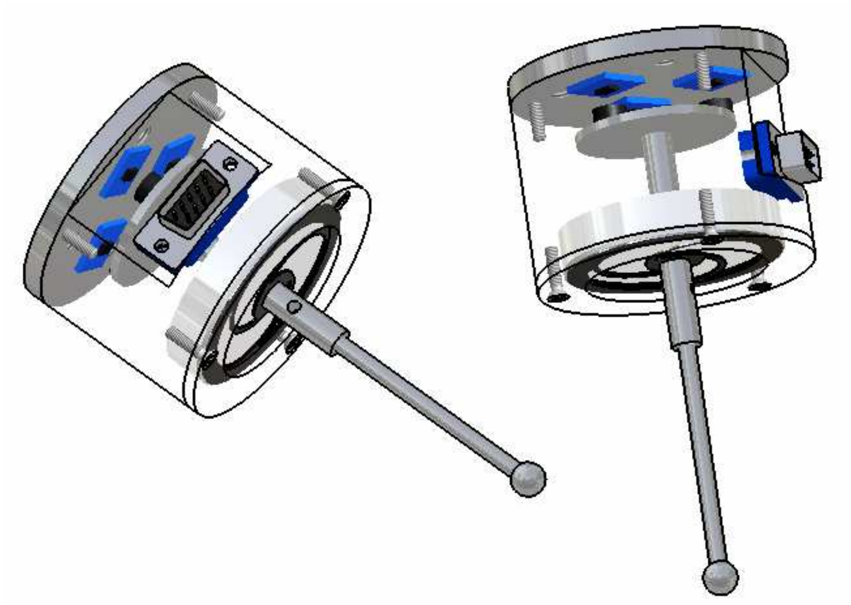

Figure 4.8 Assembly of the major design-2 from different points of view

4.4 Alternative Probe Design–1

Several probe prototypes are designed for the CMM applications and the probe designs under this headline cover different structural probes. Similarly, the functionality and the kinematics of all designed probes are same.

As can be seen from Figure 4.9, in this design, an inner ring is used to fix the locations of the GMR sensors inside the main probe body. However, while mounting the top lid to the main probe body, inner ring can rotate in an undesired way. In order to avoid this problem, a pin hole is drilled for both of the top lid and the inner ring. By virtue of this pin hole, the GMR sensors will maintain their locations without any change which will affect the probe's functionality and accuracy respectively.

Through the guide of the top lid, inner ring forces the ring and the spring steel is fixed more properly from its peripherals. Bottom lid does not play any role in the fixing phase of the spring steel.

The main advantage of this system can be listed as follows:

1) Since the length of the inner ring is wide enough, GMR sensor locations can be altered in order to obtain the best operation configuration,
2) Undesired rotation of the inner ring can be stopped by a pin,
3) During screwing the top lid to its place, through its guide, inner ring forces the polyamide more tightly and spring steel is fixed peripherally.

The disadvantage of this system can be listed as follows:

1) Complex manufacturing processes, (vital tolerances need to be considered during the manufacturing processes).

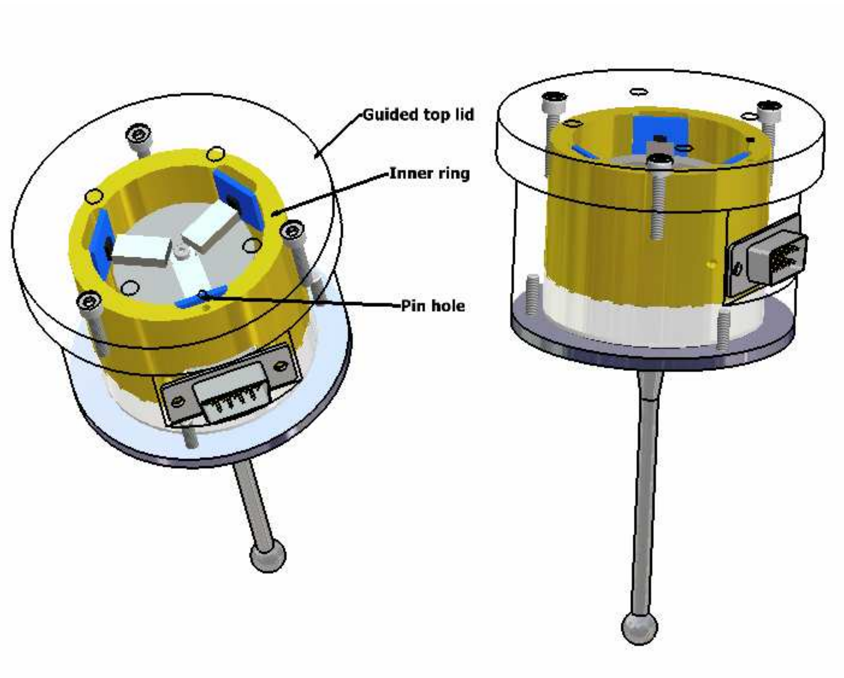

Figure 4.9 Assembly of the alternative design-1 from different points of view

4.5 Alternative Probe Design–2

Similarly, this design uses the same inner ring system explained in the previous section. The prominence of this design is the integration of the system, in other words the dimensions are optimized. Furthermore, bottom lid appeared in the previous major and alternative designs was not used in this design. Since clamping is done by the top lid, inner ring and the polyamide; there is no need to mount an extra part which is the bottom lid in this design. As can be seen from Figure 4.10, the top lid has no guide in this design and set screws are used to fix the inner ring in its place more properly. Three set screws are mounted peripherally in order to avoid an undesired rotation of the inner ring inside one-piece main probe body.

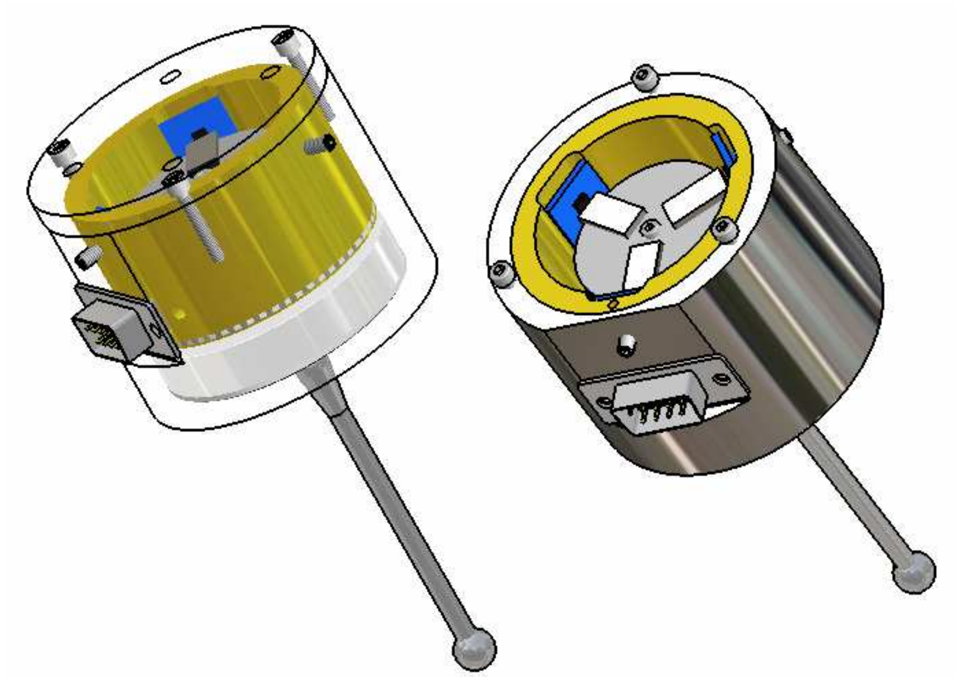

Figure 4.10 Assembly of the alternative design-2 from different points of view

The main advantage of this system can be listed as follows:

1) Since the length of the inner ring is wide enough, GMR sensor locations can be altered in order to obtain the best operation configuration,
2) Undesired rotation of the inner ring can be stopped by a pin and the set screws that are mounted peripherally,
3) During screwing the top lid to its place, inner ring forces the polyamide more tightly and spring steel is fixed peripherally,

4) One–piece main probe body.

The disadvantage of this system can be listed as follows:

1) Complex manufacturing processes, (vital tolerances need to be considered during the manufacturing processes).

4.6 Alternative Probe Design–3

The major advantage of this design is the capability to adjust the position of the GMR sensors through the screws. Again, one–piece main probe body is used in this design. By virtue of this design, the settlement of the GMR sensors and disc magnets can be optimized in order to find the relevant linear operation zone. Kinematics and the working principle of this design are same as the other previous major and alternative designs. In order to maintain the position of the adjustment screw without any change, a spring, and a set screw is used. Spring will keep the screw in its location and set screw will prevent the rotation of the screw otherwise the position of the GMR sensor will change and this case will cause an undesired results during the tests of the probe system. As can be seen from the Figure 4.11, two rings are located at the top and bottom part of the polyamide in order to clamp the spring steel more tightly. Through screwing the top lid in its own place, the linear adjustment guide unit will force the ring located at the top of the polyamide and as a result, the spring steel will be fixed peripherally in a one-piece main probe body.

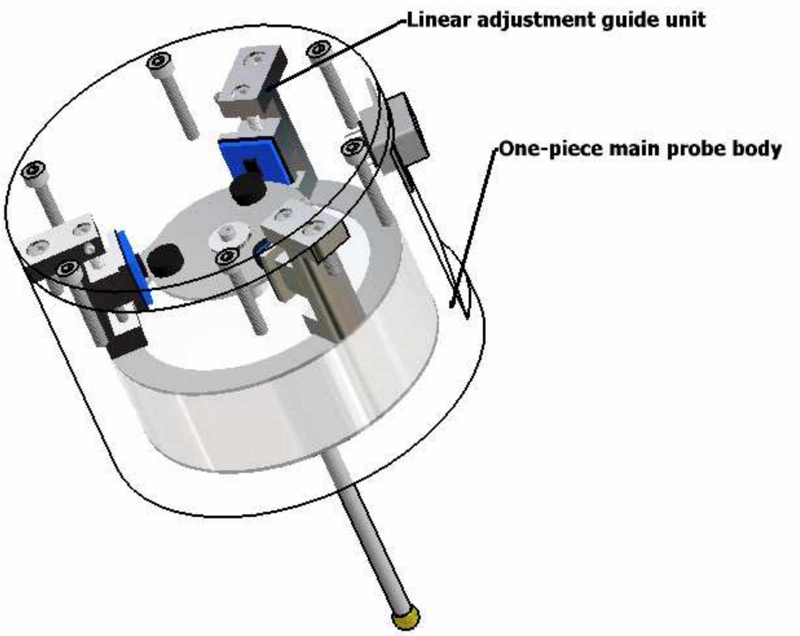

Figure 4.11 Assembly of the alternative design-3

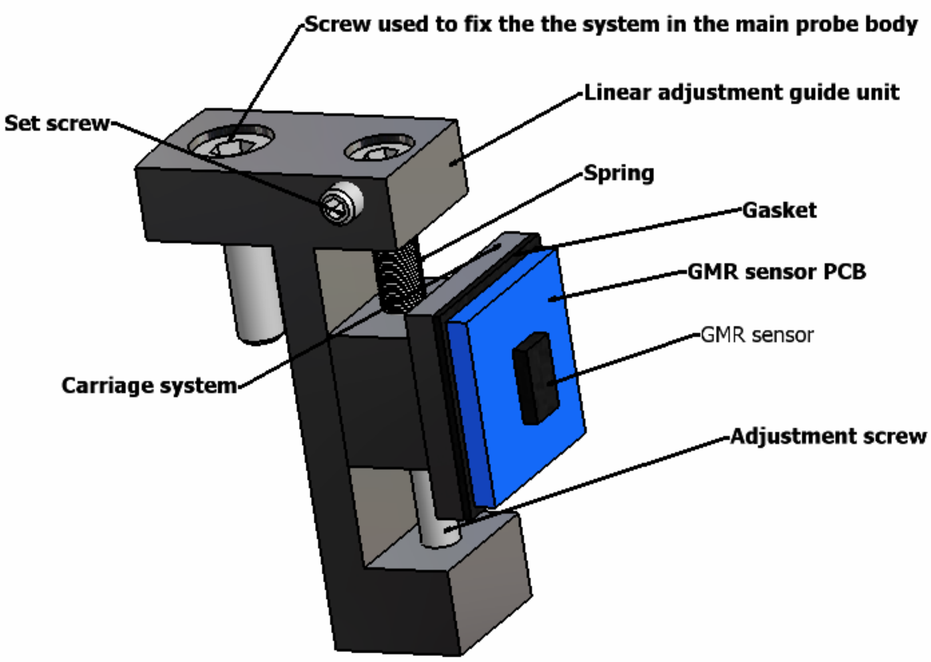

Figure 4.12 Close-up view of the linear adjustment system

The main advantage of this system can be listed as follows:

1) Through the linear adjustment unit system, vertical location of the GMR sensors can be altered in order to obtain the best operation configuration,
2) One–piece main probe body.

The disadvantage of this system can be listed as follows;

1) Complex manufacturing processes,
2) Due to the wrong screwing of the linear adjustment system in to the one-piece main probe body, GMR sensors can be located slantly which is an undesired option for the sake of the system's performance.

4.7 Alternative Probe Design–4

In this system, again a linear adjustment guide unit is used to alter the position of the GMR sensor location. In this case, extra linear adjustment units are not preferred because of their position-based sensitivity in the design. However, the utilized logic in this system actually the same as the logic used in the previous alternative design. Instead of using linear adjustment units, grooves are formed in the main probe body that will serve as a linear adjustment unit. Similar to the previous alternative design, a carriage system is used to locate the GMR sensor and PCB assembly.

The major difference of the system is the location of the disc magnets in the whole system. Unlikely to the other previous major and alternative designs, disc magnets are located in a hole at the carriage system. Furthermore, the clamping system of the spring steel also differs from other previous probe designs. In order to maintain the position of the adjustment screw without any change, a spring, and a set screw is used. Spring will keep the screw in its location and set screw will prevent the rotation of the screw otherwise the position of the GMR sensor will change and this case will cause an undesired results during the tests of the probe system.

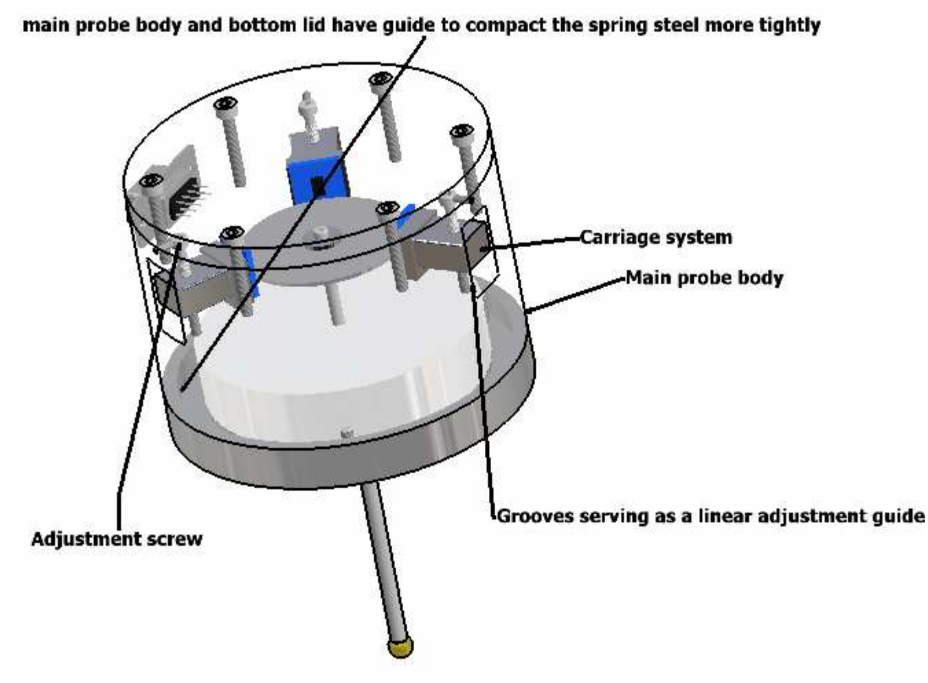

Figure 4.13 Assembly of the alternative design-4

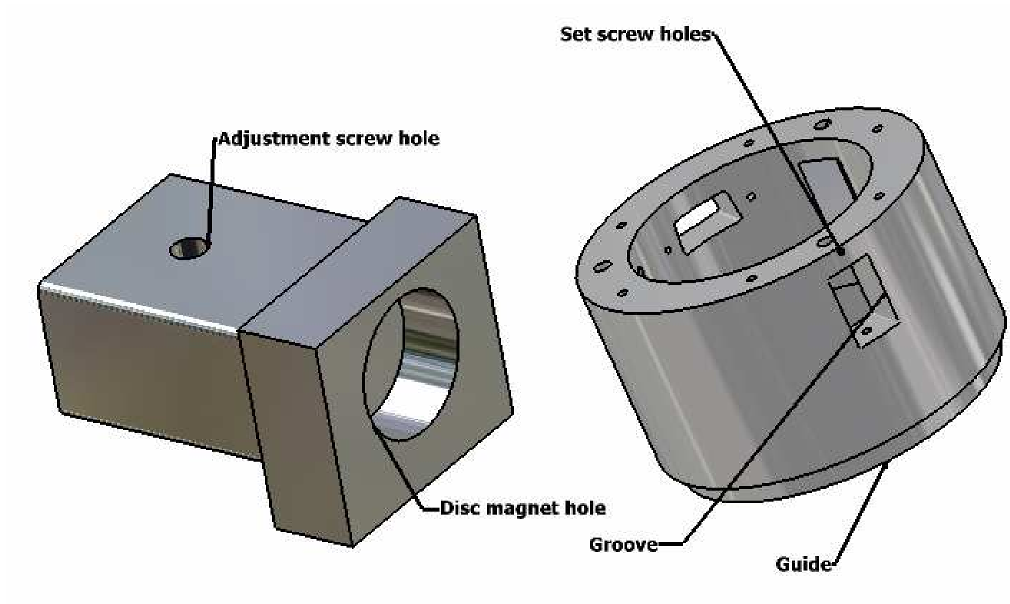

Figure 4.14 Close-up views of the main probe body and the carriage system

The main advantage of this system can be listed as follows:

1) By virtue of the grooves and the carriage system, vertical location of the GMR sensors can be altered in order to obtain the best operation configuration.

The disadvantage of this system can be listed as follows:

1) Complex manufacturing processes.

4.8 Alternative Probe Design–5

Another type of probe system is designed for the CMM applications that has different structural basis. Similar to the previous alternative design, grooves are formed around the main probe body functioning as a linear adjustment guide and a carriage system is used to locate the GMR sensor and PCB assembly. In this case, D-SUB9 connector is located at the top lid where extra connection parts are found. Those extra connection parts will be used to mount the probe system on to a flat table.

In order to maintain the position of the adjustment screw without any change, a spring, and a set screw is used. Spring will keep the screw in its location and set screw will prevent the rotation of the screw otherwise the position of the GMR sensor will change and this case will cause an undesired results during the tests of the probe system. The major difference of the system is the location of the disc magnets in the whole system. Unlikely to the other previous major and alternative designs, disc magnets are located in a hole at the carriage system.

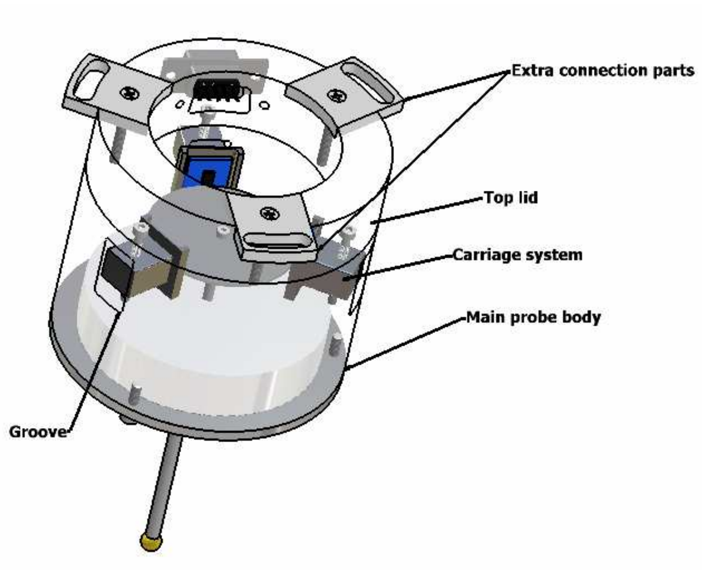

Figure 4.15 Assembly of the alternative design-5

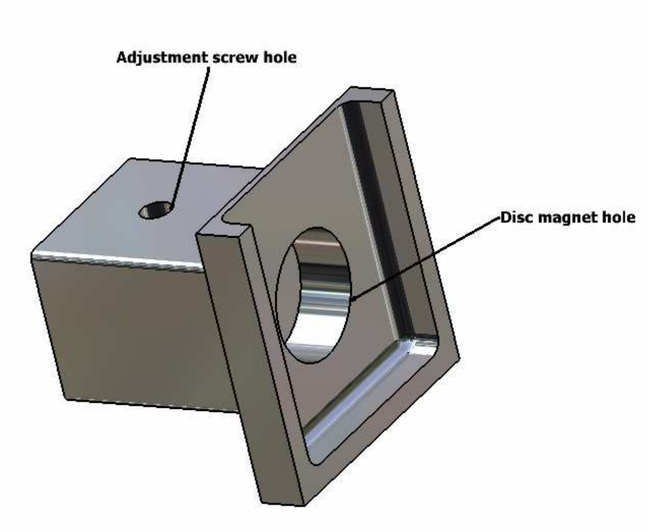

Figure 4.16 Close-up view of the carriage system

The main advantage of this system can be listed as follows:

1) By virtue of the grooves and the carriage system, vertical location of the GMR sensors can be altered in order to obtain the best operation configuration.

The disadvantage of this system can be listed as follows:

1) Complex manufacturing processes,
2) Complex cabling procedures.

4.9 Finite Element Analysis of Spring Plates

Finite Element Analysis (FEA) is performed in order to determine the most relevant geometry for the spring steel acting as the basis of the design. Various types of geometry analysis are carried out for the optimum performance of the probe. During the analysis, observed parameters are the flexibility of the designed arms and the movement of the center of the geometry. Considering the kinematical constraints, mostly the designs having the three arms are observed during the Finite Element Analysis. The results obtained from those analyses are given in Tables 4.1, 4.2, 4.3 and 4.4 in a tabulated format. For Table 4.1**,** applied force in X and Y directions is 0.20 N., in Z direction the applied force is 1.00 N. Max. Stress is calculated via Von Misses method.

Table 4.1 Results obtained from the analysis

	Force Axes	Stylus tip disp. (μm)	Magnet Plate disp. (μm)	k (N/m)	Max. Stress (MPa)
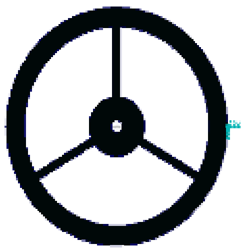	+X	1054.71	595.56	189.63	90.21
	-X	1054.71	595.56	189.62	90.20
	+Y	1057.54	596.17	189.11	101.78
	-Y	1057.54	596.17	189.11	101.78
	Z	132.32	132.32	7557.14	62.77
	Force Axes	**Stylus tip disp. (μm)**	**Magnet Plate disp. (μm)**	**k (N/m)**	**Max. Stress (MPa)**
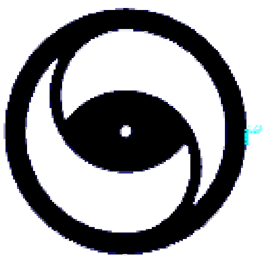	+X	1655.42	945.12	120.81	122.94
	-X	1655.42	945.12	120.81	122.94
	+Y	3260.32	1880.40	34.34	157.19
	-Y	3260.32	1880.40	34.34	157.19
	Z	174.29	174.29	5737.37	87.59

Table 4.1 (Continued)

	Force Axes	Stylus tip disp. (μm)	Magnet Plate disp. (μm)	k (N/m)	Max. Stress (MPa)
	+X	1936.46	1108.01	103.28	130.74
	-X	1936.46	1108.01	10328	130.74
	+Y	4964.44	2873.73	40.28	137.73
	-Y	4964.44	2873.73	40.28	137.73
	Z	294.09	294.09	3400.25	113.63

	Force Axes	Stylus tip disp. (μm)	Magnet Plate disp. (μm)	k (N/m)	Max. Stress (MPa)
	+X	2406.98	1383.73	83.09	245.00
	-X	2406.98	1383.73	83.09	245.00
	+Y	2409.61	1384.22	83.00	251.19
	-Y	2409.61	1384.22	83.00	251.19
	Z	227.28	227.28	4399.85	109.52

Table 4.1 (Continued)

<table>
<tr><td rowspan="6">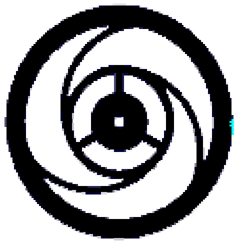</td><th>Force Axes</th><th>Stylus tip disp. (μm)</th><th>Magnet Plate disp. (μm)</th><th>k (N/m)</th><th>Max. Stress (MPa)</th></tr>
<tr><td>+X</td><td>2285.49</td><td>1312.82</td><td>87.50</td><td>150.98</td></tr>
<tr><td>-X</td><td>2285.49</td><td>1312.82</td><td>87.50</td><td>150.98</td></tr>
<tr><td>+Y</td><td>2288.22</td><td>1313.38</td><td>87.40</td><td>148.84</td></tr>
<tr><td>-Y</td><td>2288.22</td><td>1313.38</td><td>87.40</td><td>148.84</td></tr>
<tr><td>Z</td><td>328.26</td><td>328.26</td><td>3046.34</td><td>107.32</td></tr>
<tr><td rowspan="6"></td><th>Force Axes</th><th>Stylus tip disp. (μm)</th><th>Magnet Plate disp. (μm)</th><th>k (N/m)</th><th>Max. Stress (MPa)</th></tr>
<tr><td>+X</td><td>4053.56</td><td>2342.97</td><td>49.33</td><td>230.21</td></tr>
<tr><td>-X</td><td>4053.56</td><td>2342.97</td><td>49.33</td><td>230.21</td></tr>
<tr><td>+Y</td><td>4054.30</td><td>2342.36</td><td>49.33</td><td>224.11</td></tr>
<tr><td>-Y</td><td>4054.31</td><td>2342.36</td><td>49.33</td><td>224.11</td></tr>
<tr><td>Z</td><td>531.77</td><td>531.77</td><td>1880.48</td><td>152.71</td></tr>
</table>

Table 4.1 (Continued)

	Force Axes	Stylus tip disp. (µm)	Magnet Plate disp. (µm)	k (N/m)	Max. Stress (MPa)
	+X	5001.09	2864.29	39.99	241.74
	-X	5001.09	2864.29	39.99	241.74
	+Y	19642.28	11429.94	10.18	315.01
	-Y	19642.28	11429.94	10.18	315.01
	Z	976.99	976.99	1023.54	248.63

	Force Axes	Stylus tip disp. (µm)	Magnet Plate disp. (µm)	k (N/m)	Max. Stress (MPa)
	+X	2996	1724.91	66.75	178.52
	-X	2996	1724.91	66.75	178.52
	+Y	2997.43	1724.71	66.72	176.90
	-Y	2997.43	1724.71	66.72	176.90
	Z	390.28	390.28	2562.21	103.46

Table 4.1 (Continued)

	Force Axes	Stylus tip disp. (µm)	Magnet Plate disp. (µm)	k (N/m)	Max. Stress (MPa)
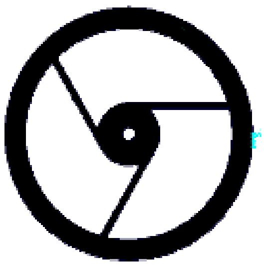	+X	1449.02	825.44	138.02	15358
	-X	1449.02	825.44	138.02	153.58
	+Y	1450.95	825.51	137.84	159.52
	-Y	1450.95	825.51	137.84	159.52
	Z	184.13	184.13	5430.78	91.94

	Force Axes	Stylus tip disp. (µm)	Magnet Plate disp. (µm)	k (N/m)	Max. Stress (MPa)
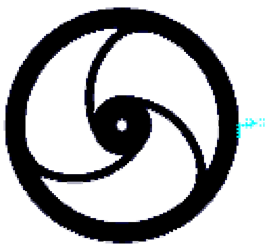	+X	1842.99	1054.99	108.51	162.79
	-X	1842.99	1054.99	108.51	162.79
	+Y	1844.24	1054.67	108.44	161.98
	-Y	1844.24	1054.67	108.44	161.98
	Z	239.49	239.49	4175.49	97.35

Table 4.2 Results obtained from the analysis (Contact Force [0.2 N] in X direction)

Analyzed Geometry	**X - direction**			
	Stem x disp. (μm)	**Up part x disp. (μm)**	**k_x (N/m)**	**Max. stress (MPa)**
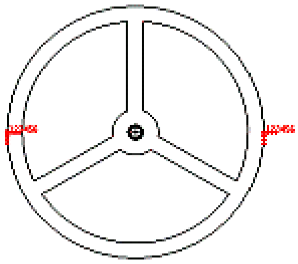 **Geometry-1**	442	201	452.48	40.4
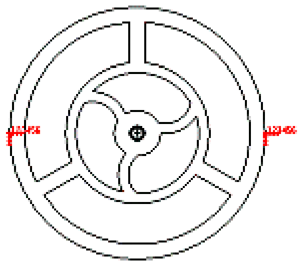 **Geometry-2**	514	237	389.10	44.4
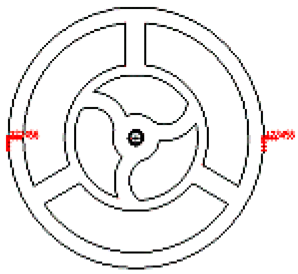 **Geometry-3**	417	188	479.61	34.3
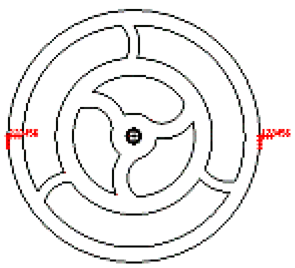 **Geometry-4**	401	180	498.75	34.2

Table 4.2 (Continued)

Analyzed Geometry	**Stem x disp. (μm)**	**Up part x disp. (μm)**	**k_x (N/m)**	**Max. stress (MPa)**
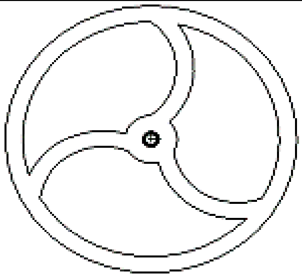 **Geometry-5**	462	211	432.9	41.6
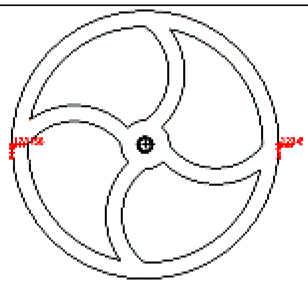 **Geometry-6**	359	159	557.10	30.3
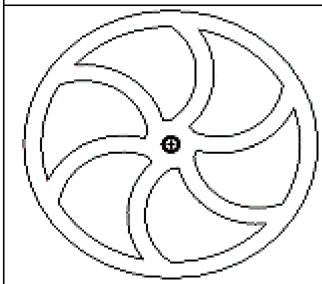 **Geometry-7**	263	111	760.45	25.3
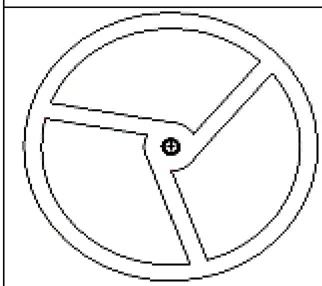 **Geometry-8**	454	207	440.53	46.4

Table 4.2 (Continued)

Analyzed Geometry	Stem x disp. (μm)	Up part x disp. (μm)	k_x (N/m)	Max. stress (MPa)
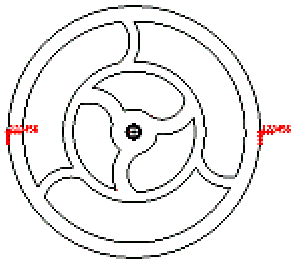 **Geometry-9**	464	212	431.03	34.5
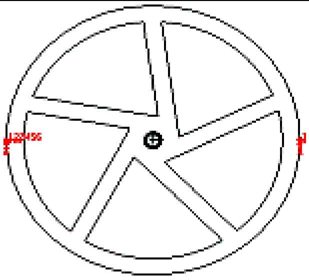 **Geometry-10**	294	126	680.27	31.3
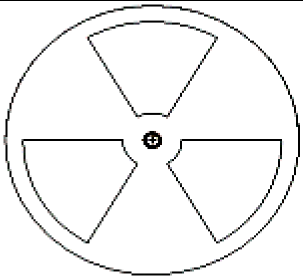 **Geometry-11**	192	75	1041.66	26
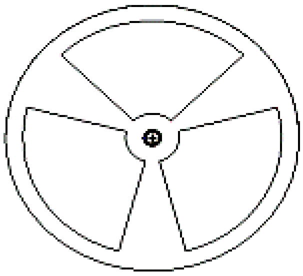 **Geometry-12**	321	140	623.05	35.5

Table 4.2 (Continued)

Analyzed Geometry	Stem x disp. (μm)	Up part x disp. (μm)	k_x (N/m)	Max. stress (MPa)
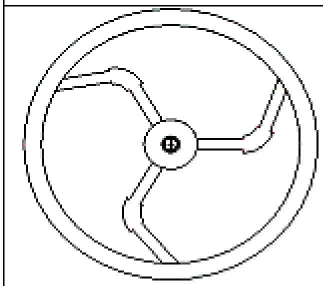 **Geometry-13**	2220	1100	90.09	156
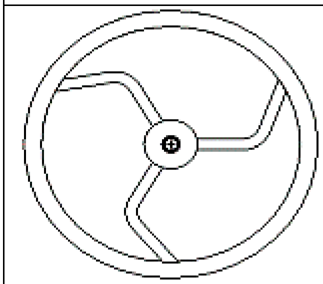 **Geometry-14**	2370	1170	84.39	206

Table 4.3 Results obtained from the analysis (Contact Force [0.2 N] in Y direction)

Analyzed Geometry	Y - direction			
	Stem y disp. (μm)	Up part y disp. (μm)	k_y (N/m)	Max. stress (MPa)
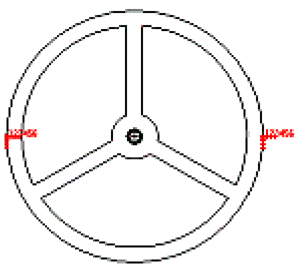 **Geometry-1**	442	201	452.49	43.7

Table 4.3 (Continued)

Analyzed Geometry	**Stem y disp. (μm)**	**Up part y disp. (μm)**	**k_y (N/m)**	**Max. stress (MPa)**
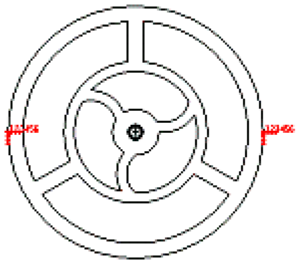 **Geometry-2**	516	238	387.60	45.5
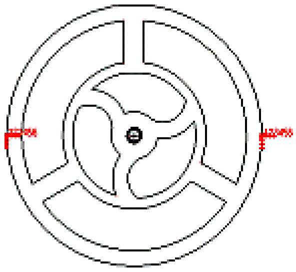 **Geometry-3**	417	188	479.62	31.1
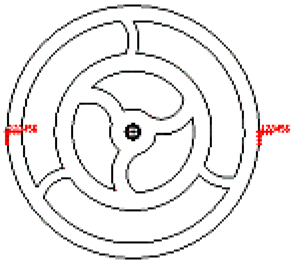 **Geometry-4**	464	212	431.03	33.4
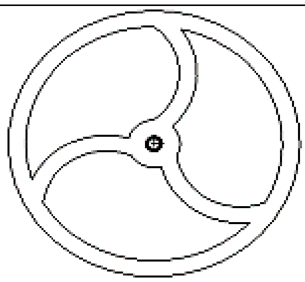 **Geometry-5**	401	180	498.75	31.3

Table 4.3 (Continued)

Analyzed Geometry	**Stem y disp. (μm)**	**Up part y disp. (μm)**	**k_y (N/m)**	**Max. stress (MPa)**
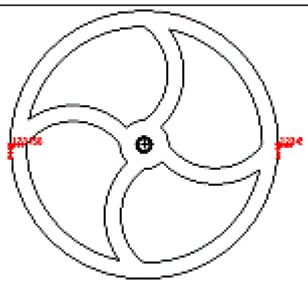 **Geometry-6**	464	212	431.03	40.5
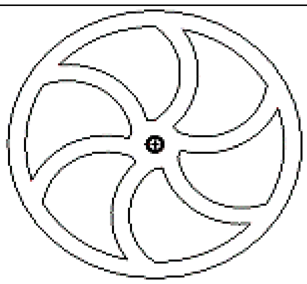 **Geometry-7**	359	159	557.11	31.3
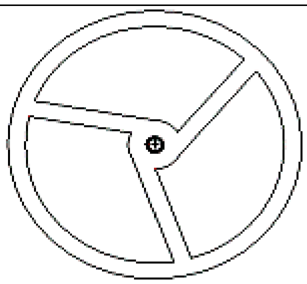 **Geometry-8**	263	111	760.46	25.8
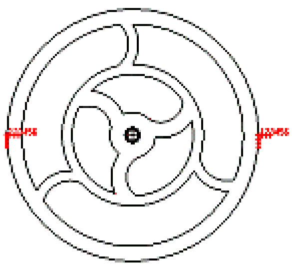 **Geometry-9**	454	207	440.53	18

Table 4.3 (Continued)

Analyzed Geometry	Stem y disp. (μm)	Up part y disp. (μm)	k_y (N/m)	Max. stress (MPa)
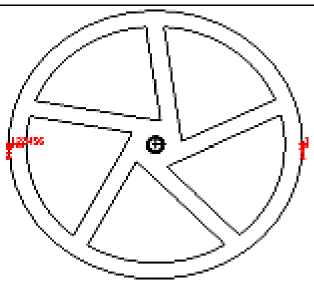 **Geometry-10**	294	127	680.27	32
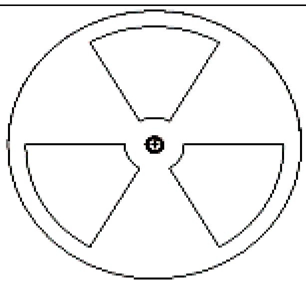 **Geometry-11**	192	75	1041.66	25.6
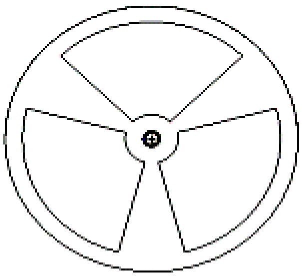 **Geometry-12**	321	140	623.05	42.9
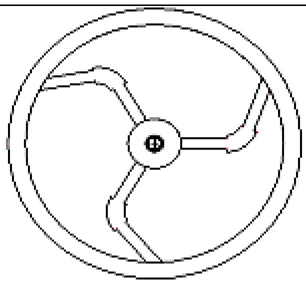 **Geometry-13**	2280	1120	87.72	201

Table 4.3 (Continued)

Analyzed Geometry	Stem y disp. (μm)	Up part y disp. (μm)	k_y (N/m)	Max. stress (MPa)
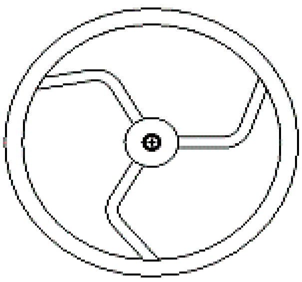 Geometry-14	2370	1170	84.4	207

Table 4.4 Results obtained from the analysis (Contact Force [1 N] in Z direction)

Analyzed Geometry	Z - direction			
	Stem z disp. (μm)	Up part z disp. (μm)	k_z (N/m)	Max. stress (MPa)
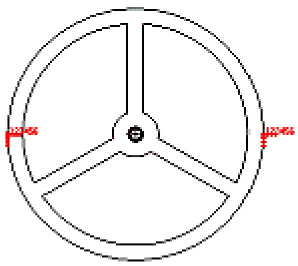 Geometry-1	40.3	40.3	24813.9	21.9
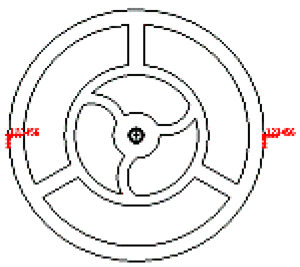 Geometry-2	38.9	38.9	25706.94	19.5

Table 4.4 (Continued)

Analyzed Geometry	**Stem z disp. (μm)**	**Up part z disp. (μm)**	**k_z (N/m)**	**Max. stress (MPa)**
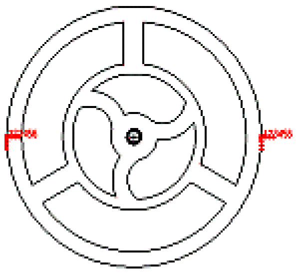 **Geometry-3**	32.1	32.1	31152.65	17.3
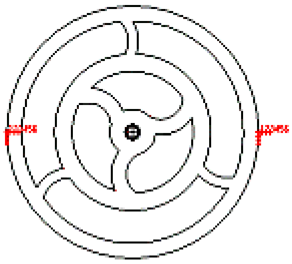 **Geometry-4**	39.1	39.1	25575.45	22.7
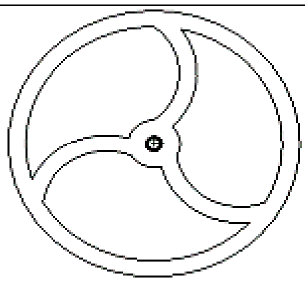 **Geometry-5**	32.2	32.2	31055.9	19.1
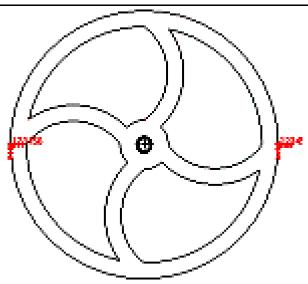 **Geometry-6**	42	42	23809.52	22

Table 4.4 (Continued)

Analyzed Geometry	Stem z disp. (µm)	Up part z disp. (µm)	k_z (N/m)	Max. stress (MP3)
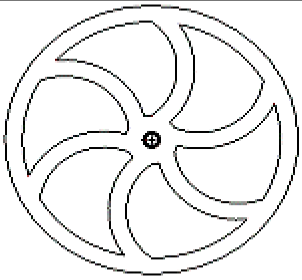 **Geometry-7**	31	31	32258.06	16.5
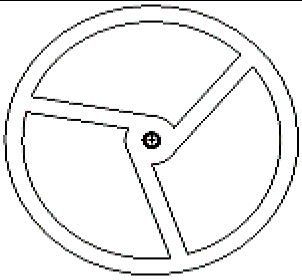 **Geometry-8**	21	21	47619.04	12.4
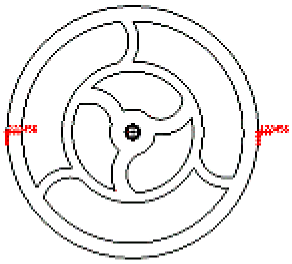 **Geometry-9**	41.4	41.4	24154.59	26.1
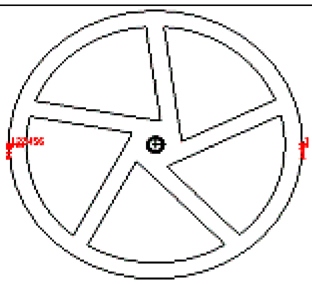 **Geometry-10**	24.4	24.4	40983.61	15.9

Table 4.4 (Continued)

Analyzed Geometry	Stem z disp. (μm)	Up part z disp. (μm)	k_z (N/m)	Max. stress (MPa)
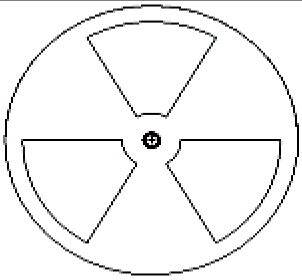 Geometry-11	11.1	11.1	90090.09	8.97
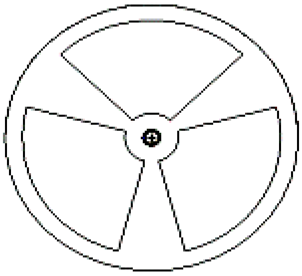 Geometry-12	21.6	21.6	46296.3	17.2
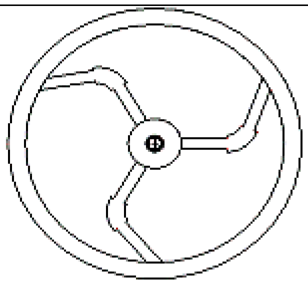 Geometry-13	222	222	4504.50	113
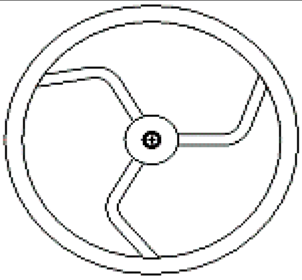 Geometry-14	228	228	4385.96	117

From those investigations, **Geometry 5** is picked up and new models are generated from this original model. **Geometry 5** is picked up, because it lets the arms of the geometry to move more smoothly in Z–direction and center of the geometry maintains its position when a force is applied to the stylus tip.

Many quantities can affect the CMM probing task such as, probing angle, probe orientation, stylus configuration, stylus material, workpiece conditions etc. Actually, due to its function on a CMM, probe can be described one of the most vital elements of the CMM dramatically. So considering those parameters, it is not easy to derive the mathematical model.

4.10 Finite Element Modeling of Probe

The method used in this section is to model the probe system through Finite Element Analysis software. By virtue of that, the fundamental characteristics of the probe is modeled and then analyzed.

Designed probe is evaluated at two sets of models. The first set involves the probing force ($F = 0.05$ N) applied at the equator of the stylus tip every 22.5 º, and in the second set 1 mm displacement values are given to the equator of the stylus tip every 22.5 º. The purpose of the first set is to see the parameters such as Max. Stress Tensor, the displacement amount of the stylus tip resulting from the applied force. Second set of investigation is carried out because during the probe tests the stylus tip will be behaved in this way. So by virtue of those results obtained from the Finite Element Model (FEM), it easy to see the important parameters and one can easily see what will happen during the real tests.

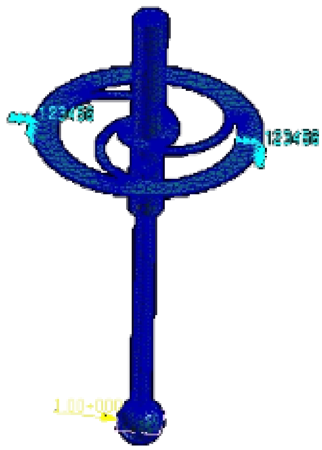

Figure 4.17 The simplified model of the designed probe

As can be seen from the above Figure 4.17, the model is fully restrained from the peripheral of the spring steel. The appropriate force is applied to the stylus tip and the corresponding displacement values are analyzed.

Table 4.5 Mechanical properties of the probe system

Material	Modulus of Elasticity (E) (MPa)	Yield Strength (MPa)	Poisson Ratio
Type 304 Stainless Steel	205000 (typical for steel)	215	0.29 (typical for steel)
CK 75 (1.1248) AISI 1080 spring steel	205000 (typical for steel)	585	0.29 (typical for steel)
AISI 1010 Grade 1000 stainless steel bearing ball	205000 (typical for steel)	303.37	0.29 (typical for steel)

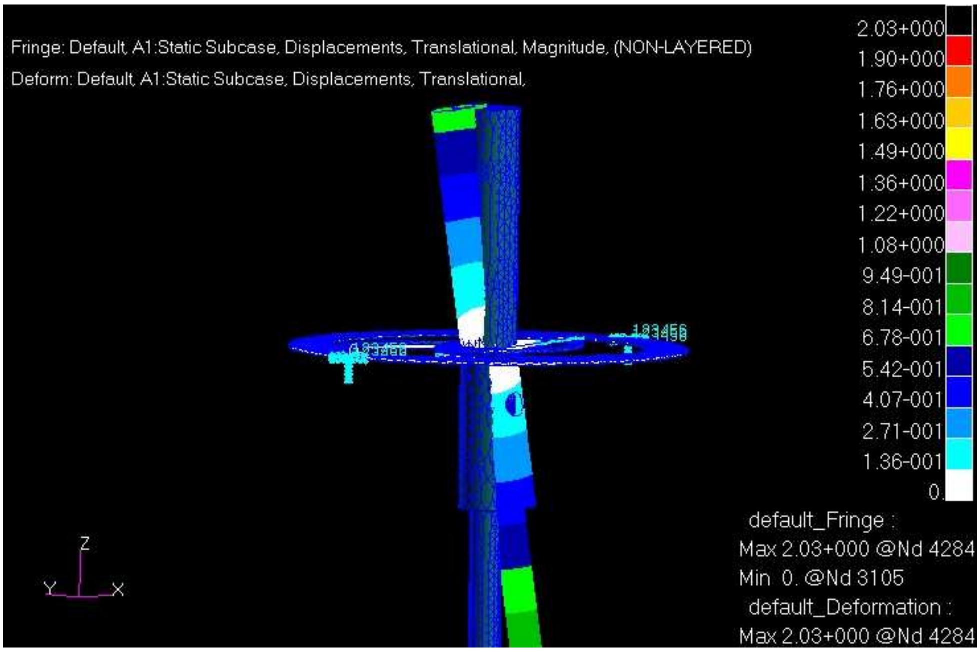

Figure 4.18 Displacement results of the center obtained from FEA tests

The result displayed in Figure 4.18 is very important for the sake of the analysis. This gives vital information of the designed probe system, such as the center of the probe system in other words the basis of the probe system constituting the kinematics of the whole system will not move under any circumstances applied during the tests. As can be seen from the fringe results of the Figure 4.18, the center zone is displayed in white color, meaning that the displacement will be zero at that zone.

Table 4.6 Results of the first test

Evaluation Angle (º)	Tip Displacement (mm)	Max. Stress Tensor [Von Misses] (MPa)
0	0.5672	49.94
22.5	0.5670	45.98
45	0.5668	42.34
67.5	0.5663	45.01
90	0.5663	43.18
112.5	0.5665	48.51
135	0.5669	47.07
157.5	0.5671	46.88
180	0.5672	49.94
202.5	0.5670	45.98
225	0.5668	42.34
247.5	0.5663	45.01
270	0.5663	43.18
292.5	0.5665	48.51
315	0.5669	47.07
337.5	0.5671	46.88

In accordance with those results, the designed model can be manufactured conveniently in order not to encounter any kind of undesired results during the test (i.e.: plastic deformation of the spring steel or probe shafts). The displacement value vs. evaluation angle graph is plotted on next page.

Max. Stress Tensor can be seen at the arms of the spring steel due to the applied force at the stylus tip.

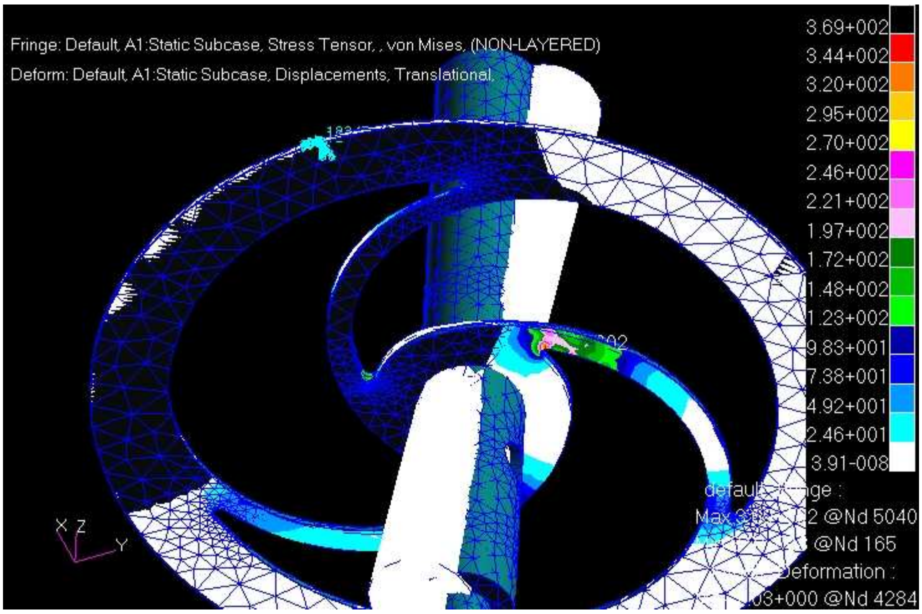

Figure 4.19 Stress Tensor, Von Misses results obtained from FEA tests

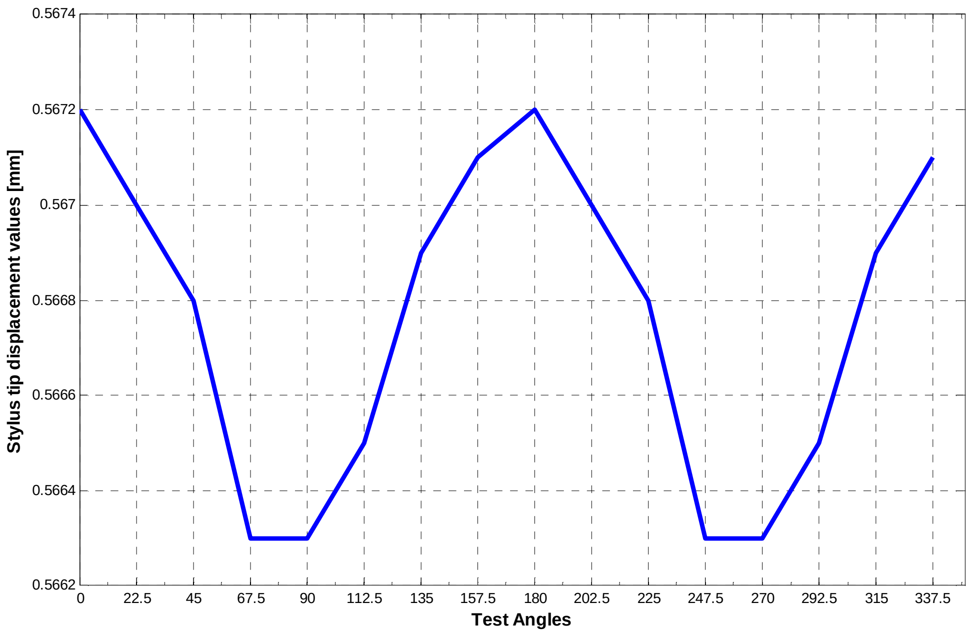

Figure 4.20 Simulated stylus displacement values at different evaluation angles

Second set of investigation is carried out via FEA in order to see the results approximately before the real probe tests. In those tests again same model is used but stylus tip is displaced 1mm from its equator every 22.5º. From those tests, one can have a chance to visualize the things happened during those tests and to see the limits of the designed probe respectively. More importantly, this type of simulation is more close to real tests of the probe system.

Table 4.7 Results of the second test

Evaluation Angle (º)	**Magnet Plate Disp. (μm)**	**Disp. of arms of spring steel in Z direction (μm)**	**Max. Stress Tensor, Nodal [Von Misses] (MPa)**
0	368.96<d<403.87	117.66	114.51
22.5	355.73<d<391.30	142.86	107.42
45	355.73<d<391.30	155.66	92.28
67.5	355.73<d<391.30	153.53	82.83
90	355.73<d<391.30	142.26	102.13
112.5	355.73<d<391.30	131.92	111.31
135	355.73<d<391.30	135.71	108.59
157.5	355.73<d<391.30	152.88	94.23
180	355.73<d<391.30	155.61	84.96
202.5	355.73<d<391.30	146.58	86.08
225	355.73<d<391.30	134.60	97.00
247.5	355.73<d<391.30	129.97	100.33
270	355.73<d<391.30	148.59	94.10
292.5	355.73<d<391.30	156.41	87.73
315	355.73<d<391.30	150.42	92.68
337.5	355.73<d<391.30	138.12	109.23
Z-Direction	1000	1000	167.94

4.11 Verification of FEA Results

In order to verify the finite element analyses results (stress result), simple calculations are carried out. New geometry is modeled as a spring steel plate and analyzed via FEA software. The geometry of the designed spring plate for the verification process can be seen in Figure 4.21.

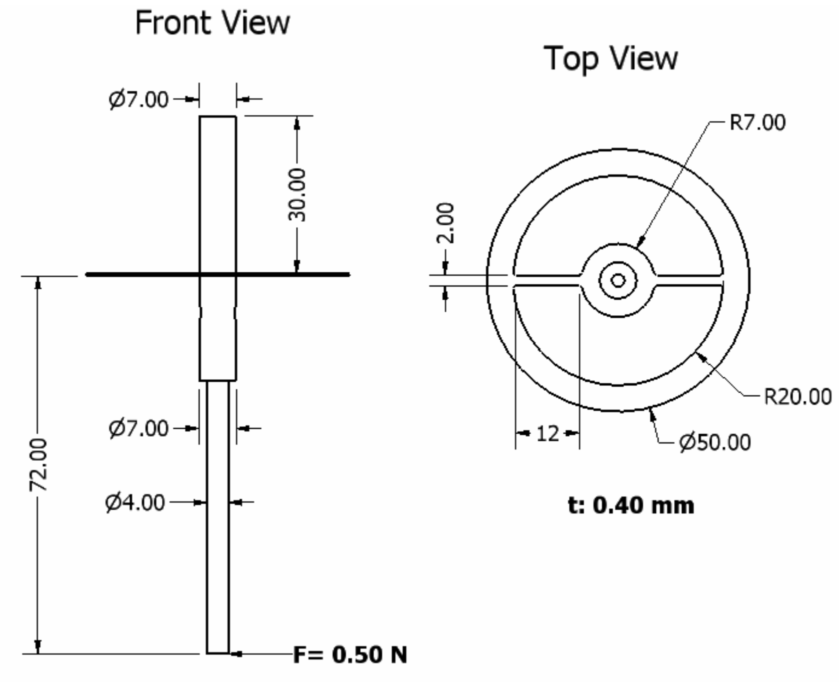

Figure 4.21 Designed model for verification purpose

As can be seen from Figure 4.21, applied force is 0.5 N. The boundary condition adopted for the test is similar to the other tests performed previously. Spring steel plate is fixed around its peripherals. So, the modeled geometry can be thought as a cantilever beam with an end moment.

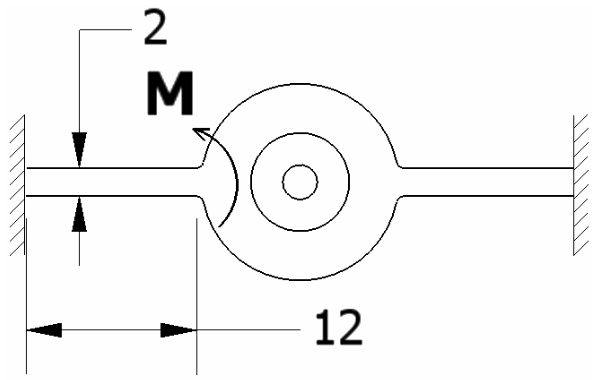

Figure 4.22 Top view of the analyzed model

Through the cantilever beam assumption, simple calculations can be carried out to find the Max stress in the beam.

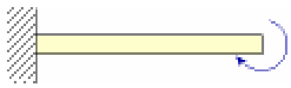

Figure 4.23 Cantilever Beam with an end moment

Max. stress on the beam with this conditions can be calculated as follows;

$$\sigma_{\max} = |M| . \frac{c}{I} \tag{4.1}$$

Where, σ_{max} is the max. stress on the beam, M is the applied moment, c is the distance from neutral axis to extreme fibers and I is moment of inertia.

$$\sigma_{\max} = |0.50[N].72[mm]| . \frac{0.40[mm]/2}{b.t^3/3} \tag{4.2}$$

Where b = 2 mm, t = 0.40 mm respectively. As a result, $\boldsymbol{\sigma_{max}}$ **= 169.22 MPa**. Max. stress result [Von Misses method] of the FEA software is **167.9 MPa**.

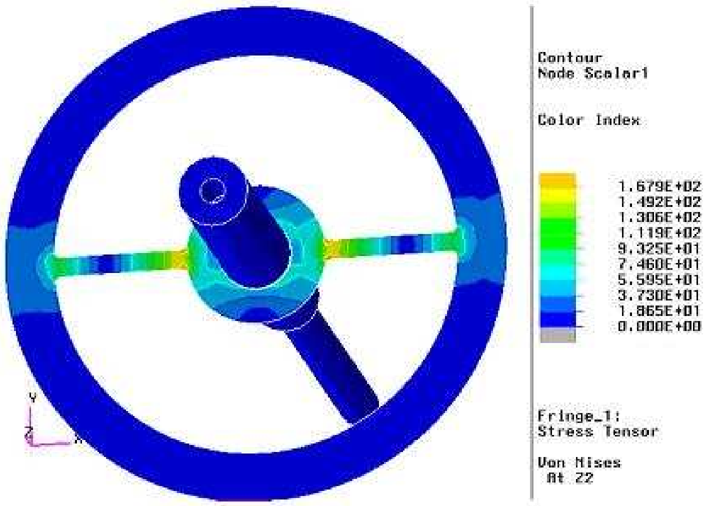

Figure 4.24 Max. Stress result of the FEA software

Consequently, the results coming from two different methods are close to each other. So the correctness of the FEA software is verified by a simple hand calculation method.

4.12 Manufacturing Process

Designed probes are manufactured on conventional machine tools. Furthermore, some other manufacturing techniques are utilized for the spring steel plates and magnet plate. Since, thickness of the spring steel plates are too thin to manufacture, they are manufactured via water jet method. Through this method spring steel plates are manufactured in desired forms without encountering any kind of manufacturing related problems. Afterwards, those spring plates are washed via ultrasonic washing machine in order to dissolve the dirts coming from water jet manufacturing process. However, this method did not dissolve the dirts exactly. In that case, spring steel plates are sanded via sand paper. Furthermore, one of the spring steel plate (having thickness 0.20 mm) is put in to a sandblasting machine to see how it will affect the spring steel. As a result, sandblasting operation leaded up to significant deflection on the spring steel plate. One of the important technique used during the manufacturing process was the laser cutting. Since, spring steel has larger Elastic Modulus (E) and the thickness of the magnet plate is 2 mm, it has seen that they could nor be manufactured via conventional manufacturing techniques. Due to the stiffness of the spring steel material, they are produced via laser cutting. Furthermore, the hole of the magnet plate is enlarged via Electrical Discharge Machine (EDM).

When it comes to the materials used in manufactured probes, aluminium is preferred mostly. The material of the main probe body, top lid and bottom lid is 7075 type aluminium. For the shafts (stylus shaft and magnet plate holder shaft) T-304 and T-303 stainless steels are used. More importantly, holes and the grooves of the main probe body are put on to a diffuser to drill the holes and to form the grooves at desired angles.

4.13 Conclusion

In this chapter, designed touch trigger / measurement probes are proposed and divided into two groups; major designs and alternative designs. Considering the ease of the manufacturing process, major design-1 and major design-2 is selected. Furthermore, finite element analysis are presented in this chapter. Those finite element analyses play an important role because those analysis gave us an opportunity to see the results before the manufacturing process. Furthermore, simple hand calculations are also performed in order to verify the correctness of the finite element analyses results. Among the tested geometries, geometry-5 is picked up and other geometries are derived from this selected original geometry. The geometry selected in here is vital because it will be the reference plane for the probe and it will be the basis of the mechanism. By virtue of the selected geometry, the stylus tip will transfer the deflections to the magnet plate. Furthermore, Von Misses Stress results are examined during the finite element analysis not to encounter any kind of plastic deformation during the real tests of the probe.

CHAPTER 5

ANVIL GAUGE DESIGNS

5.1 Introduction

Anvil gauge apparatus is designed for the test of the designed probe. The main purpose of this device is to deflect the stylus tip of the probe along the desired directions. In addition to the main task of the anvil gauge, it was also used during the GMR sensor tests as can be seen from the figures in Chapter 3 under the headline GMR sensor tests. However, probe tests are carried on a three-axis computer controlled Electrical Discharge Machine (EDM), anvil gauge is used at the tests as a workpiece during the tests that are performed at the equator of the stylus tip. Furthermore, the designed probes are tested at different latitudes below the equator through the angled parts (mounted on the shaft of the anvil gauge) designed for this task; anvil gauge device is also used during those tests as well.

5.2 Major Design

As can be seen from Figure 5.1, major anvil gauge design is formed via simple parts. Through the designed mechanism, by turning the adjusting cylinder clockwise or counter clockwise, magnet cylinder will move upwards or downwards without any rotational movement. Trough the flat area formed on the magnet cylinder lets the shaft to move only up and down without any rotation. Therefore, shaft guide is screwed on to the upper part of the device. Considering the ease of the manufacturing process, hole is drilled on the upper part of the device. By virtue of the compression spring, magnet shaft and the adjusting cylinder will maintain their positions. Through the grooves on the magnet shaft, bar magnets can be located precisely.

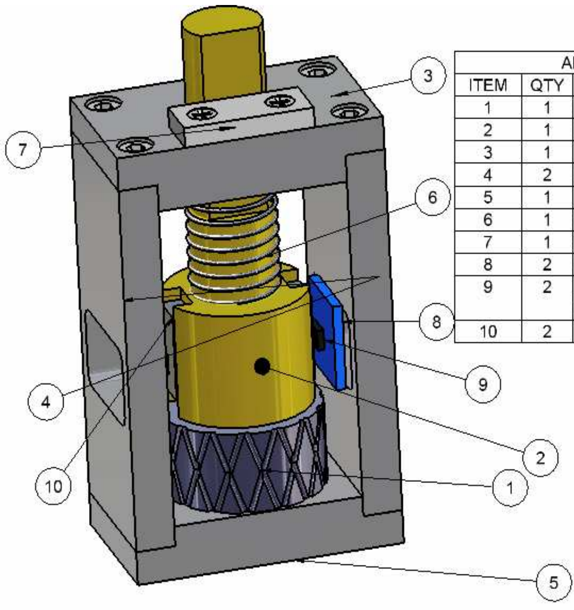

ANVIL GAUGE MAJOR DESIGN			
ITEM	QTY	PART NUMBER	DESCRIPTION
1	1	Adjusting Cylinder	Stainless Steel
2	1	Magnet Cylinder	Stainless Steel
3	1	Device Upper Part	Aluminium 6010
4	2	Device Side Part	Aluminium 6010
5	1	Device Bottom Part	Aluminium 6010
6	1	Compression Spring	Stainless Steel
7	1	Shaft Guide	Aluminium 6010
8	2	GMRSenspr PCB	
9	2	NVE AA006-02E GMR sensor	
10	2	Bar Magnet	

Figure 5.1 Major Anvil Gauge Design

Furthermore, in order to test the probe at different latitudes below the equator of the stylus tip, different parts are manufactured at different angles. Thus, via those manufactured parts the probe will be tested at different latitudes; 22.5 º, 45 º and 67.5 º below the equator. Those parts are mounted on the top region of the magnet shaft and they are fixed via a setscrew.

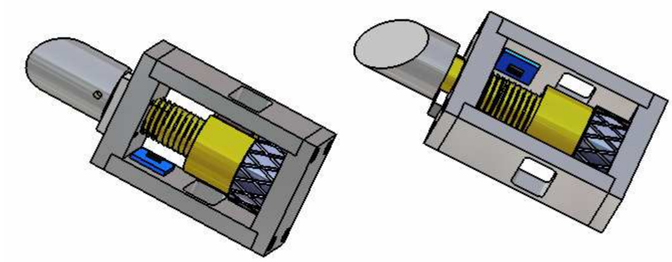

Figure 5.2 Anvil gauge design with an angled part

Figure 5.3 Anvil Gauge Device

5.3 Alternative Design

Another model is designed for the anvil gauge apparatus. This design differs from the major design in many ways dramatically. At first, this design is extremely huge when it is compared with the major design. Through the screw at the middle, part containing too many holes is moved on a guide along the axis of the screw. It is assumed that, those holes will scatter the magnetic field lines in a different fashion and through this way; GMR sensor will sense the displacement amount of the part. Thus, displacement amount of the shaft that is located on to this part can be known. However, the difficulty of the manufacturing process and the size of this design made the design as an alternative design.

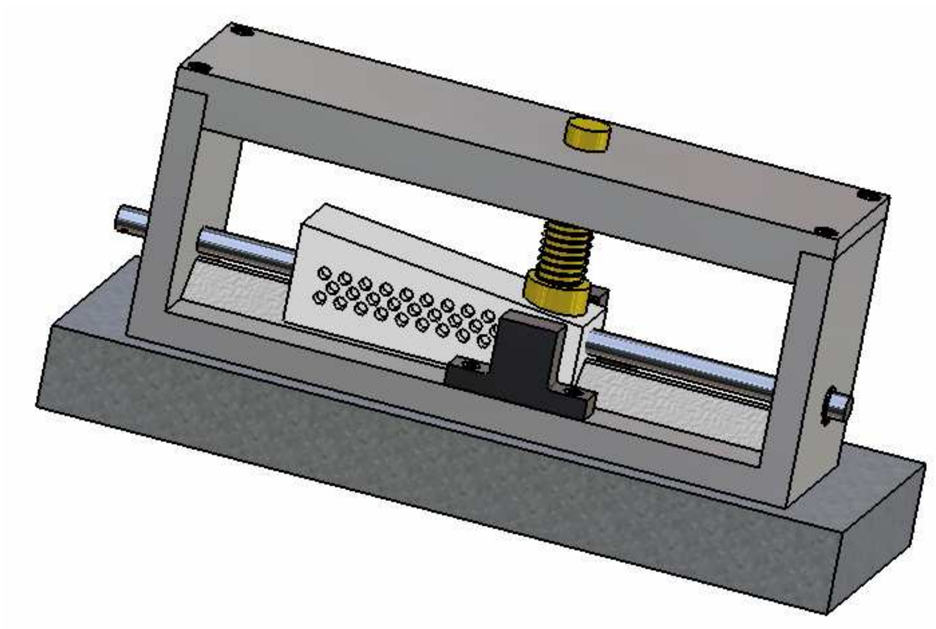

Figure 5.4 Alternative anvil gauge design

5.4 Calibration Results of the Major Anvil Gauge Design

Calibration process is carried out via a comparator, each 0.25 mm displacement amount of the magnet shaft is verified via a comparator, and the corresponding voltage values are read from the NVE AA006-02 GMR sensor respectively. In the total 10 tests are performed via the anvil gauge apparatus; 5 upward movement of the magnet shaft (0 mm to 5.5 mm) and 5 downward movement of the magnet shaft (5.5 mm to 0 mm.). During the calibration tests, data acquired from GMR sensor tests (Chapter 3, Figure 3.7) is used as a guide and bar magnet and the GMR sensor is located in accordance with those obtained results in order to stay in the operation zone. For that reason the data acquired from the calibration test of the anvil gauge and the data coming from the GMR sensor tests with bar magnet are plotted in the same figure just to verify that the bar magnet and the GMR sensor are located correctly.

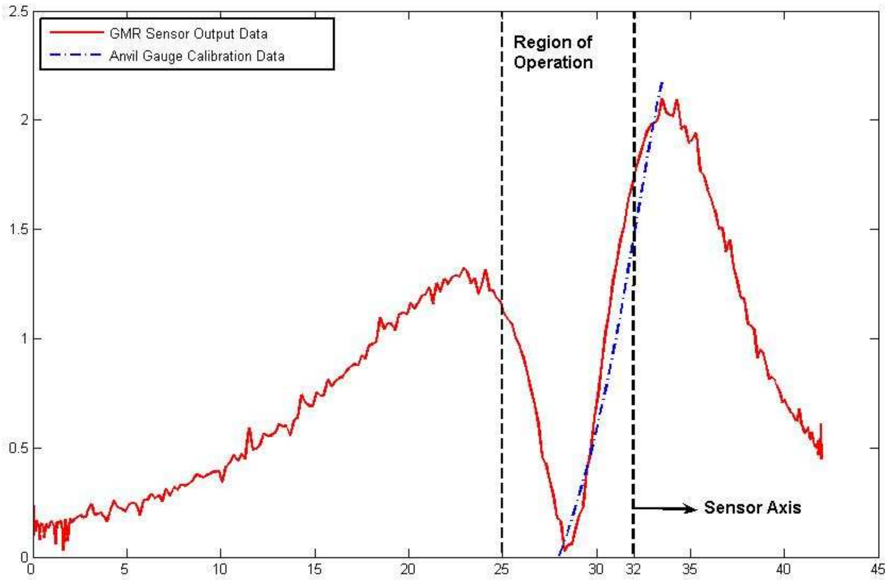

Figure 5.5 Calibration data and GMR sensor-bar magnet data plot

In accordance with the obtained data, as can be seen from Figure 5.5, results of the calibration test stay in the linear zone. Furthermore, acquired data points are fitted to a curve via least squares method using regression model that is;

$$V(x) = p_0 + p_1.x_i + p_2.x_i^{\ 2} + \ldots + p_n.x_i^{\ n} \tag{5.1}$$

Where p_i values are the constants of the polynomial fitted curve, V(x) is the voltages values, n is the degree of the polynomial and x_i values are the displacement amounts respectively. Through this method, fitted curve is plotted in Figure 5.6 and 5.7. Since there are 23 data points, the best-fit curve is determined not to encounter any kind of higher uncertainty amounts or over fitting cases. As a result best fit curve is obtained when the degree of the polynomial is 5 (n=5).

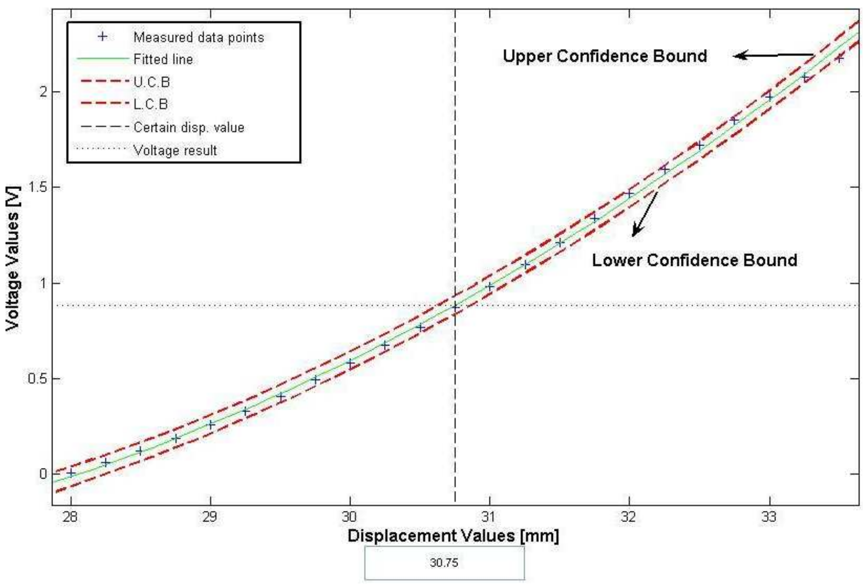

Figure 5.6 Fitted Curve (n= 2)

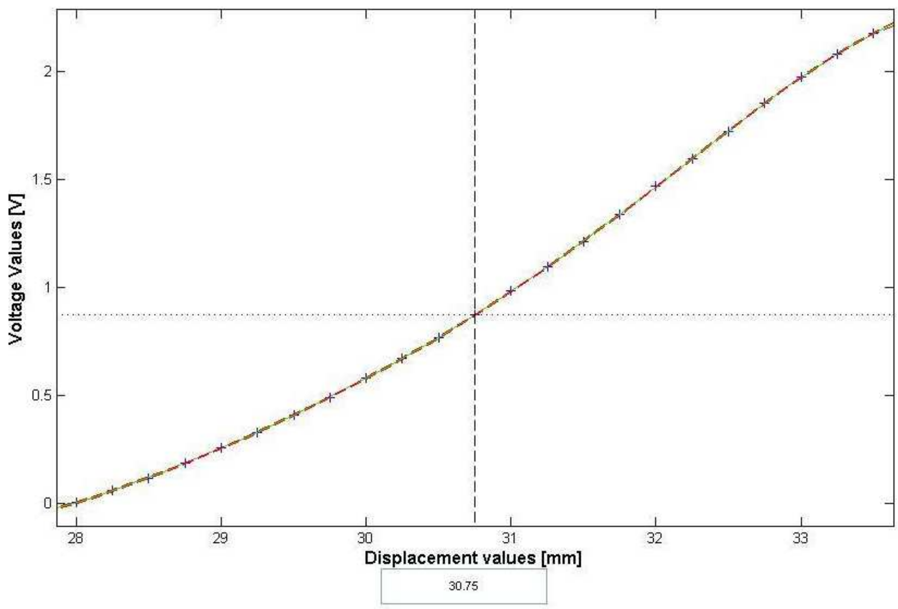

Figure 5.7 Best Fitted Curve (n= 5)

5.5 Manufacturing Process

The anvil gauge apparatus is designed in order to test the probe during the experiments. Since, it will be used during the experiments, the form tolerances of the parts carries vital roles. Furthermore, the system itself comprises too many parts, in order to avoid the failure of the manner of working of the system; all parts have to be manufactured precisely. Therefore, at the beginning of the manufacturing process side, top and bottom walls, and guide part are grinded. In order to manufacture the parts precisely, low feed rates and small cutting depth values are given to the machine tool. The flatness of the side and bottom walls is important. The main reason of the desired flatness of the afore-mentioned surfaces will be a key parameter during the test of the probe. Furthermore, the hole on the top wall and the diameter of the magnet shaft are important parameters for the whole system. They have to be manufactured in a proper fashion in order to lead the magnet shaft's motion inside the hole conveniently. Therefore, the flatness of the surface of the guide part where it leads the magnet shaft to a linear motion is vital indeed. As a result, the components building the anvil gauge apparatus is manufactured in order to avoid the improper functioning of the device. Since, the parts are working all together, they are greased via engine oil. The materials used for this device are 6010 type aluminium and T-303 stainless steel. Side, top, and bottom wall and guide part material is 6010 type aluminium. The material of the magnet shaft, adjusting shaft and angled parts is T-303 stainless steel.

5.6 Conclusion

In this chapter, major and alternative anvil gauge designs are presented. First introduced design was manufactured because of the compact design and ease of the manufacturing process. Furthermore, this design was calibrated via NVE AA006-02 GMR sensor through an instrumentation amplifier circuit. By moving the magnet shaft 0.25 mm, (displacement amount is checked via comparator) each time via rotating the adjusting cylinder, generated outputs are read from the GMR sensor. In accordance with the obtained data, hysteresis band is obtained in all five performed tests. As can be seen from the figures obtained from the calibration tests, generated outputs are laying in the operation zone as defined in Chapter 3, Figure 3.7.

CHAPTER 6

KINEMATIC MODEL

6.1 Kinematical Model of the Probe

When the relevant probe elements including housing, magnet-support plate, and shafts are assumed to behave like rigid objects, a kinematic model of the system can be developed using Homogeneous Transformation Matrices (HTMs). Figure 6.1 illustrates the simplified schematic of the designed probe along with its critical geometric parameters.

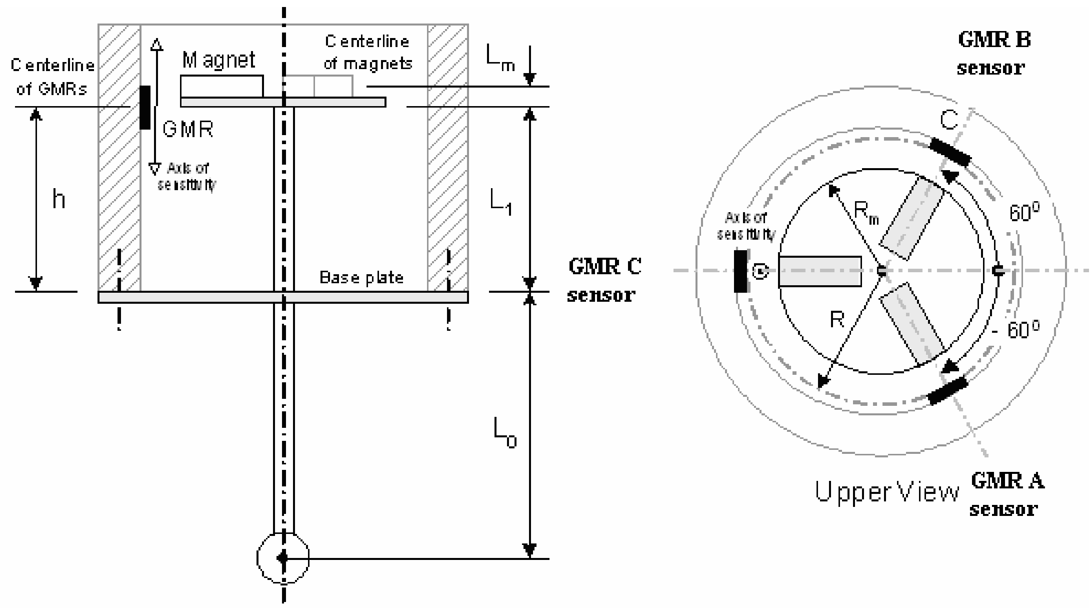

Figure 6.1 Simplified schematic of the measurement probe

When the center of the stylus ball is displaced by Δx, Δy, and Δz along the fundamental axes; Figure 6.2 shows both the resulting position and the reference coordinate frames to be used in the analysis. Note that since the stylus displacement is to be small (e.g. less than a few millimeters); the motion shown in the figure is deliberately exaggerated to make distinction among various reference frames as well as their corresponding parameters. As can be seen, three coordinate frames are defined to simplify the ongoing analysis. For instance, the fixed frame $\{X_0, Y_0, Z_0\}$, which appears to be on the base plate, is essentially connected to the body of the probe and is used as a global reference. Likewise, the frame $\{X_1, Y_1, Z_1\}$ is the attached to the probe shaft. When the probe is in its neutral position, its origin (O') coincides with that of the global coordinate frame (O). Finally, the extra coordinate frame $\{X_2, Y_2, Z_2\}$, which is solely defined for the sake of simplicity, is a translated reference frame along the probe shaft and could be appended to the previous frame if desired.

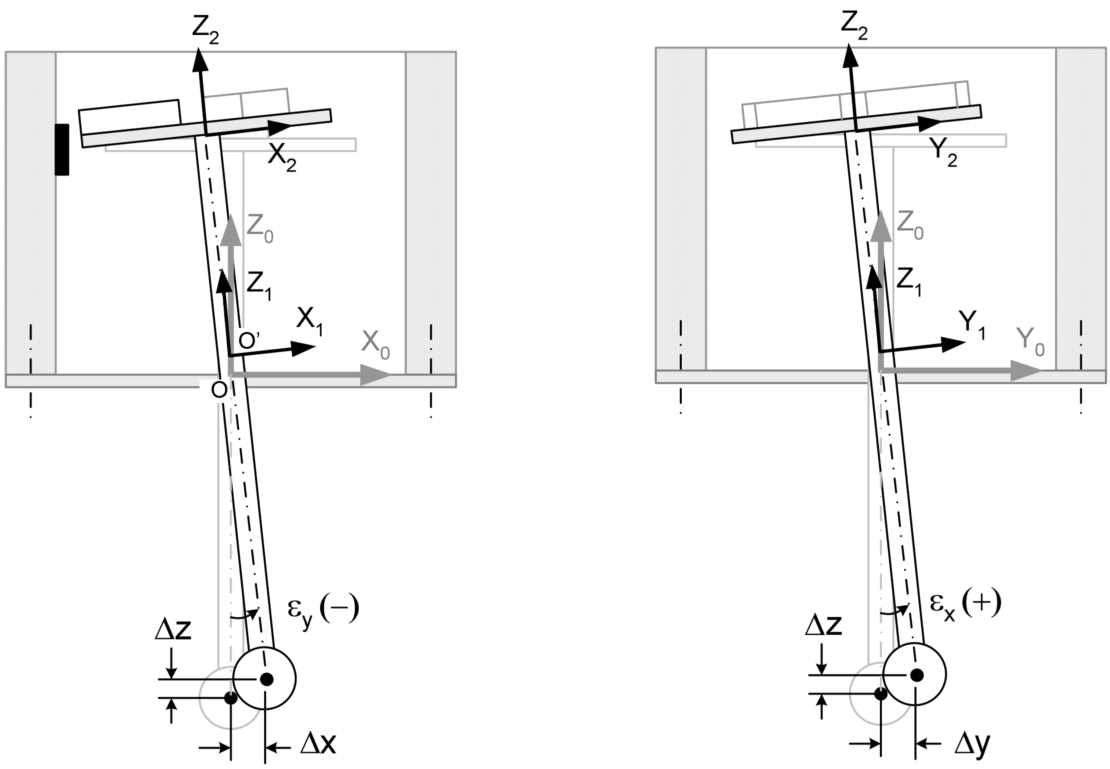

Figure 6.2 Reference frames for kinematic analysis

Armed with this information, one can express the transformations (i.e. HTMs) among these reference frames. To be specific, the location of a point in the Cartesian coordinate frame {j} (namely, ${}^{j}P$) can be conveniently converted to its corresponding position (vector) in {i} (${}^{i}P$). Under the assumption that all relative motions are very small in magnitude; the HTM implementing this coordinate transformation could be given as;

$$
{}^{i}_{j}T = \begin{bmatrix} 1 & -\varepsilon_z & \varepsilon_y & \delta_x \\ \varepsilon_z & 1 & -\varepsilon_x & \delta_y \\ -\varepsilon_y & \varepsilon_x & 1 & \delta_z \\ 0 & 0 & 0 & 1 \end{bmatrix} \tag{6.1}
$$

Thus,

$$
{}^{i}P = {}^{i}_{j}T \cdot {}^{j}P \tag{6.2}
$$

Note that in (1), ε_x, ε_y, and ε_z are small angles representing the orientation of {j} wrt. {i} while δ_x, δ_y, and δ_z denote minute displacements about the corresponding origins. For detailed derivations, reader is encouraged to refer [Slocum]. Consequently, the HTM relating {0} to {1} takes the following form:

$$
{}^{0}_{1}T = \begin{bmatrix} 1 & 0 & \varepsilon_y & 0 \\ 0 & 1 & -\varepsilon_x & 0 \\ -\varepsilon_y & \varepsilon_x & 1 & \Delta z \\ 0 & 0 & 0 & 1 \end{bmatrix} \tag{6.3}
$$

where the (small) angular motions demonstrated in Figure 6.2 can be expressed as

$$
\varepsilon_x = \frac{\Delta y}{L_0}; \quad \varepsilon_y = -\frac{\Delta x}{L_0} \tag{6.4}
$$

It is critical to notice that by design; the helical beams in the probe's base plate allow the stylus to rotate about the origin (O) without any considerable translation of O’ in the XY plane. Similarly, when the stylus is in contact with the part, the roll motion of the probe shaft is also insignificant if compared to its counterparts: $\varepsilon_Z \cong 0$. Eventually, the HTM relating the coordinate frame {1} to {2} is

$$ {}^{1}_{2}T = \begin{bmatrix} 1 & 0 & 0 & 0 \\ 0 & 1 & 0 & 0 \\ 0 & 0 & 1 & L_1 \\ 0 & 0 & 0 & 1 \end{bmatrix} \tag{6.5} $$

Hence, the centerline coordinates of the magnets that face various GMR sensors can be calculated wrt. global coordinate system {0}:

$$ {}^{0}P_{*}^{M}(\Delta x, \Delta y, \Delta z) = {}^{0}_{1}T(\Delta x, \Delta y, \Delta z) \cdot {}^{1}_{2}T \cdot {}^{2}P_{*}^{M} \tag{6.6} $$

Here, * is a wildcard for letters A, B, and C indicating the location of a particular magnet on the circular support plate. Position vectors in frame {2} can be directly written:

$$ {}^{2}P_{A}^{M} = \begin{bmatrix} -R_m \\ 0 \\ L_m \\ 1 \end{bmatrix} \tag{6.7a} $$

$$ {}^{2}P_{B}^{M} = \begin{bmatrix} R_m \cos(-60^0) \\ R_m \sin(-60^0) \\ L_m \\ 1 \end{bmatrix} = \begin{bmatrix} \frac{1}{2} R_m \\ -\frac{\sqrt{3}}{2} R_m \\ L_m \\ 1 \end{bmatrix} \tag{6.7b} $$

$$ {}^{2}P_{C}^{M} = \begin{bmatrix} R_m \cos(60^0) \\ R_m \sin(60^0) \\ L_m \\ 1 \end{bmatrix} = \begin{bmatrix} \frac{1}{2} R_m \\ \frac{\sqrt{3}}{2} R_m \\ L_m \\ 1 \end{bmatrix} \tag{6.7c} $$

Substituting (6.3), (6.4), (6.5), and (6.7) into (6.6) yields

$$ {}^{0}P_{A}^{M} = \begin{bmatrix} -R_m - c\Delta x \\ -c\Delta y \\ cL_0 - \frac{R_m}{L_0}\Delta x + \Delta z \\ 1 \end{bmatrix} \tag{6.8a} $$

$$ {}^{0}P_{B}^{M} = \begin{bmatrix} \frac{R_m}{2} - c\Delta x \\ -\frac{\sqrt{3}R_m}{2} - c\Delta y \\ cL_0 + \frac{R_m}{2L_0}\Delta x - \frac{\sqrt{3}R_m}{2L_0}\Delta y + \Delta z \\ 1 \end{bmatrix} \tag{6.8b} $$

$$ {}^{0}P_{C}^{M} = \begin{bmatrix} \frac{R_m}{2} - c\Delta x \\ \frac{\sqrt{3}R_m}{2} - c\Delta y \\ cL_0 + \frac{R_m}{2L_0}\Delta x + \frac{\sqrt{3}R_m}{2L_0}\Delta y + \Delta z \\ 1 \end{bmatrix} \tag{6.8c} $$

where $c \equiv (L_m+L_1)/L_0$. Recall that the first three components of (6.8) essentially yield the Cartesian coordinates of each magnet's center at the rim wrt. the global frame. Likewise, the global coordinates of the centerline for the GMR sensors could be directly obtained:

$$ {}^{0}P_{A}^{S} = \begin{bmatrix} -R \\ 0 \\ h \\ 1 \end{bmatrix} \tag{6.9a} $$

$$ {}^{0}P_{B}^{S} = \begin{bmatrix} R\cos(-60^0) \\ R\sin(-60^0) \\ h \\ 1 \end{bmatrix} = \begin{bmatrix} \frac{1}{2}R \\ -\frac{\sqrt{3}}{2}R \\ h \\ 1 \end{bmatrix} \tag{6.9b} $$

$$
{}^{0}P_{C}^{S} = \begin{bmatrix} R\cos(60^{0}) \\ R\sin(60^{0}) \\ h \\ 1 \end{bmatrix} = \begin{bmatrix} \frac{1}{2}R \\ \frac{\sqrt{3}}{2}R \\ h \\ 1 \end{bmatrix} \tag{6.9c}
$$

The following (vector) difference equation gives the relative motion of the magnetic field vector (as generated by the permanent magnets) with respect to the center point along the sensitivity axis of the GMR sensor:

$$
{}^{0}E_{*} = {}^{0}P_{*}^{S} - {}^{0}P_{*}^{M} \tag{6.10}
$$

Three fundamental components of (6.10) could be expressed as;

$$
E_{A} = \begin{bmatrix} \delta x_{A} \\ \delta y_{A} \\ \delta z_{A} \end{bmatrix} = \begin{bmatrix} -\Delta R + c\Delta x \\ c\Delta y \\ h - cL_{0} + \frac{R_{m}}{L_{0}}\Delta x - \Delta z \end{bmatrix} \tag{6.11a}
$$

$$
E_{B} = \begin{bmatrix} \delta x_{B} \\ \delta y_{B} \\ \delta z_{B} \end{bmatrix} = \begin{bmatrix} \frac{\Delta R}{2} + c\Delta x \\ -\frac{\sqrt{3}\Delta R}{2} + c\Delta y \\ h - cL_{0} - \frac{R_{m}}{2L_{0}}\Delta x + \frac{\sqrt{3}R_{m}}{2L_{0}}\Delta y - \Delta z \end{bmatrix} \tag{6.11b}
$$

$$
E_{C} = \begin{bmatrix} \delta x_{C} \\ \delta y_{C} \\ \delta z_{C} \end{bmatrix} = \begin{bmatrix} \frac{\Delta R}{2} + c\Delta x \\ \frac{\sqrt{3}\Delta R}{2} + c\Delta y \\ h - cL_{0} - \frac{R_{m}}{2L_{0}}\Delta x - \frac{\sqrt{3}R_{m}}{2L_{0}}\Delta y - \Delta z \end{bmatrix} \tag{6.11c}
$$

where $\Delta R \equiv R - R_m$. Note that the GMR sensor is insensitive to the motion of magnetic field along the tangential direction. Only the relative displacements of the permanent magnet wrt the center of the GMR sensor in the radial (i.e. normal to the surface of GMR) and axial (i.e. along the axis of sensitivity) directions are needed for all intensive purposes. Hence, taking the projection of (6.11) along the aforementioned (i.e. A, B, C) axes yields these components:

$$\begin{bmatrix} r_A \\ r_B \\ r_C \end{bmatrix} = c \cdot \begin{bmatrix} -1 & 0 \\ \frac{1}{2} & -\frac{\sqrt{3}}{2} \\ \frac{1}{2} & \frac{\sqrt{3}}{2} \end{bmatrix} \begin{bmatrix} \Delta x \\ \Delta y \end{bmatrix} + \begin{bmatrix} r_0 \\ r_0 \\ r_0 \end{bmatrix} \tag{6.12a}$$

$$\begin{bmatrix} a_A \\ a_B \\ a_C \end{bmatrix} = \begin{bmatrix} \frac{R_m}{L_0} & 0 & -1 \\ -\frac{R_m}{2L_0} & \frac{\sqrt{3}R_m}{2L_0} & -1 \\ -\frac{R_m}{2L_0} & -\frac{\sqrt{3}R_m}{2L_0} & -1 \end{bmatrix} \begin{bmatrix} \Delta x \\ \Delta y \\ \Delta z \end{bmatrix} + \begin{bmatrix} a_0 \\ a_0 \\ a_0 \end{bmatrix} \tag{6.12b}$$

where r_A, r_B, r_C (≥ 0, by definition) denote the radial displacements while a_A, a_B, and a_C represent the axial displacements along direction A, B, and C respectively. Figure 6.3 shows the axial and radial distance convention used in this study. The next section concentrates on the calculation of stylus displacements employing GMR readings.

6.2 Calculation of Stylus Displacements

In the previous section, a kinematic model of the probe has been developed for the purpose of relating the motion of the stylus to the relative displacements of permanent magnets wrt the GMR sensors.

In fact, GMR sensor along with its interface (amplifier + filter) circuitry used in this study generates a linear unipolar voltage (ranging from 0 to 5 Volts) as a function of the magnetic field's displacement (or change in its intensity) along its principal axis (i.e. axis of sensitivity). Figure 6.4 illustrates the characteristic output of this system. Hence, the quasi-static behavior of the sensor in the linear region could be represented by;

$$v = k_1 a - k_2 ar \qquad (a, r > 0) \tag{6.13}$$

where a and r are the axial- and radial displacements of the sensor with respect to mmf (magneto-motive-force) source (i.e. permanent magnet) while k_1 [V/m] and k_2 [V/m^2] are two known constants of this system. As can be seen from Figure 6.4; the generated voltage, v, can be regarded as the absolute value of the displacement and thus determining the direction of motion is a major challenge when operating the sensor about its center point. Hence, it must be biased by moving the mmf source above or below the sensor's centerline to determine the direction.

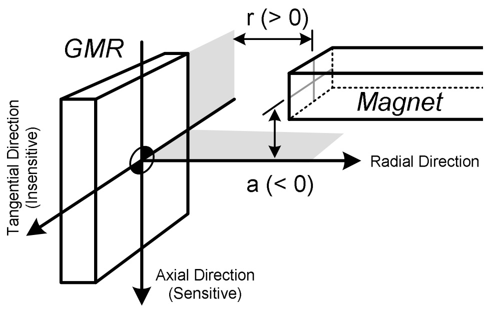

Figure 6.3 Axis convention

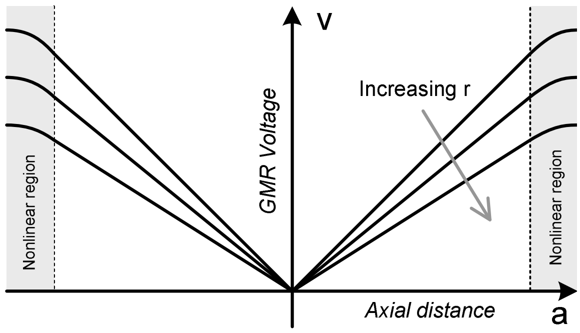

Figure 6.4 Quasi-static behavior of GMR sensor

When the stylus is free (e.g. not in contact with the part), let the generated voltage be;

$$v_0 = k_1 a_0 - k_2 a_0 r_0 \tag{6.14}$$

where a_0 and r_0 are the initial axial- and radial proximity at this neutral point. The geometric parameters defined in the previous section dictate that $a_0 = h – L_1 – L_m$ and $r_0 = R – R_m$. Note that this choice implies that the operating region of the sensor is restricted to $0 \le a \le 2a_0$. Likewise, subtracting (6.14) from (6.13) yields the incremental sensor voltage:

$$\Delta v = v - v_0 = k_1(a - a_0) - k_2(ar - a_0 r_0) \tag{6.15}$$

Unfortunately, since this voltage, which depends on two arguments (a and r), is nonlinear (or **"bilinear"** to be exact) by nature, an iterative procedure must be adapted to solve Δx, Δy, and Δz. That is, with an estimate $(\hat{r}_*)$ at hand; the axial displacement at a specific location can be determined:

$$a_* = \frac{\Delta v_* + (k_1 - k_2 r_0)a_0}{k_1 - k_2 \hat{r}_*} \tag{6.16}$$

where $\hat{r}_* = r_0 = R - R_m$ is usually a good initial choice. Solving (6.12b) leads to the displacements of the stylus end-point:

$$\begin{bmatrix} \Delta x \\ \Delta y \\ \Delta z \end{bmatrix} = \begin{bmatrix} \frac{2L_0}{3R_m} & -\frac{L_0}{3R_m} & -\frac{L_0}{3R_m} \\ 0 & \frac{L_0}{\sqrt{3}R_m} & -\frac{L_0}{\sqrt{3}R_m} \\ -\frac{1}{3} & -\frac{1}{3} & -\frac{1}{3} \end{bmatrix} \begin{bmatrix} \frac{\Delta v_C + k_2(\hat{r}_A - r_0)a_0}{k_1 - k_2 \hat{r}_A} \\ \frac{\Delta v_A + k_2(\hat{r}_B - r_0)a_0}{k_1 - k_2 \hat{r}_B} \\ \frac{\Delta v_B + k_2(\hat{r}_C - r_0)a_0}{k_1 - k_2 \hat{r}_C} \end{bmatrix} \tag{6.17}$$

Notice that when $\hat{r}_A \cong \hat{r}_B \cong \hat{r}_C \cong r_0$ this equations boils down to;

$$\begin{bmatrix} \Delta x \\ \Delta y \\ \Delta z \end{bmatrix} = \begin{bmatrix} a_{11} & a_{12} & a_{13} \\ a_{21} & a_{22} & a_{23} \\ a_{31} & a_{32} & a_{33} \end{bmatrix} \begin{bmatrix} \Delta v_A \\ \Delta v_B \\ \Delta v_C \end{bmatrix} \tag{6.18}$$

Consequently, (12a) is employed to get a better estimate on the radial displacements. Since, Equation 6.17 is directly dependent to the geometrical parameters of the probe, another model is developed via Least Squares Method (LSM) in order to acquire more better estimate of the measured data. This procedure could be repeated several times until (6.17) converges to an acceptable solution. To study the convergence (and stability) of the proposed method, a Monte-Carlo simulation (with 20000 instances) has been conducted with the following random variables:

- Δx and Δy: uniform probability density between -1 and 1 mm;
- Δz: uniform probability density between 0 and 1 mm;
- k_2/k_1: uniform probability density between 0 and 20%.

It is critical to note that k_2/k_1 ratio here serves as a measure for the dominance of radial proximity on the dynamic behavior of the sensor. In the simulation, the nominal values of the actual-system parameters are employed. As a metric for the estimation error, a vector norm is defined:

$$e = \left\| \begin{matrix} \Delta x - \Delta \hat{x} \\ \Delta y - \Delta \hat{y} \\ \Delta z - \Delta \hat{z} \end{matrix} \right\| \tag{6.19}$$

An error threshold of 1 μm is utilized to terminate the iterations while the maximum allowable iteration number in the simulation is limited to 100. It has been observed that the algorithm is stable and quickly converges to the true values in usually one or two iteration steps. The source code (CCS C) of the probe's firmware, which essentially implements this algorithm on an 8-bit microcontroller (PIC16F88@20 Mhz), is given in the Appendix A.1.

6.3 Conclusion

In this chapter, a kinematic model of the probe is developed using HTMs. In accordance with that, reference frames for kinematic analysis is defined. So by virtue of this information, the transformations (i.e. HTMs) among these reference frames can be expressed. In brief, a kinematic model of the probe has been developed in order to relate the motion of the stylus to the relative displacements of permanent magnets wrt the GMR sensors. Furthermore, in order to determine the displacement of the stylus tip, a model (6.17) is developed. Since this equation is dependent to the various parameters such as L_0, R_m, and they cannot be known exactly, the constants of the model are to be determined via Least Squares Method (LSM) for a better estimate.

CHAPTER 7

PROBE INTERFACING

7.1 GMR Signal Processor

As indicated in Chapter 3, the GMR sensors are essentially used in Wheatstone bridge configuration where the GMR changes its resistance dramatically when subjected to even small magnetic fields along its principal (axial) axis. Thus, the output of the sensor is a small differential voltage, which must be conditioned (i.e. buffered, amplified, and filtered), for all practical purposes. In this study, a three-channel GMR processor has been designed as shown in Figure 7.1 a schematic of the card has been given in Figures 7.2, 7.3, 7.4 and 7.5. As can be seen, the card has two main stages: i) Signal conditioner and ii) the processor. At the first stage; a bunch of general purpose op-amps (TL084) are used to condition the differential voltages generated by the sensors. Three instrumentation amplifiers, whose gains are adjusted by the multi-turn pots RV2, RV4, and RV6 (50kΩ), are used to amplify the signal. The corresponding gain (K) can be calculated as

$$K = 1 + \frac{20000}{R_V} \tag{7.1}$$

where R_v refers to the resistance of the aforementioned pots at a particular instant. Theoretically, this gain could be adjusted in between 1.8 and ∞. After this stage, the differential amplifier is utilized to bias the amplified GMR voltages while referencing them to the ground potential. Notice that all the resistors (20kΩ) of this amplifier must be matched manually to reject common mode voltage since the calculation of stylus displacements are very sensitive to noise as well drift introduced along the way. Likewise, the offset voltage of this circuit could be adjusted from -12V (V_{SS}) to 12V (V_{CC}) using the multi-turn pots RV1, RV3, and RV5 (50kΩ). Thus, not only the amplitude of the signal but also its offset could be set precisely so that the processed voltage lies within the prescribed range (unipolar 5V) for the A/D converter of the proceeding stages.

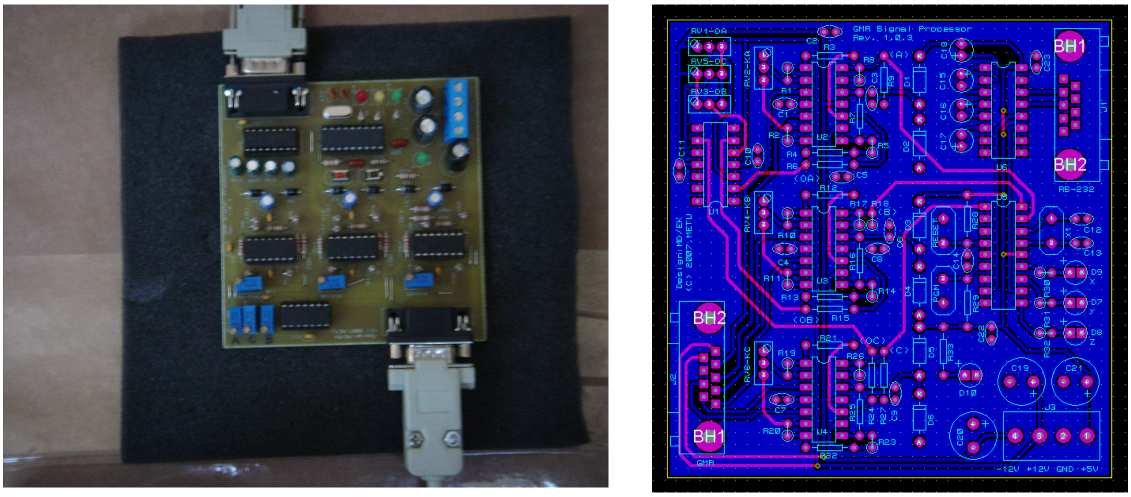

Figure 7.1 GMR signal processor board

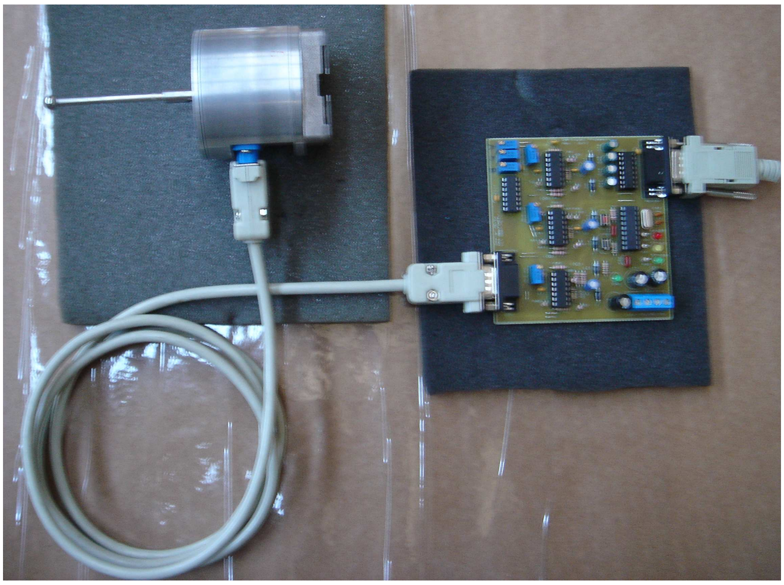

Figure 7.2 GMR signal processor board and the probe

Then, the voltage is passed through a low-pass filter whose cut-off (f_c) frequency is calculated by

$$f_c = \frac{1}{2\pi R_f C_f} \tag{7.2}$$

where R_f and C_f corresponds to the elements of the passive RC circuit (for instance, see R7 and C3 of Figure 7.2). Usually, a bandwidth frequency of a few Hertz is more than adequate for all practical purposes. Note that to protect the A/D converter; the Schottky diodes of the circuit clamp the output voltage to 5V and 0V whenever the processed voltage exceeds these levels.

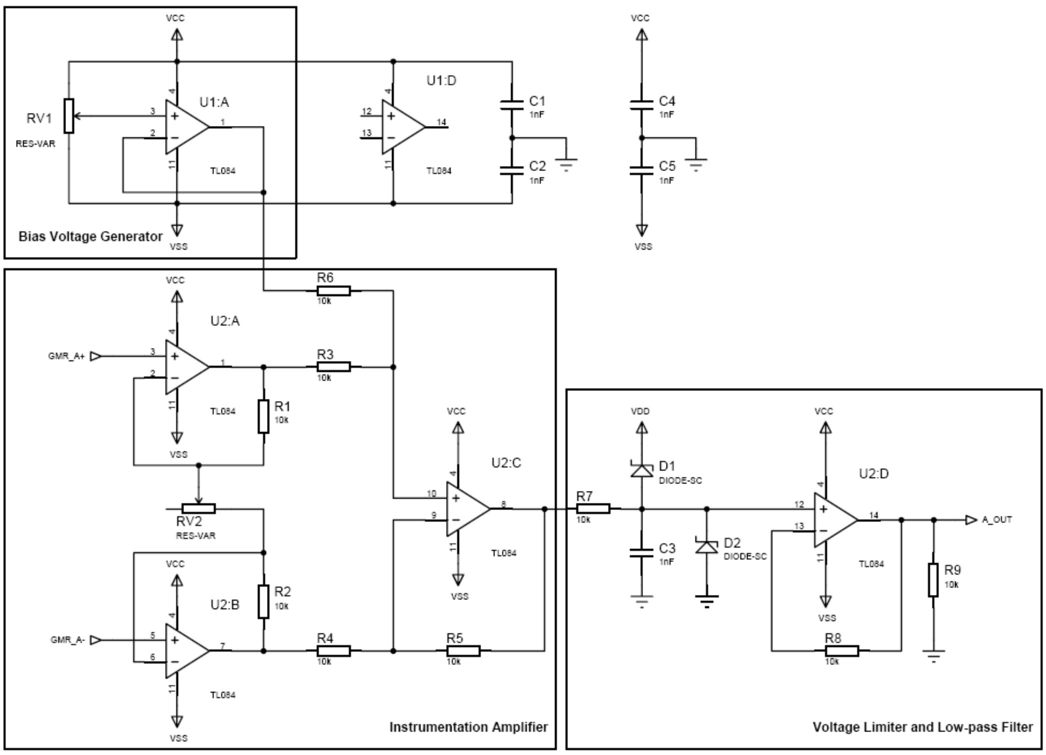

Figure 7.3 Signal conditioner for GMR A

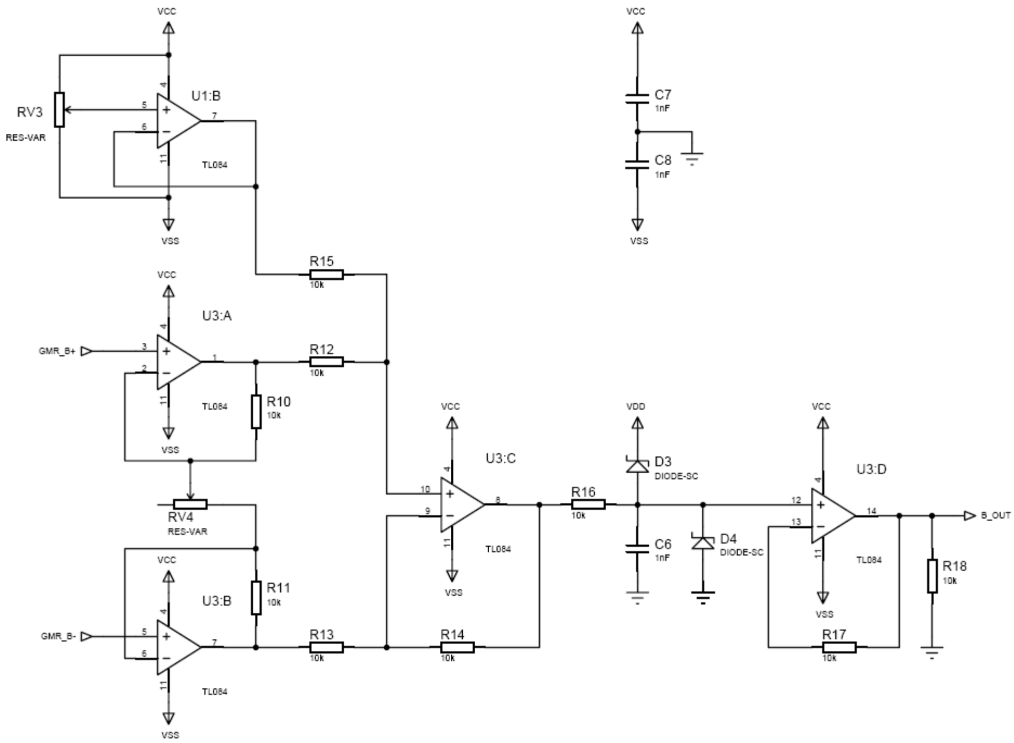

Figure 7.4 Signal conditioner for GMR B

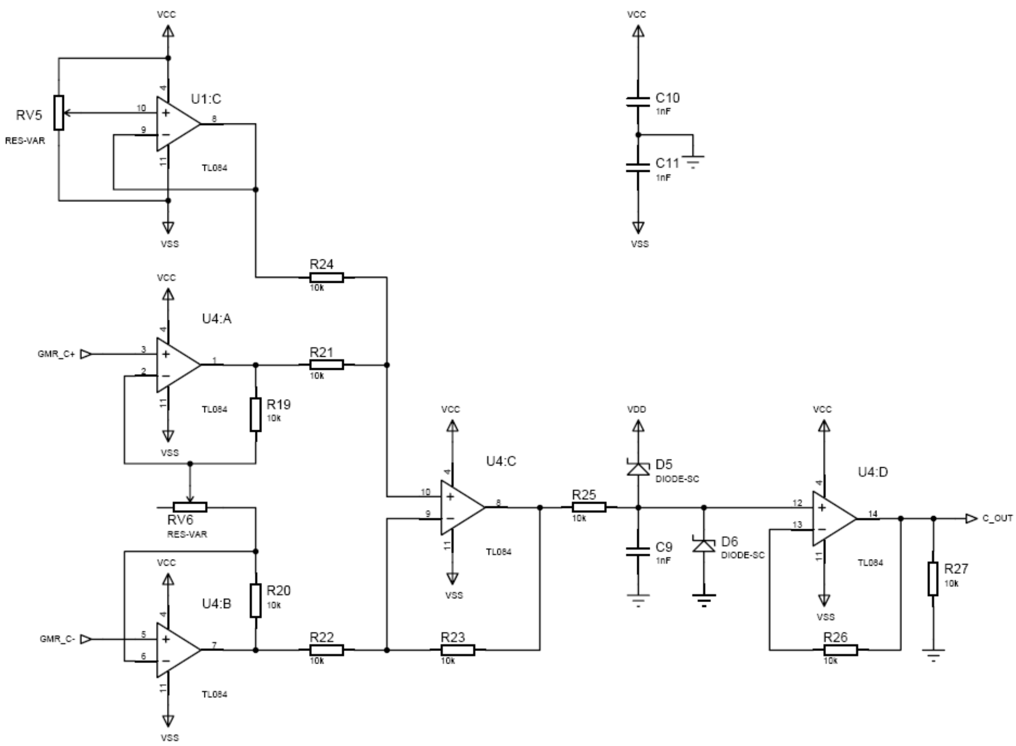

Figure 7.5 Signal conditioner for GMR C

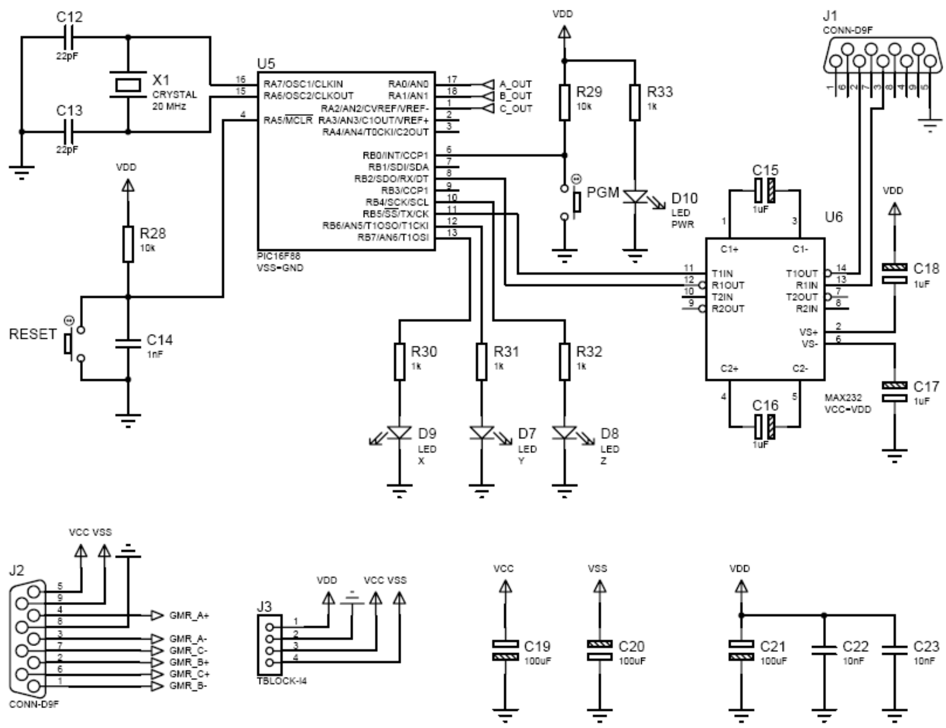

Figure 7.6 Signal processor

Finally, as can be seen in Figure 7.6; a PIC18F88 (8-bit RISC) microcontroller running at 20MHz is utilized to calculate the stylus displacements by taking into account these processed GMR voltages. For this purpose, all three signals are connected to the low three pins of Port A (a.k.a. analog port) that incorporates a (multiplexed) 10-bit A/D converter. Similarly, three LEDs driven by this microcontroller indicate a probe triggering event for each principal axis. Note that, a MAX 232 (voltage level) converter is also included in this circuitry so as to provide a communication means with a host PC via RS-232 serial port. Hence, the calculated displacements might be transferred to the controller of the CMM in real time right after a triggering event occurs. Note that the firmware of the microcontroller, which is developed by CCS C), plays a key role in the function of this card. The C source code of the probe firmware is given in Table A.1 in Appendix A.1

7.2 Conclusion

In this chapter, a three-channel GMR processor has been designed which has two main stages; signal conditioner and the processor. At the first stage, a bunch of general-purpose op-amps (TL084) are used to condition the differential voltages generated by the sensors. Three instrumentation amplifiers, whose gains are adjusted by the multi-turn pots RV2, RV4, and RV6 (50kΩ), are used to amplify the signal. As a second stage, the differential amplifier is utilized to bias the amplified GMR voltages while referencing them to the ground potential. Finally, a PIC18F88 (8-bit RISC) microcontroller running at 20MHz is utilized to calculate the stylus displacements by taking into account these processed GMR voltages.

CHAPTER 8

EXPERIMENTS and RESULTS

8.1 Introduction

Probe tests are performed on a 3-axis CNC electrical discharge machine (EDM) at Makim Machinery Industry Ltd. Co (Ankara). The probe is mounted on the EDM via the two adapters, which are located on to the top lid of the probe. After fixing the probe to the EDM's body through the adapters, it is observed that the overall length of the probe was not long enough to contact with the table of the EDM. Therefore, an elevator mechanism has to be considered.

At first, as an elevator mechanism a granite table and 4 rectangular shaped marble blocks are preferred. Granite is selected for the table due to its great surface flatness in all directions. Granite table is put on to the marbles and surface flatness is checked via a comparator. During this procedure, comparator is fixed on to the EDM body, and the whole system is driven along the X and Y axes of the granite table. However, during those tests, it has seen that very huge amount of deviations are encountered in both X and Y axes (approximately 2 mm. deviations). In order to eliminate this problem, the marbles are sanded via a sand paper, but unfortunately, it is observed that it was a time consuming process. Thus, elevator mechanism with the marbles did not serve as it was thought at the beginning. The elevator mechanism with the marbles can be seen in Figure 8.1.

Figure 8.1 Granite table and the marbles used for the elevator mechanism

Later on, granite table is put on to a metal (steel) block that has fine form tolerances on its surfaces. After the tests performed via a comparator in order to determine the surface deviations, it is observed that the maximum deviation is 10 µm. in both X and Y-axes. As a result, the granite table with the metal block is used during the probe tests.

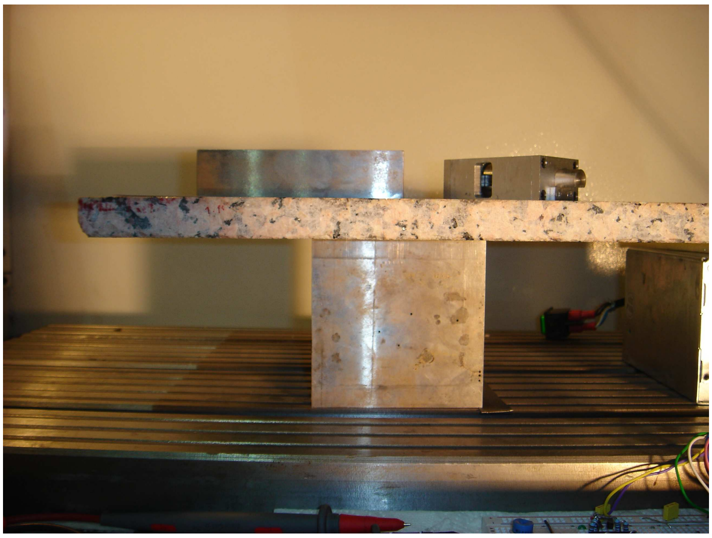

Figure 8.2 Granite is put on to a metal block

After setting the granite table precisely, the probe tests can be performed more accurately. At first, the magnets are put on to the magnet plate in accordance with the result obtained during the GMR sensor tests. Afterwards the probe is mounted on to the EDM body through two adapters of the EDM. At the beginning, the length of the top portion of the probe shaft or in other words magnet plate holder shaft is 30.00 mm respectively. However, the performed tests with this shaft were not relevant with the acquired data coming from the GMR sensor tests. The thing is that, when the stylus tip is moved by 1mm there has to be a change in the GMR voltage like 0.40 V or 0.50 V respectively. Unfortunately, with this length of magnet plate holder shaft the change in the GMR voltage is 0.10 V at most. So, undesired outputs are generated at the beginning of the tests. After the intensive works in order to solve the problem, it has seen that the magnet plate is moving very close to the boundaries of the defined operation region of the GMR sensors (Figure 3.7 in Chapter 3). So, the length of the magnet plate holder shaft is reduced and 3 different shafts are manufactured in order to acquire the best results. As a magnet plate holder shaft length, 28.00 mm, 28.50 mm and 29.00 mm shafts are manufactured and by those shafts calibration tests are performed. After evaluating the results of the calibration tests with different shaft lengths, one shaft will be selected for the overall tests. In Figure 8.3, location of the sensors and the test axes can be seen obviously.

During the calibration tests, probe’s stylus tip is moved along the directions shown in Figure 8.3 by 0.10 mm displacements including the Z –direction. In other words, stylus tip has given displacements inside the circle as shown in Figure 8.3. So the probe is evaluated in 9 axes respectively. In each axes the voltage values are read from the instrumentation amplifier circuit at 0 position and afterwards displacements are given by 0.10 mm and the corresponding voltage values are read from the circuit. When the tip is moved 1 mm. in total, the same procedure is repeated but in the opposite direction (backward direction). In other words, in all evaluation axes the stylus tip is given a displacement by 0.10 mm, starting from 0 – 1 mm (forward direction) and 1 – 0 mm (backward direction) respectively.

Furthermore, the probe's tip is moved along the GMR sensor axes by 1 mm. Thus the probe is evaluated in 15 axes totally.

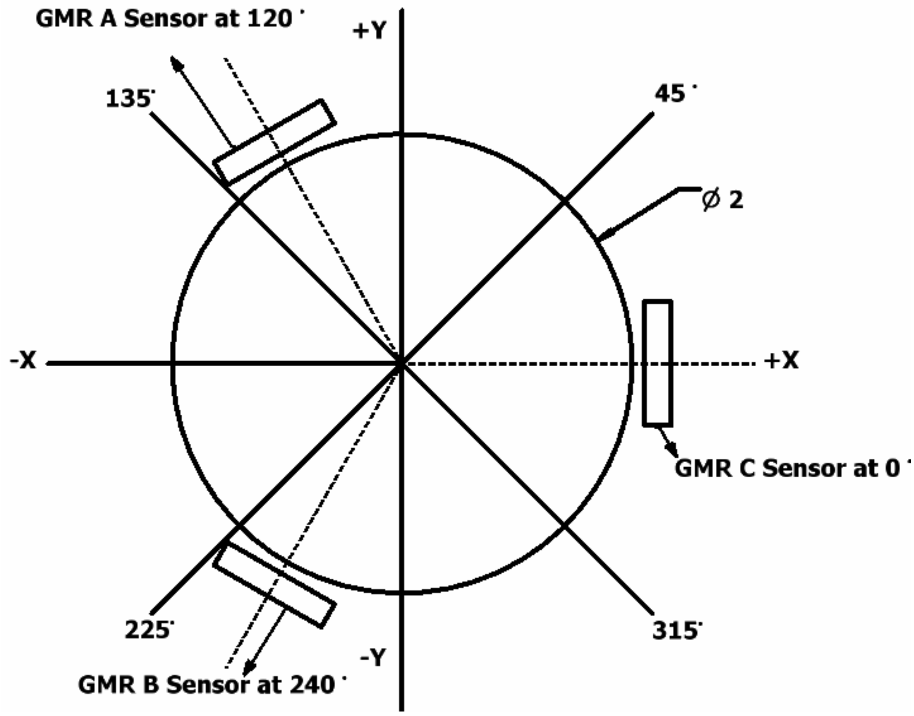

Figure 8.3 Sensor locations and test axes of the probe

Calibration tests; minimum step is 0.10 mm; is carried out via 3 different shaft lengths. In accordance with the acquired data, shaft with 28.50 mm length is preferred.

After defining the magnet plate holder shaft length, probe tests can be performed. Similarly, to the calibration tests, probe tests are performed in similar fashion, but the displacement amount of the tip of the probe is 0.20 mm at this time. Forward and backward operation is valid for those tests as well.

8.2 First Probe Tests

Probe tests are performed using a number of geometries acting as the spring plates. The thicknesses of those materials are 0.20, 0.3, and 0.40 mm respectively. Note that, at the beginning it was thought that, tests would be performed with 12 spring steel geometries with different thicknesses and shapes. Unfortunately, during the tests, it was observed that materials having 0.20 mm thickness experienced plastic deformation during the installation of the probe. Moreover, the weight of the stylus assembly affected the geometry. One of the spring steel geometry plastically deformed during the probe tests and one of them was bent during the sanding process. So, in total 7 different spring steel geometries are used during the probe tests. Figure 8.4 shows spring steel geometries.

a) SS-1: Spring steel-1 (thickness: 0.40 mm.),
b) SS-2: Spring steel-2 (thickness: 0.30 mm. and 0.40 mm.),
c) SS-3: Spring steel-3 (thickness: 0.30 mm. and 0.40 mm.),
d) SS-4: Spring steel-4 (thickness: 0.30 mm. and 0.40 mm.).

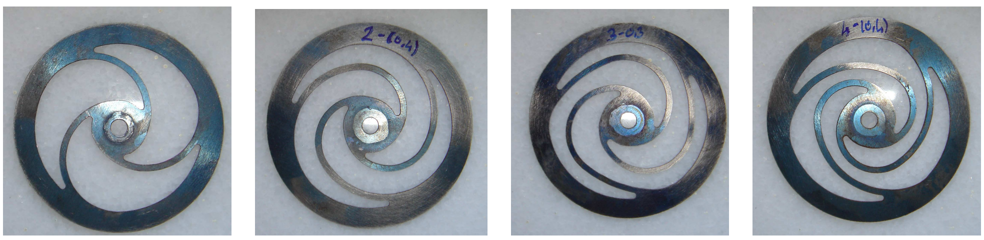

a) SS-1 **b)** SS-2 **c)** SS-3 **d)** SS-4

Figure 8.4 Spring Steel plates used in the experiments

During those tests, the magnets are placed on to the magnet plate. In order to obtain the maximum voltage difference in all directions, the radial distance is different for all the magnets. By doing this method, outputs generated from the GMR sensors still stay in the operation zone as indicated in Chapter 3 in Figure 3.7.

8.3 First Probe Test Results

In accordance with the created model in Chapter 7 the original and the model values are plotted in this section. From the acquired voltage values, model displacement values are obtained and model displacement and real displacement values are plotted. Furthermore, the error values estimated via root mean square method is also plotted for all of the spring steel geometries. During the model estimations, acquired data at x, y and z directions are evaluated together. Tests can be classified in to two groups;

1) tests at the equator,
2) tests below the equator at different latitudes, again in those latitudes probe is tested according to the Figure 8.3 (22.5 º, 45 º and 67.5 º).

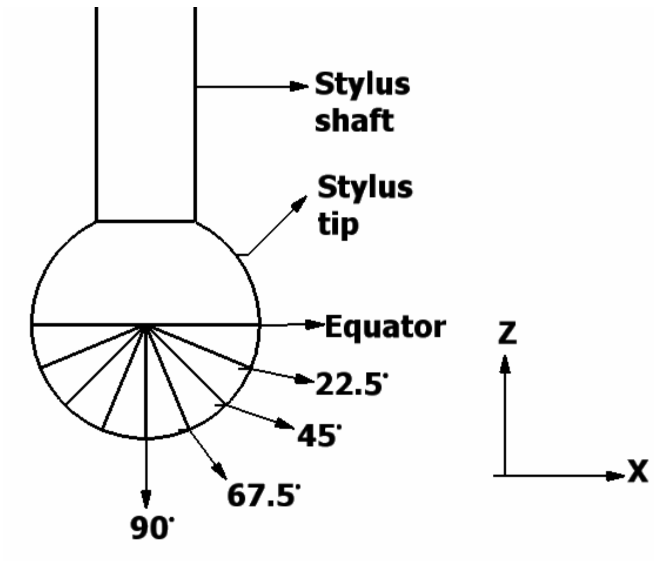

Figure 8.5 Test latitudes

In order to find the model displacement values more accurately, during the model estimations, Least Squares Method (LSM) is used. As can be seen from the below equations, model displacement values are obtained as follows;

$$\delta = A.V \tag{8.1}$$

$$\delta = \begin{bmatrix} \delta_x \\ \delta_y \\ \delta_z \end{bmatrix} \tag{8.2}$$

$$V = \begin{bmatrix} \Delta V_A \\ \Delta V_B \\ \Delta V_C \end{bmatrix} \tag{8.3}$$

$$A = \lfloor a_{ij} \rfloor_{3x3} \tag{8.4}$$

$$A = (V^T.V)^{-1}.V^T.\delta \tag{8.5}$$

Where δ is the displacement amount of the stylus tip, V is the voltage values read from related GMR sensors and A is the constant matrix. Through this method, matrix A can be found easily and after defining the matrix A, by virtue of the voltage values in Equation 8.1, model displacement values are obtained. As can be seen in Chapter 6, Equation 6.17 is employed to obtain a model displacement matrix. However, this model is dependent to the geometry of the probe (i.e: length of the stylus shaft etc.). Since, it is hard to obtain the exact values of the L_0 and R_m, another model is created. By virtue of this new model, LSM model, the constant matrix A is obtained through the acquired data coming from the tests. Furthermore, through the LSM model, the error amount between the measured and estimated value is reduced dramatically. More importantly, LSM model is directly dependent on the acquired test data, in other words constant matrix A is derived only from the acquired test data. The MatLab code is given in Table C.1 at Appendix C.

Test numbers indicated in the plots can be determined through the directions. 0 º - 180 º, 45 º - 225 º, 90 º - 270 º, and 135 º - 315 º. Since there are 4 major directions and 11 measurements were acquired from each of them, resulting 44 measurements in XY plane and adding the measurements coming from Z direction, total test number is 50.

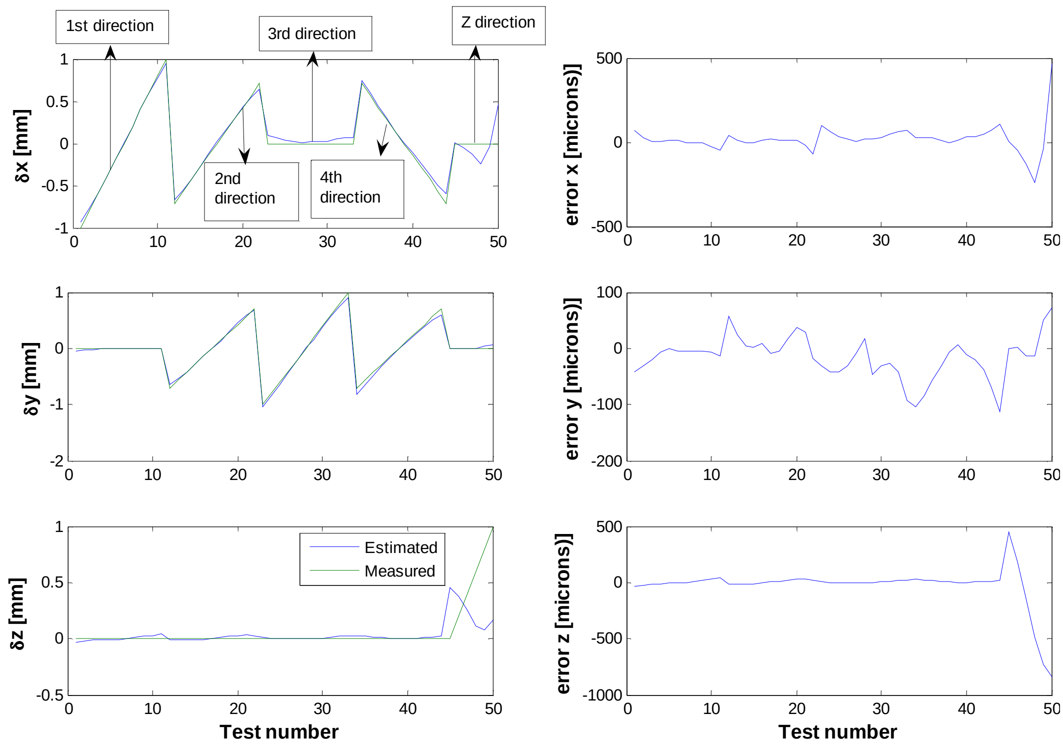

Figure 8.6 SS-1 (thickness: 0.40 mm) results

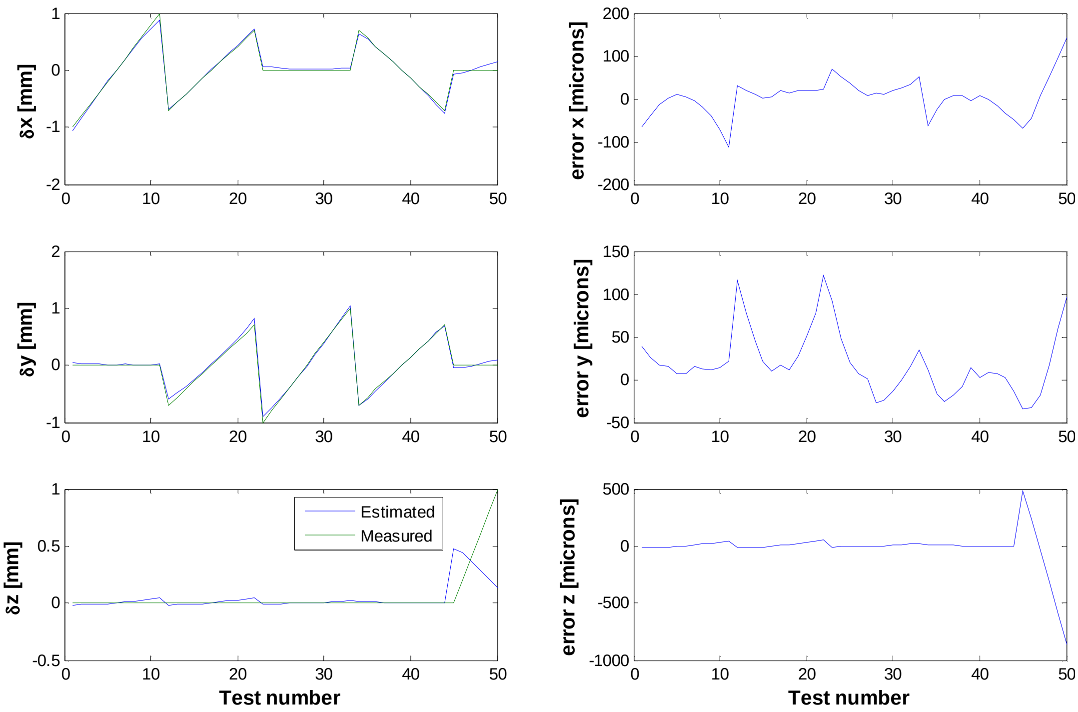

Figure 8.7 SS-2 (thickness: 0.30 mm) results

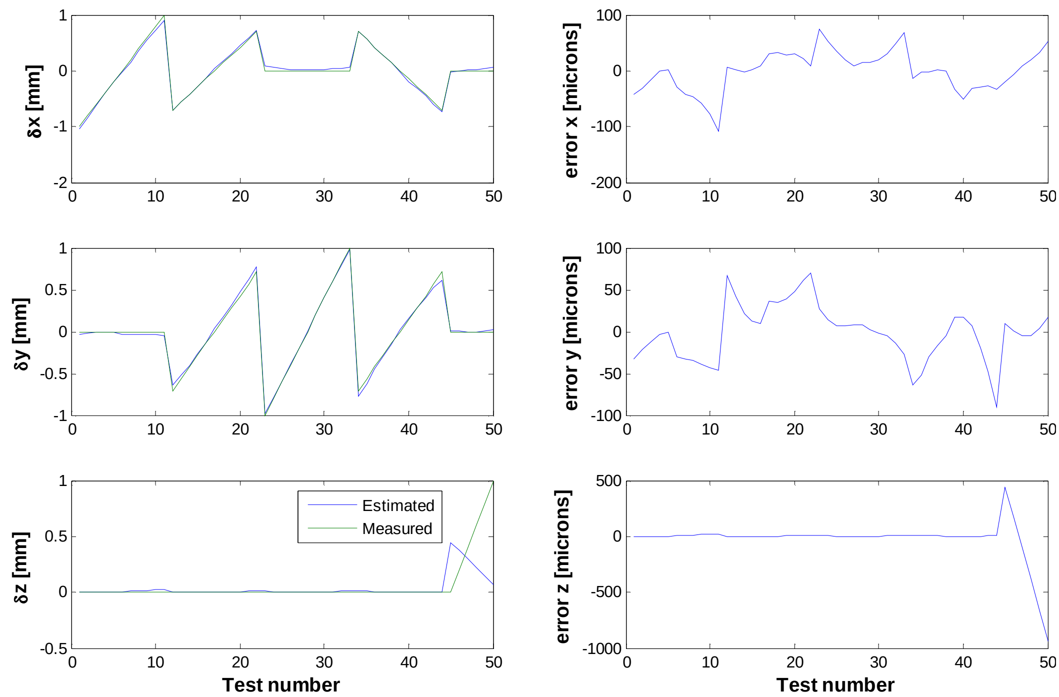

Figure 8.8 SS-2 (thickness: 0.40 mm) results

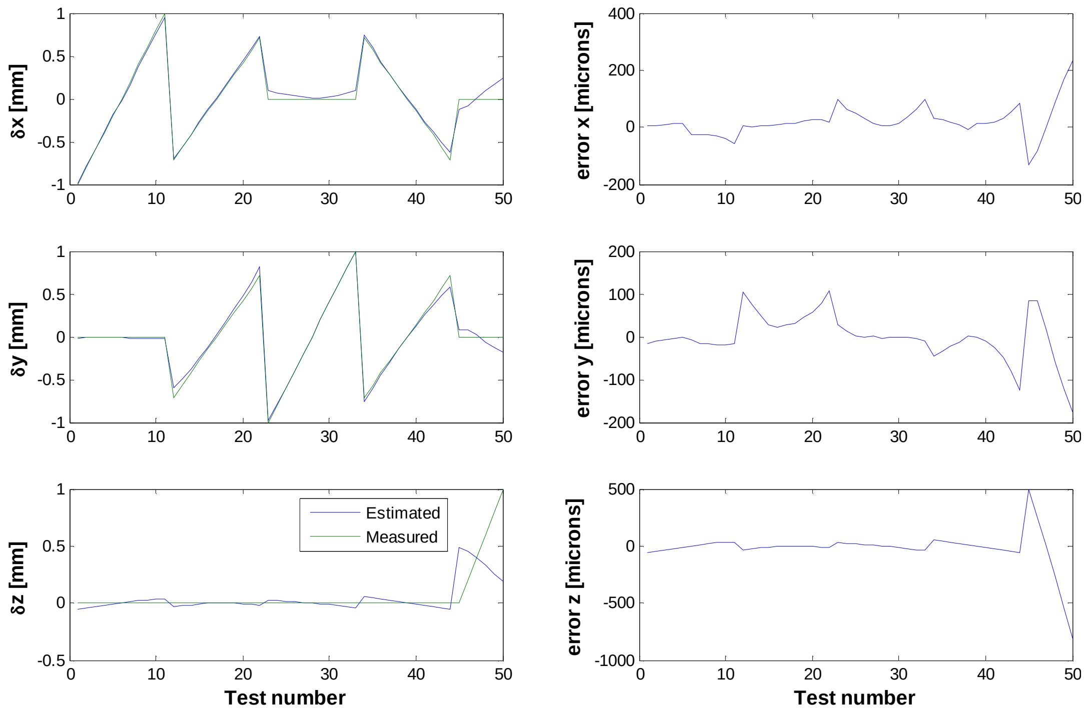

Figure 8.9 SS-3 (thickness: 0.30 mm) results

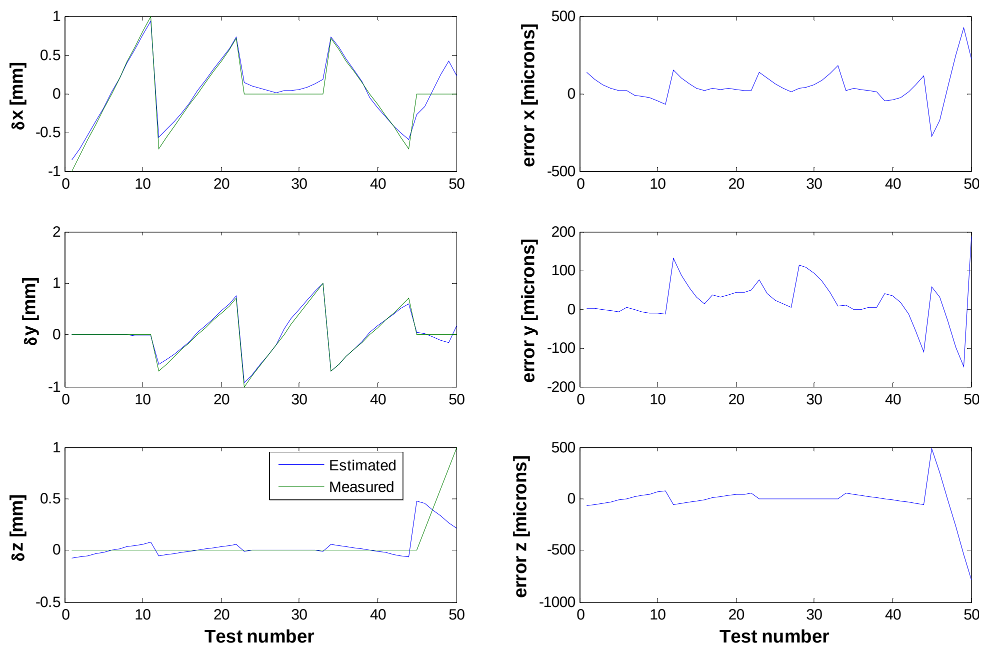

Figure 8.10 SS-3 (thickness: 0.40 mm) results

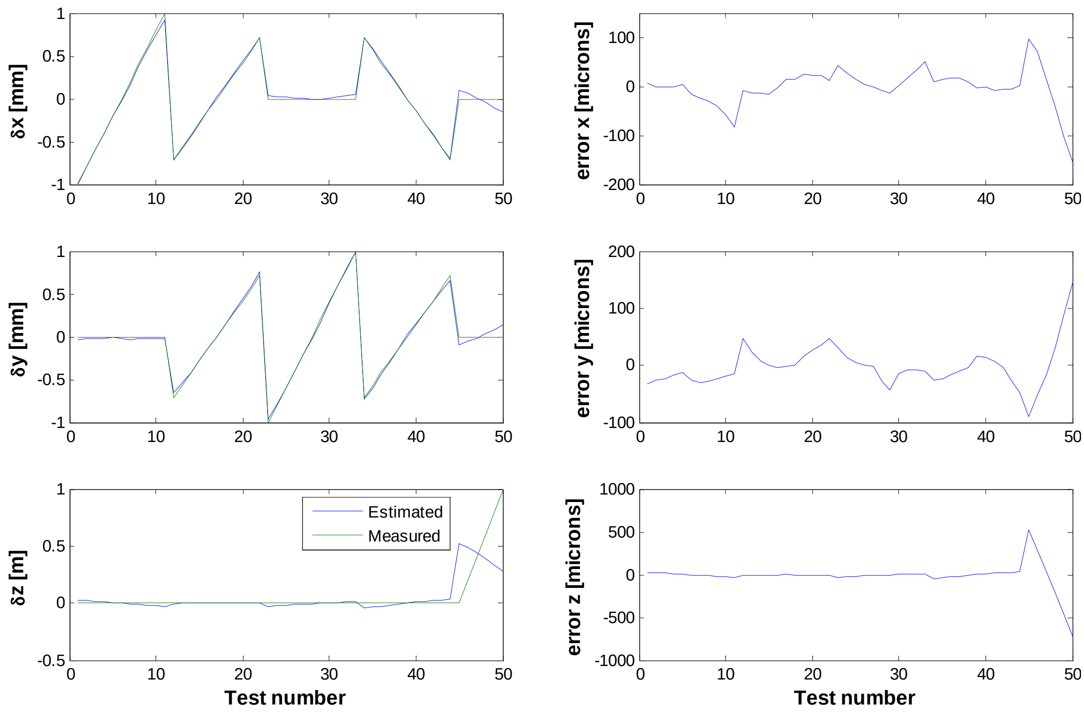

Figure 8.11 SS-4 (thickness: 0.30 mm) results

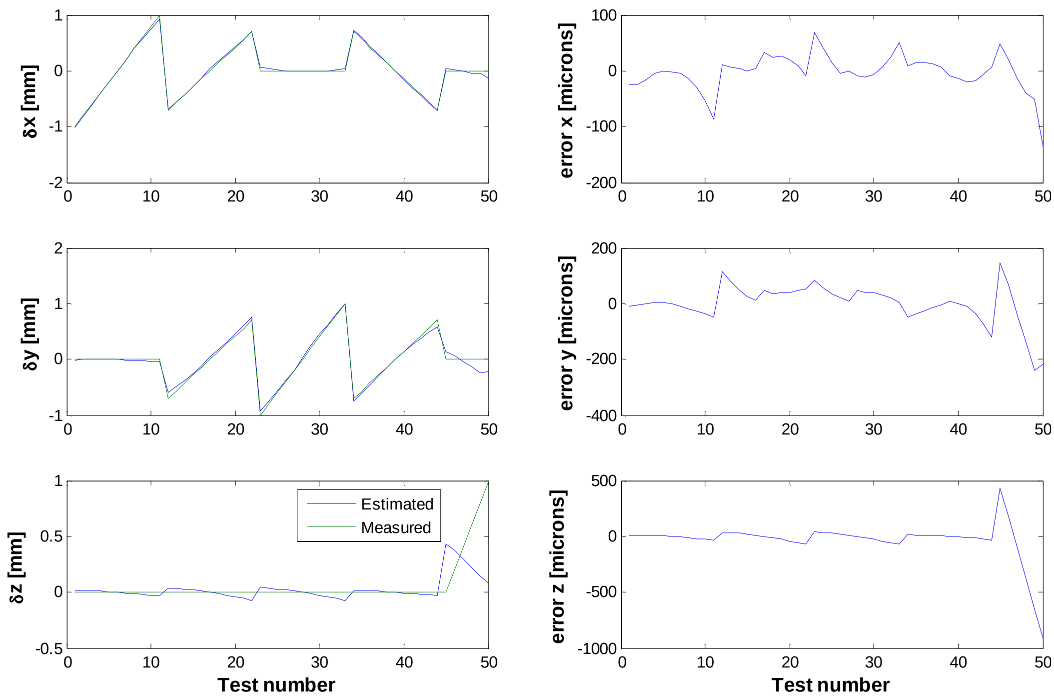

Figure 8.12 SS-4 (thickness: 0.40 mm) results

Results of the probe tests at different latitudes below equator are plotted as follows, SS-1 (thickness: 0.40 mm) is picked up;

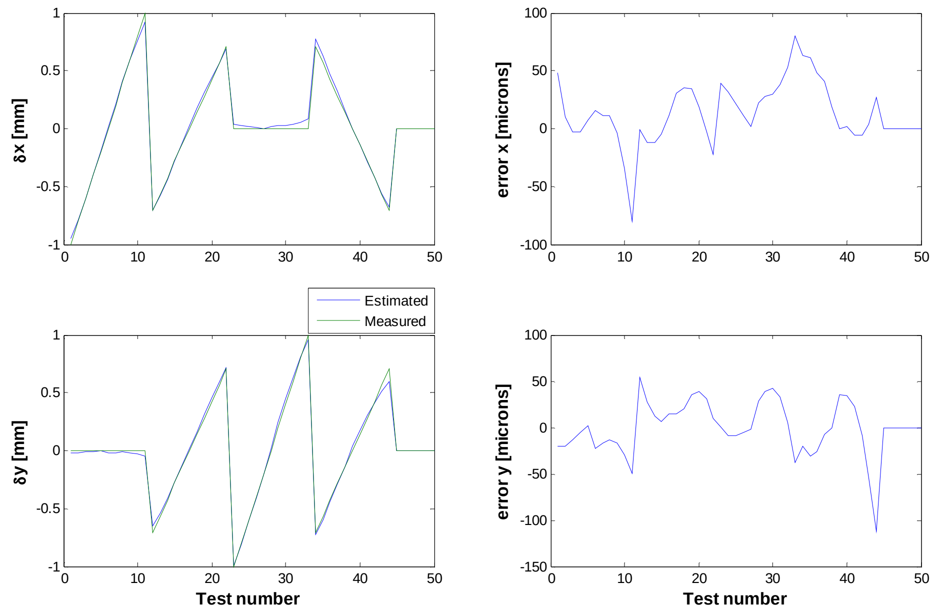

Figure 8.13 SS-1 (thickness: 0.40 mm) results at latitude 22.5 ° below equator

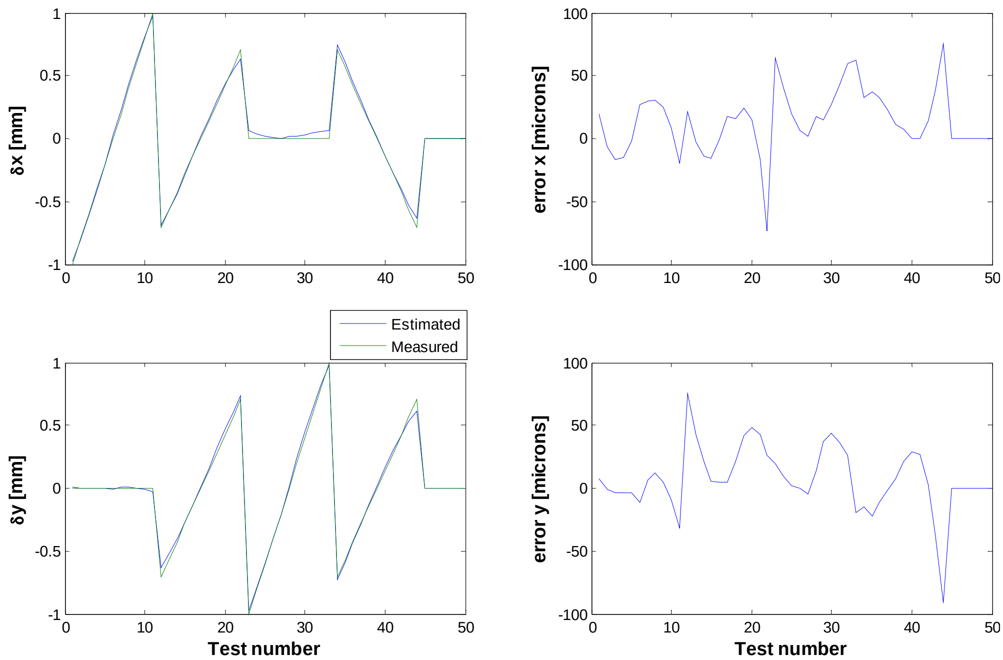

Figure 8.14 SS-1 (thickness: 0.40 mm) results at latitude 45 ° below equator

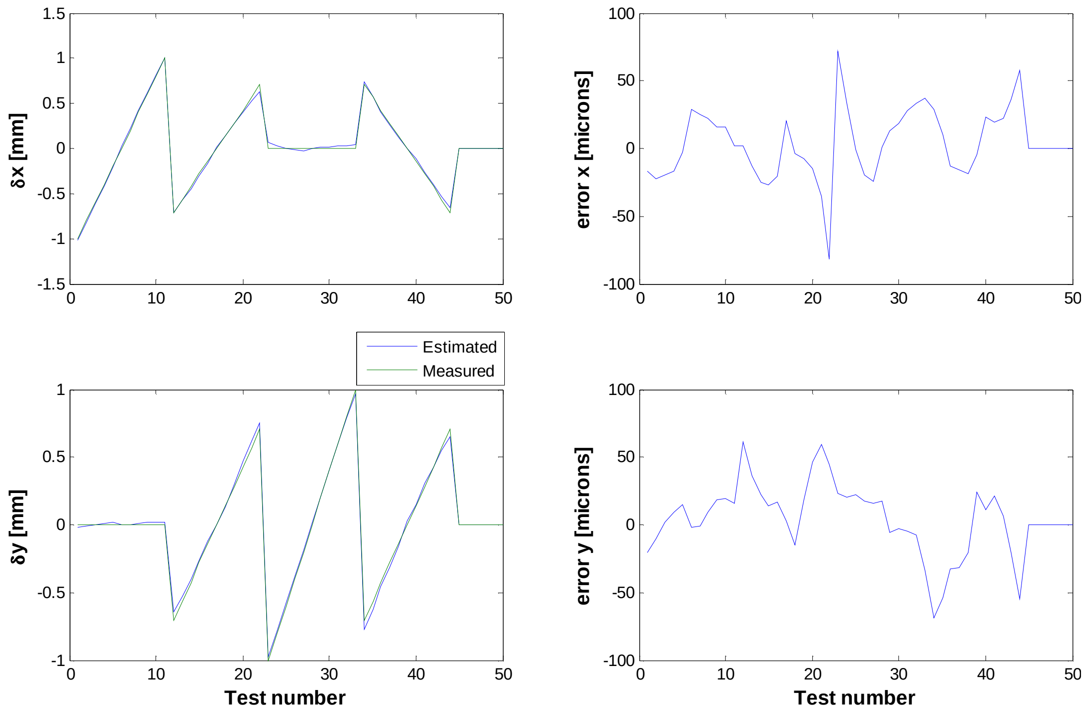

Figure 8.15 SS-1 (thickness: 0.40 mm) results at latitude 67.5 º below equator

According to the results obtained from the tests performed at the equator of the stylus tip, SS-4 (thickness: 0.30 mm) gave reasonable data, so evaluation of the probe with more axes (30 º , 60 º , 120 º , 150 º , 210 º , 240 º , 300 º and 330 º) is going to be carried out via this spring steel. Also SS-1 (thickness: 0.40 mm) is going to be tested with those angles to see whether this method will reduce the error in Z direction or not. In Figure 8.16, the evaluation angles can be seen obviously. Furthermore, during the tests performed at the equator of the stylus tip of the probe, it is observed that when the tip contacted with a part along the X –axis, tip also moved in Y-direction as well. So in order to test the probe more accurately and in order reflect the probe's performance more truly; during the tests performed at different latitudes; stylus tip is placed in a hole. So by virtue of this method, stylus tip will only move along the direction that it has to move.

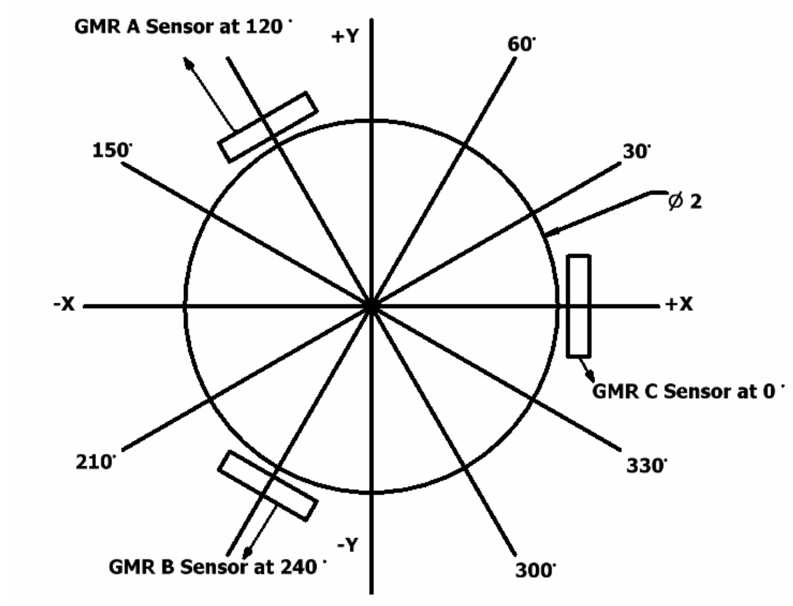

Figure 8.16 Newly defined test axes

In those tests, the minimum step in XY plane is 0.20 mm, and the minimum step in Z direction is 0.10 mm respectively. In order to reach the best result, more axes are added to the test procedure.

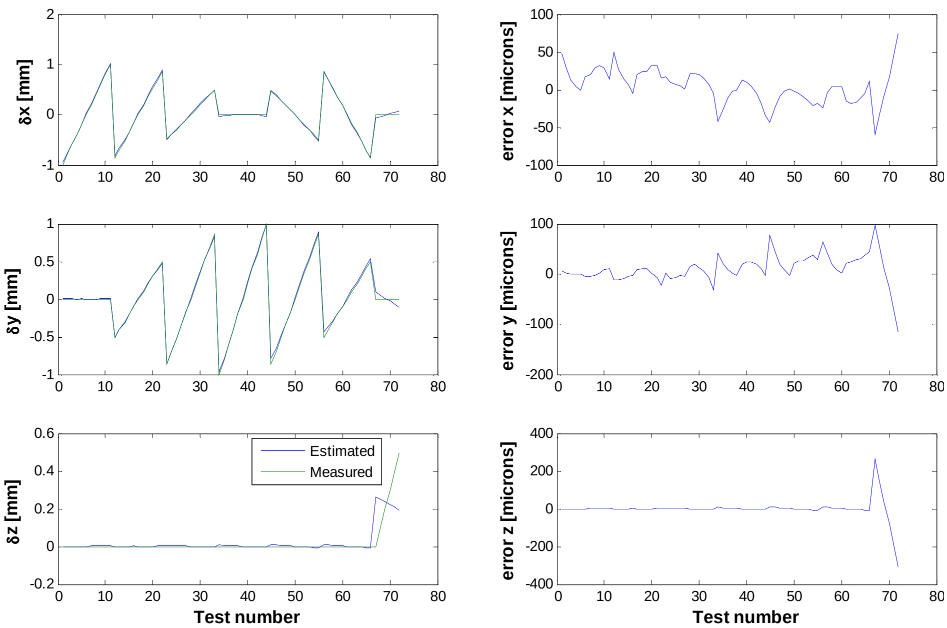

Figure 8.17 SS-4 (thickness: 0.30 mm) test results after a newly defined test axes

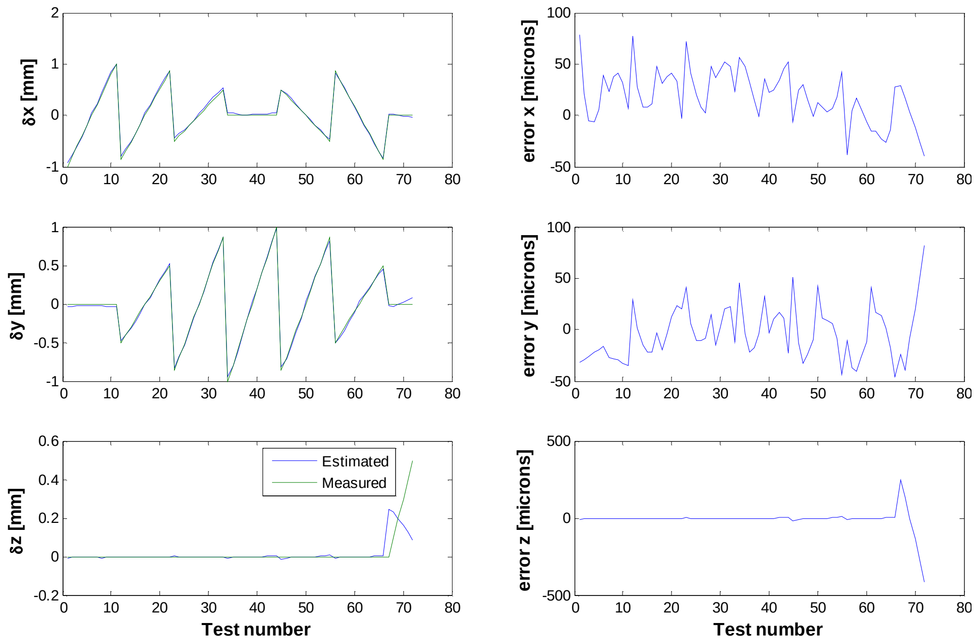

Figure 8.18 SS-1 (thickness: 0.40 mm) test results after a newly defined test axes

Results of the probe tests at different latitudes below equator for newly defined axes are plotted as follows, SS-4 (thickness: 0.30 mm) is picked up;

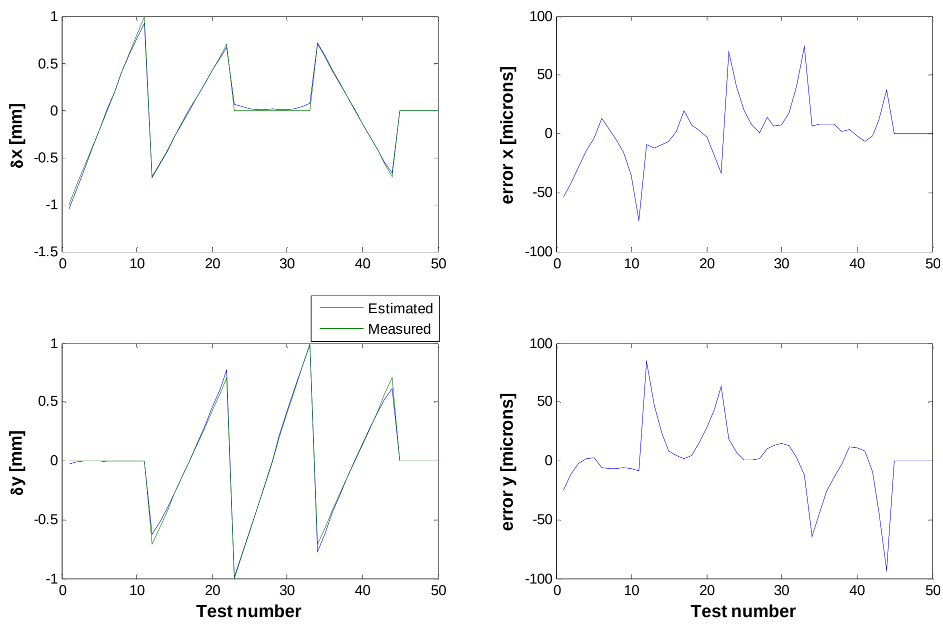

Figure 8.19 SS-4 (thickness: 0.30 mm) results at latitude 22.5 º below equator

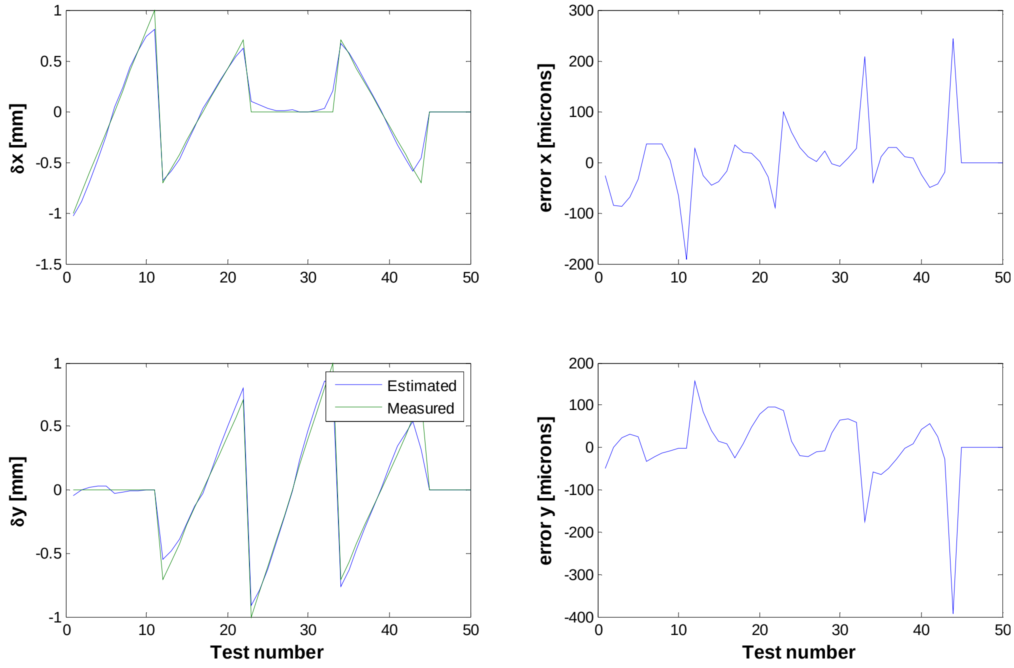

Figure 8.20 SS-4 (thickness: 0.30 mm) results at latitude 45 ° below equator

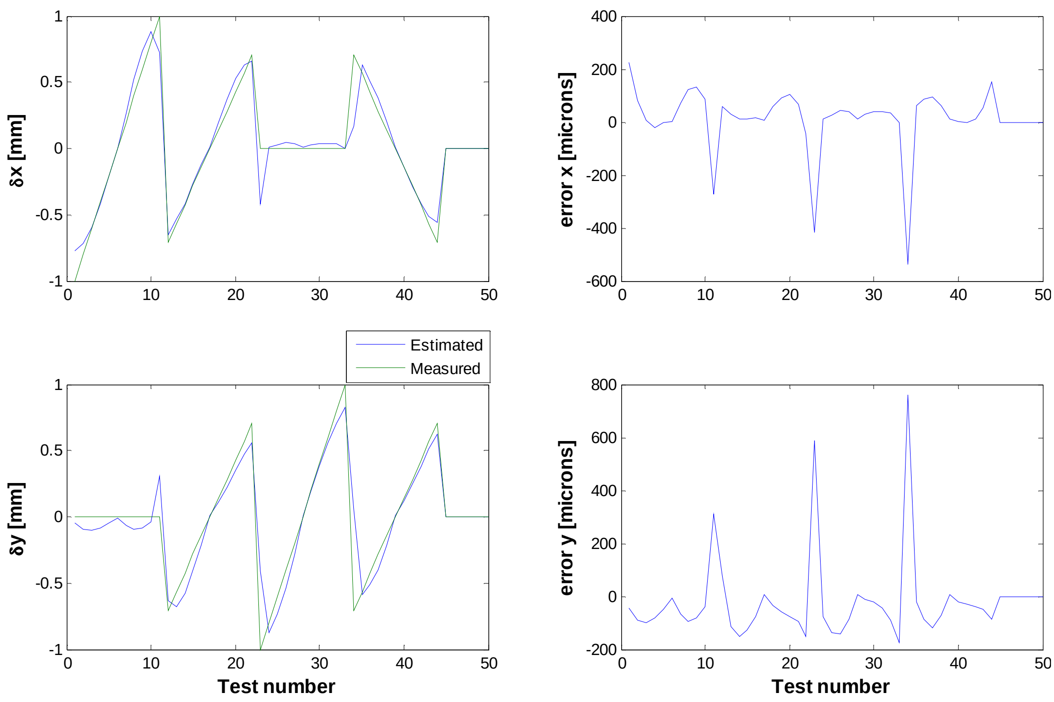

Figure 8.21 SS-4 (thickness: 0.30 mm) results at latitude 67.5 ° below equator

When the results are compared for SS-4 (thickness: 0.30 mm) and SS-1 (thickness: 0.40 mm); fixing the stylus tip via a hole reduces error in z direction in a considerable amount. In Figures 8.22, 8.23 and 8.24, two different test methods can be seen obviously.

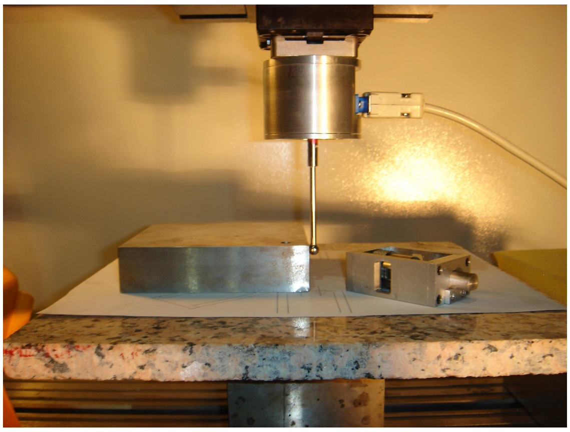

Figure 8.22 Tests with metal block and anvil gauge apparatus

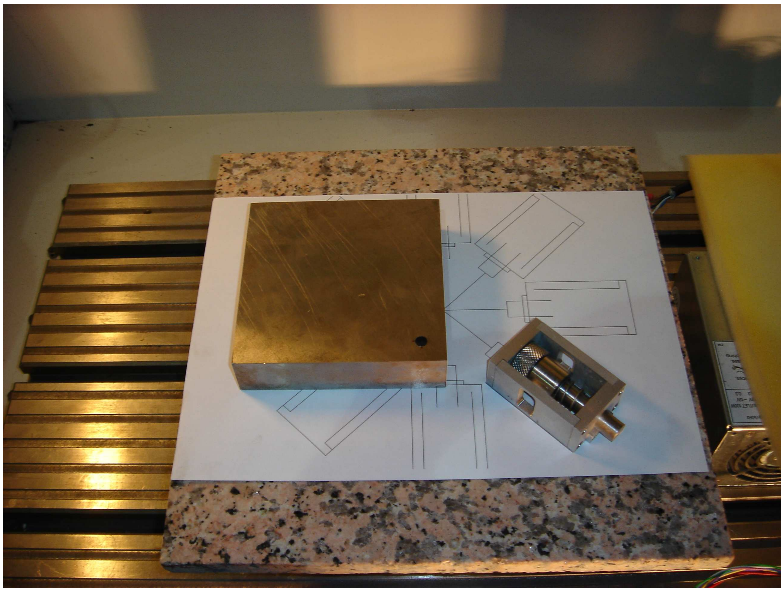

Figure 8.23 Arrangement of the steel block and the anvil gauge apparatus on the granite table

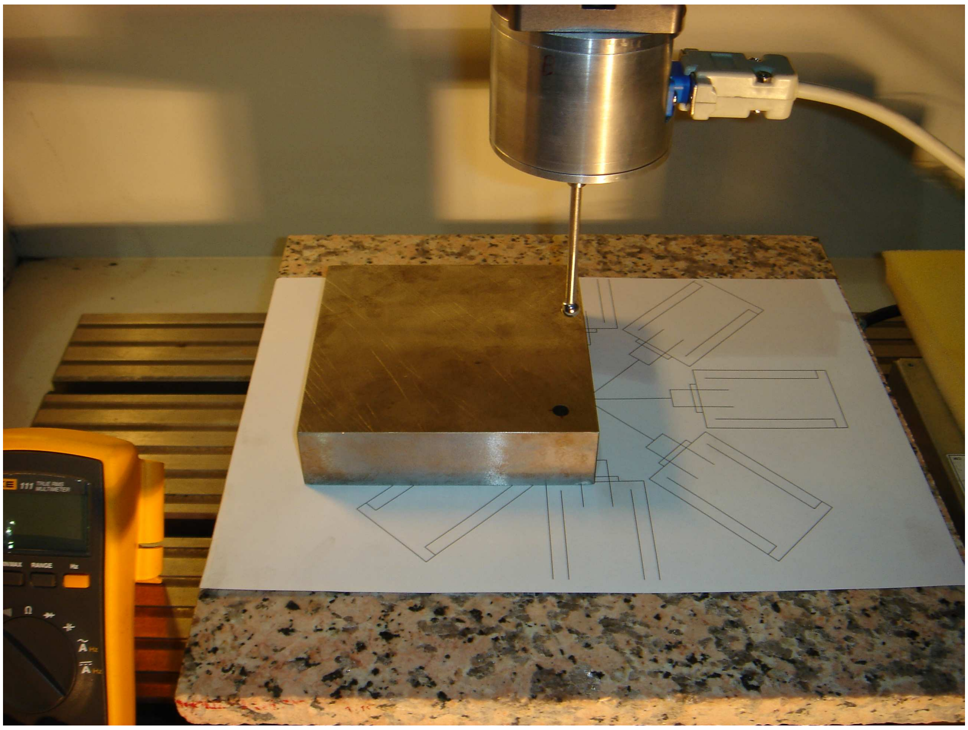

Figure 8.24 Stylus tip is fit inside a hole on the steel block

The magnitude of the error values are calculated through Root Mean Square (RMS) method, which is the statistical measure of the magnitude of a varying quantity. RMS values for the first probe obtained from different spring steel geometries are given in Tables 8.1 and 8.2.

$$RMS = \sqrt{\frac{1}{N}\sum_{i=1}^{N}(x_i - \hat{x}_i)^2} \tag{8.6}$$

Where $\hat{x}_i$ is the estimated displacement value of the stylus tip of the probe in accordance with the Least Squares Method (LSM) model, x_i is the measured displacement amount of the stylus tip of the probe.

During the tests, it is observed that, using a spring steel material as a magnet plate affected the voltage values read from GMR sensors at resting position. In accordance with Figure 3.7 in Chapter 3, adjusting the radial distance between 2.5 – 4 mm was reasonable. However, setting all magnets with the same radial distances did not result in the same voltage values read from the sensors. Furthermore, changing the polarity of the magnets on the magnet plate affects the voltage values as well. Thus, another material is selected in order to see the reason of this failure. Instead of using a spring steel material, stainless steel is preferred as a magnet plate. By virtue of the stainless steel's non-magnetic property, all GMR sensors generated approximately same voltage values when all the magnets are put in to the same radial distances. So spring steel's magnetic property somehow scatters the magnetic field lines or concentrates them and therefore the output voltages are affected dramatically. However, performed tests with stainless steel as a magnet plate told us that, GMR sensors generated the output in a different manner. Since the GMR sensors test are performed via spring steel material, hence the tests are performed again with the spring steel.

Table 8.1 Table of results at equator

Spring Steel Geometries	**At the equator**	
SS-1 (thickness: 0.40 mm)	RMS Error (x):	84.90 µm
	RMS Error (y):	40.20 µm
	RMS Error (z):	186.10 µm
SS-2 (thickness: 0.30 mm)	RMS Error (x):	42.87 µm
	RMS Error (y):	40.54 µm
	RMS Error (z):	172.15 µm
SS-2 (thickness: 0.40 mm)	RMS Error (x):	35.79 µm
	RMS Error (y):	33.07 µm
	RMS Error (z):	184.14 µm
SS-3 (thickness: 0.30 mm)	RMS Error (x):	58.84 µm
	RMS Error (y):	53.41 µm

Table 8.1 (Continued)

	RMS Error (z):	164.85 µm
SS-3 (thickness: 0.40 mm)	RMS Error (x):	109.73 µm
	RMS Error (y):	59.61 µm
	RMS Error (z):	163.33 µm
SS-4 (thickness: 0.30 mm)	RMS Error (x):	39.02 µm
	RMS Error (y):	35.77 µm
	RMS Error (z):	152.08 µm
SS-4 (thickness: 0.40 mm)	RMS Error (x):	32.58 µm
	RMS Error (y):	68.35 µm
	RMS Error (z):	182.98µm
SS-1 (thickness: 0.40 mm) with more axes	RMS Error (x):	31.83 µm
	RMS Error (y):	26.25 µm
	RMS Error (z):	69.25 µm
SS-4 (thickness: 0.30 mm) with more axes	RMS Error (x):	23.15 µm
	RMS Error (y):	30.06 µm
	RMS Error (z):	56.88 µm

Table 8.2 Table of results below equator

Below Equator		**SS-1 (thickness: 0.40 mm)**	**SS-4 (thickness: 0.30 mm)**
At 22.5 º	RMS Error (x):	29.65 µm	25.20 µm
	RMS Error (y):	28.83 µm	27.29 µm
At 45 º	RMS Error (x):	28.55 µm	64.84 µm
	RMS Error (y):	26.67 µm	76.28 µm
At 67.5 º	RMS Error (x):	25.79 µm	121.21 µm
	RMS Error (y):	26.26 µm	162.25 µm

8.4 Second Probe Tests

After examining the results acquired from the first probe tests, SS-4 (thickness: 0.30 mm) is used to test the second probe. As can be seen from Figure 8.25, and Figure 8.28**,** GMR sensors are located at the bottom part of the top lid. Due to the difficulty of the settlement of the GMR sensors under the top lid, bearings are used to raise the top lid. The reason why bearing are used for the raising purpose is due to their fine surface qualities at their ring rims. Therefore, by virtue of those bearings, the probe can be mounted to the EDM body without encountering any kind of obliquity.

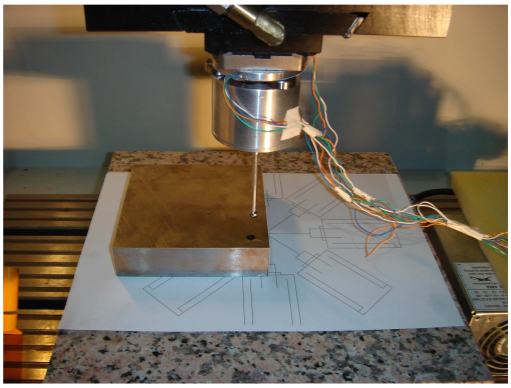

Figure 8.25 Second probe mounted on EDM

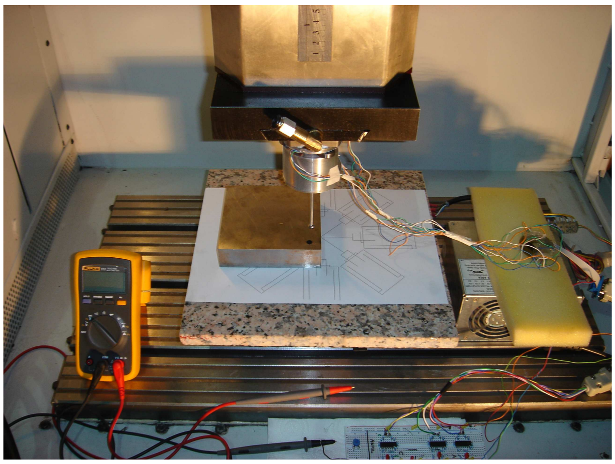

Figure 8.26 Test Setup

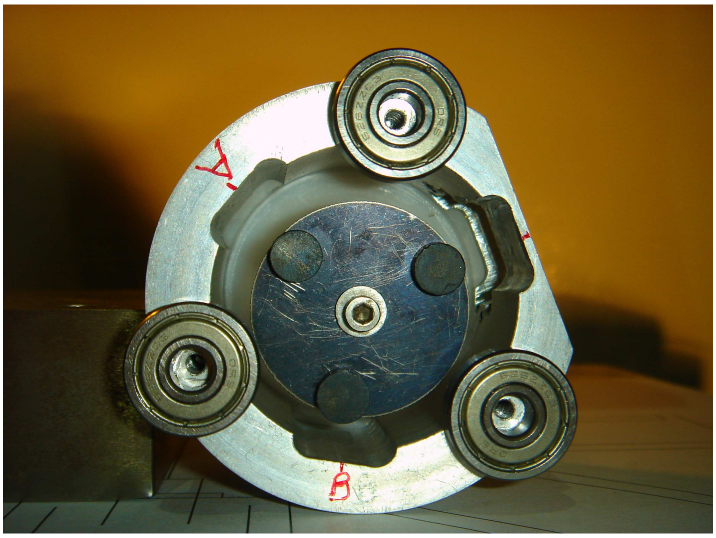

Figure 8.27 Inside view of the second probe, bearings are used for raising the top lid

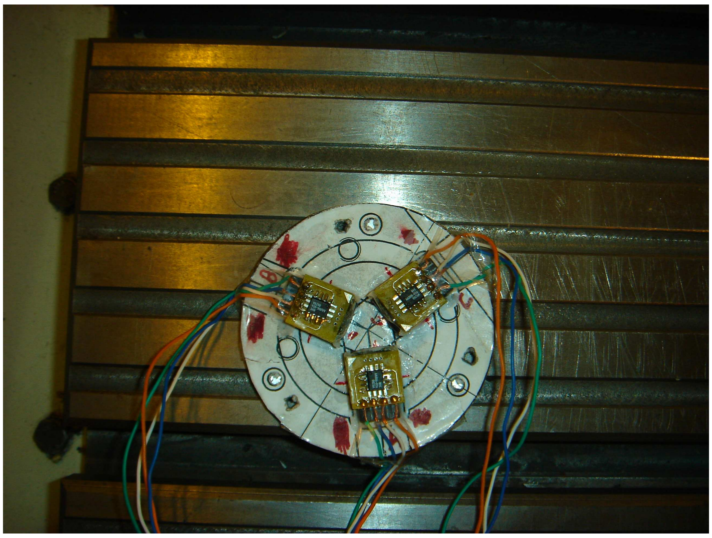

Figure 8.28 GMR sensor locations under the top lid

8.5 Second Probe Test Results

According to the created model through Least Squares Method (LSM), the original and the model values are plotted in this section. From the acquired voltage values, model displacement values are obtained and model displacement and real displacement values are plotted. Furthermore, the error values estimated via root mean square method is also plotted for SS-4 (thickness: 0.30 mm). During the model estimations, acquired data at x, y and z directions are evaluated together. Tests can be classified in to two groups;

1) tests at the equator stylus tip is fixed via hole,

2) tests below the equator at different latitudes, again in those latitudes probe is tested according to the **Figure 8.3** (22.5 º, 45 º and 67.5 º).

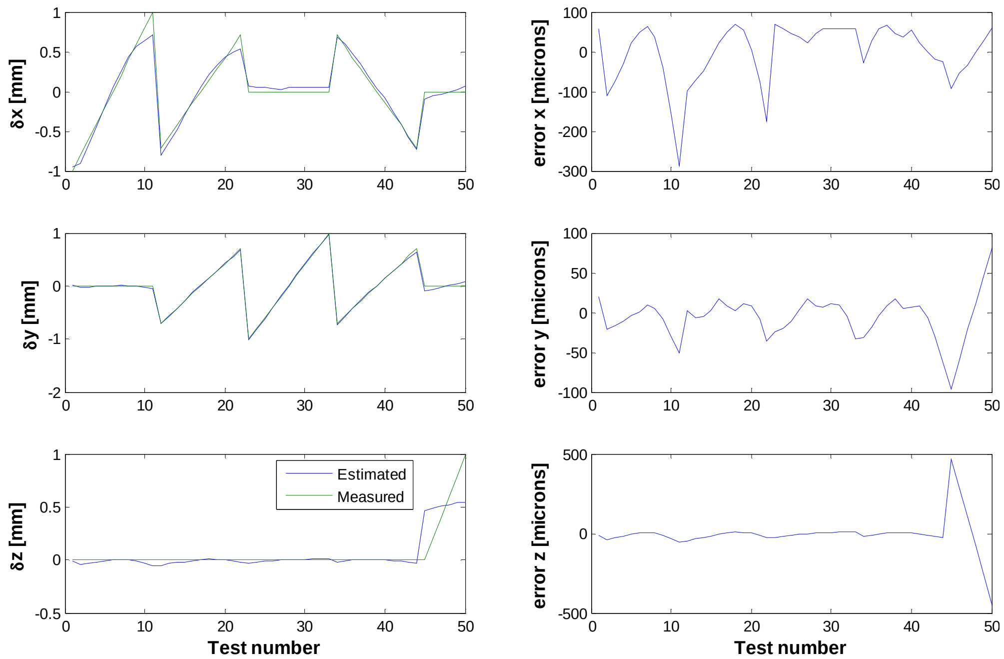

Figure 8.29 SS-4 (thickness: 0.30 mm) results

Results of the second probe tests at different latitudes below equator are plotted as follows;

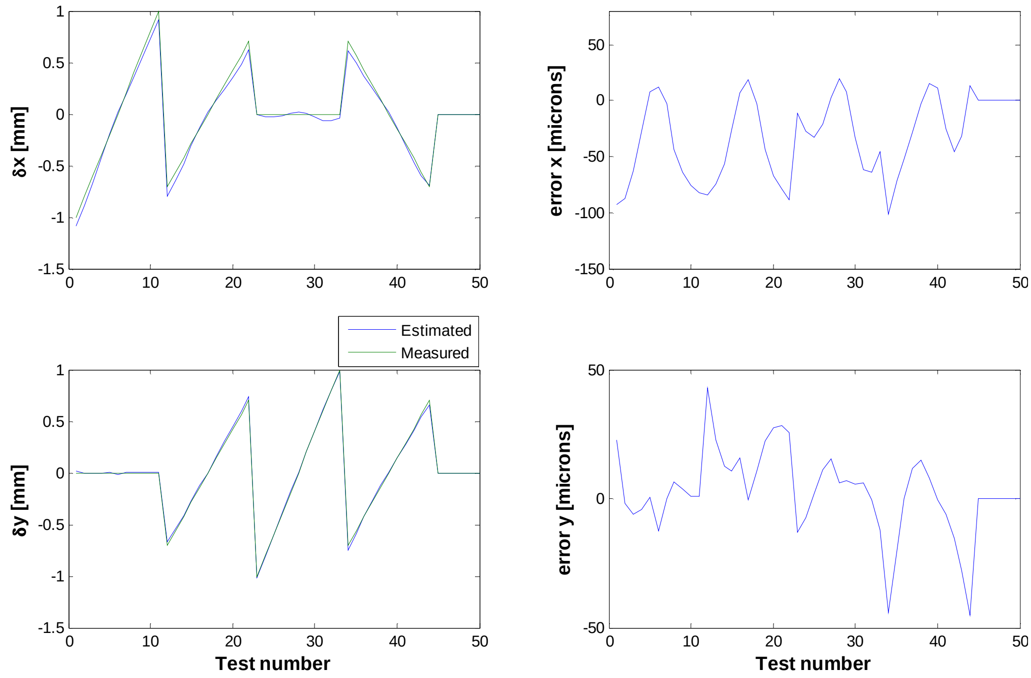

Figure 8.30 SS-4 (thickness: 0.30 mm) results at latitude 22.5 ° below equator

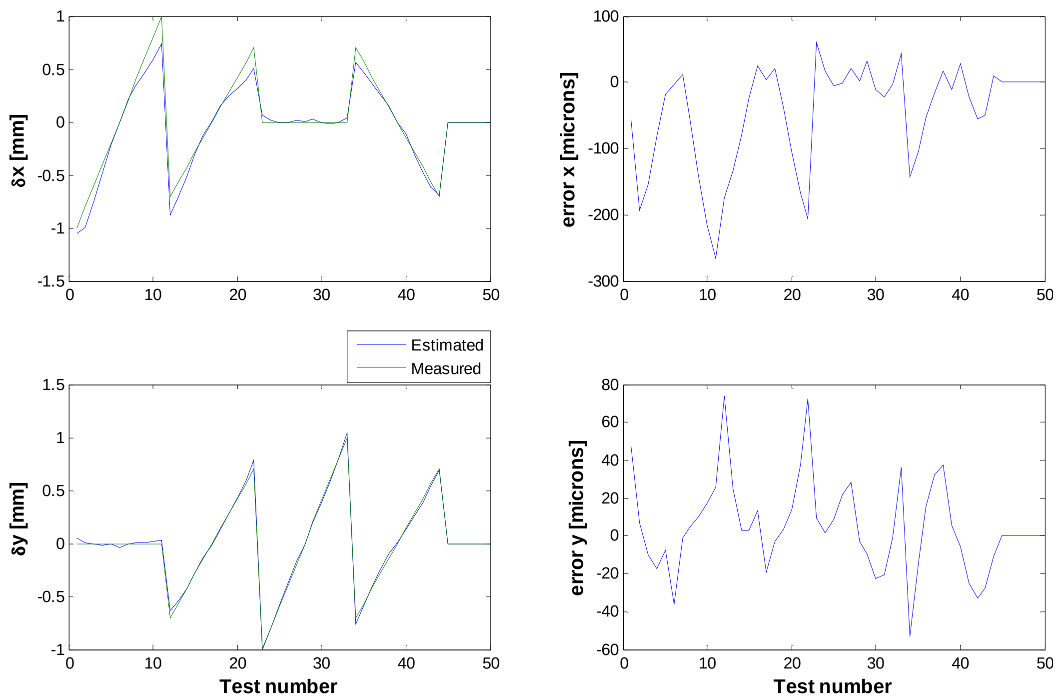

Figure 8.31 SS-4 (thickness: 0.30 mm) results at latitude 45 ° below equator

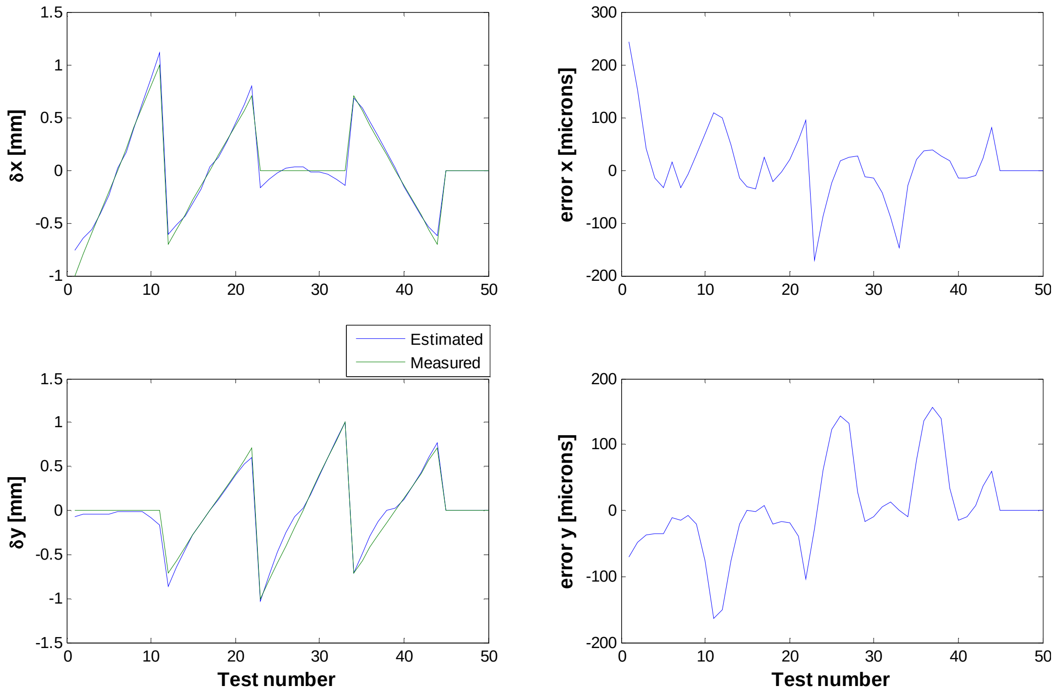

Figure 8.32 SS-4 (thickness: 0.30 mm) results at latitude 67.5 ° below equator

The magnitude of the error values are calculated via Root Mean Square (RMS) method and RMS values for the second probe is given in **Table 8.3.**

Table 8.3 Table of results

At equator		**SS-4 (thickness: 0.30 mm)**
RMS Error (x):		72.97 µm
RMS Error (y):		27.95 µm
RMS Error (z):		110.54 µm
Below Equator		**SS-4 (thickness: 0.30 mm)**
At 22.5 °	RMS Error (x):	47.84 µm

Table 8.3 (Continued)

	RMS Error (y):	16.32 µm
At 45 º	RMS Error (x):	89.44 µm
	RMS Error (y):	24.85 µm
At 67.5 º	RMS Error (x):	65.65 µm
	RMS Error (y):	66.56 µm

8.6 General Specification of EDM

Travel Span in XY plane: 430 mm x 315 mm.

Travel Span in Z direction: 400 mm.

Work table dimensions: 700 mm x 400 mm.

Work holder dimensions: 1050 mm x 650 mm x 450 mm.

Digital Reading Unit: 5 µm resolutions.

Max. workpiece load: 1000 kg.

8.7 Conclusion

In this chapter, tests of the two different probes and the results obtained from those tests are presented. At the beginning of the design procedure, anvil gauge is designed as a test apparatus. By virtue of this device, probe's stylus tip will be displaced at certain amounts. Furthermore, via the angled parts on the anvil gauge, probe will be tested not only at the equator, also at different latitudes below the equator as well. Later on, probe is mounted on Electro Discharge Machine's (EDM) body and the displacement amounts are given via the machine tool. So, in accordance with that case, anvil gauge apparatus is used during the experiments as a workpiece (as can be seen from Figures 8.22 and 8.23) while testing the probe at 45 º, 135 º, 225 º and 315 º.

As a major probe, first probe is tested via seven spring steel geometries that have different arm lengths respectively. After examining the results, it has seen that thickness and the length of the arms of the spring steels used during the experiments were vital. In other words, for instance experiments performed via SS-1 (thickness: 0.40 mm), it is observed that when the force is applied to the stylus tip through X-direction, due to the shape of the arms the tip is also moved in Y – direction as well. However, tests performed with other types of spring steel geometries, the above-mentioned problem is not met. At the beginning of the tests, calibration tests are performed to determine the optimum magnet plate holder shaft length and from those tests shaft with 28.50 mm length is picked up. Totally, 7146 experiments are carried out, 7146 times displacement is given to the stylus tip and 7146 times corresponding voltage values are read.

Additionally, in this chapter Least Squares Method (LSM) model is presented, model displacement values acquired thorough the voltage values and the real displacement values are compared. At first, experiments are performed with a steel block and the anvil gauge setup; but after encountering some undesired outputs, the stylus tip is fixed via a hole. By virtue of this method, stylus tip is forced to move only through the direction that force is applied. Moreover, via this method, error in Z direction is reduced in a considerable amount. In addition to that, it has seen that using spring steel material as a magnet plate affects the outputs generated from the GMR sensors dramatically. In accordance with the acquired results, SS-4 (thickness: 0.30 mm) is best choice for the first probe during the CMM application. Since, SS-4 (thickness: 0.30 mm) gave fine results for the first probe, it is selected as a reference plane for the second probe.

CHAPTER 9

CONCLUSION AND FUTURE WORK

The contribution of this thesis to the dimensional metrology is to develop a novel touch trigger / measurement (also be used as a scanning probe) probe that has different characteristics if compared to the other probes currently in use in the industry. The developed touch trigger / measurement probe for Coordinate Measuring Machines takes the advantage of GMR sensor technology. In this thesis, three different devices are proposed; two types of prototype touch trigger probe, and a measurement device; anvil gauge.

The tests are performed on a 3-axis CNC Electro Discharge Machine (EDM). The most significant conclusion from this work is that it is possible to design a GMR sensor based probe for use on CMMs. The performed tests can be categorized in to two groups; tests carried out in order to determine the directional sensitivity of the GMR sensor which is the basic design parameter for the location of the sensors, and the tests carried out for the proposed probe on a 3 axis CNC EDM. Two different probes were tested during the experiments. In total 7146; for the first probe 5958 experiments [(9 directions x 12 measurements x 3 sensors x 7 geometry) + (13 directions x 12 measurements x 3 sensors x 2 geometry) + (5 directions x 22 measurements x 3 sensors x 3 shafts) + 36 directions through the GMR sensor axes + (8 direction x 12 measurement x 3 sensors x 3 latitudes x 2 geometry)], for the second probe 1188 experiments [(9 directions x 12 measurements x 3 sensors) + (8 directions x 12 measurements x 3 sensors x 3 latitudes)] were performed, in other words 7146 times output values are read from GMR sensors. In accordance with the obtained data from the model, using the first probe with a spring steel geometries having the longest arm lengths also fixing the stylus tip gave fine results. Moreover, the installation process of the second probe plays an important role for the performance of this probe. Since, GMR sensors were located under the top lid of the probe; there was a handicap to adjust the magnet position precisely.

The work presented here proves the capabilities of GMR based probe for use on CMMs. Since the proposed probe is the first prototype, it can be developed in future in order to reach a resolution in the micrometer range. This is due to the application of GMR technology, proper mechanical design, and keeping proper metrological feasibilities. This result will encourage further use of GMR sensor technology in dimensional metrology.

In order to avoid the ambiguities that will affect the probe's measurement quality and accuracy, the tests are going to be performed in a controlled environment and in order to reach the best performance, at first there is a need for a magnetic shield for the whole system. In accordance with that, as a magnet plate material, stainless steel has to be used for isolating the system from the magnetic effects. Another option is to model the magnetic specifications of the spring steel with the magnets on it. So doing this simulation will lead us a better knowledge on the magnetic associated issues. As a result, in brief a magnetic circuitry has to be designed to avid the magnetic biasing dramatically.

Moreover, in order to reduce the vibration of the stylus shaft during forward and backward probing task, there is a need for damping mechanism to reduce those vibrations especially in thinner spring steel plates. Another option for the damping issue, an additional spring steel plate can be used in the probe. By virtue of this additional spring plate, damping problem can be solved dramatically.

Another point is the improvements of the current design. First of all, the length of the magnet plate holder shaft can be reduced in order to reduce the magnet plate deviations during the tests performed along the Z-direction. By virtue of this modification, magnet plate will come near to the reference plane. Besides this, in order to avoid the rotational motion of the magnet plate, magnet plate can be fixed to the reference plane or to the probe body, in other words, there is a need for a lock mechanism. However, an additional spring plate will solve this problem more properly.

APPENDIX A

SOURCE CODE OF THE PROBE'S FIRMWARE

Firmware of the microcontroller is developed by CCS S. PIC18F88 (8-bit RISC) microcontroller running at 20 MHz is used to calculate the stylus displacements.

Table A.1 C source code of the probe's firmware.

```
#include <16F88.h>
#device ADC=10
#fuses HS,NOWDT,NOPROTECT,NOLVP
#use delay(clock=20000000)
#use rs232(baud=19200,xmit=PIN_B5,rcv=PIN_B2)
#use fast_io(B)
#opt 9
//
// Constants: c = (L1+Lm)/L0,  d = L0/(3*Rm),  a0 = h - c*L0
//
const float a0 = 2, r0 = 2.5, c = 0.9, d = 1.037037;
float k1 = 2, k2 = 0.02;
float dx, dy, dz, va0, vb0, vc0;
float aa = 0, ab = 0, ac = 0;
int1 iflag = 0;
//
// External interrupt service routine
//
#INT_EXT
void isr(void) {
  iflag = 1;
  delay_ms(200); /* Debounce */
}
//
// Function to read GMR voltages
//
float GMR_out(char ch) {
  float adc = 0;
  switch(ch) {
    case 'a': set_adc_channel(2); break;
    case 'b': set_adc_channel(0); break;
    case 'c': set_adc_channel(1); break;
  }
  delay_us(50);
```

```
  adc = read_ADC()*0.004888;
  delay_us(50);
  return(adc);
}
void main() {
//
// Setup I/O ports
//
  set_tris_a(0xFF);
  set_tris_b(0x0F);
//
// Configure A/D converter
//
  setup_adc_ports(sAN0|sAN1|sAN2);
  setup_adc(ADC_CLOCK_DIV_2);
//
// Enable external interrupt (RB0)
//
  enable_interrupts(GLOBAL);
  enable_interrupts(INT_EXT);
  ext_int_edge(H_TO_L);
//
// Read the voltages at the neutral point
//
  va0 = GMR_out('a');
  vb0 = GMR_out('b');
  vc0 = GMR_out('c');
  k1 -= k2*r0;
  k2 *= c;
 while(TRUE) {
  //
  // Axial displacements of GMR sensors
  //
    aa = (GMR_out('a') - va0 + aa*a0)/(k1-aa);
    ab = (GMR_out('b') - vb0 + ab*a0)/(k1-ab);
    ac = (GMR_out('c') - vc0 + ac*a0)/(k1-ac);
  //
  // Stylus displacements
  //
    dx = d*(2*aa-ab-ac);
    dy = d*1.732051*(ab-ac);
    dz = -0.333333*(aa+ab+ac);
  //
  // Radial displacements
  //
    aa = 0.5*k2*dx; ac = 0.866*k2*dy;
    ab = aa - ac;
    ac += aa;
    aa *= -2;
  //
  // Generate trigger signals
  //
    if ((dx>0.05) || (dx<-0.05))
      output_high(PIN_B7);
    else
      output_low(PIN_B7);
    if ((dy>0.05) || (dy<-0.05))
      output_high(PIN_B6);
    else
```

```
      output_low(PIN_B6);
    if (dz>0.05)
      output_high(PIN_B4);
    else
      output_low(PIN_B4);
  //
  // On interrupt, send out all estimates (in microns)
  //
    if (iflag) {
      printf("DX = %ld\n\r",dx*1000);
      printf("DY = %ld\n\r",dy*1000);
      printf("DZ = %ld\n\n\r",dz*1000);
      iflag = 0;
    }
  }
}
```

APPENDIX B

DATA SHEET OF GMR SENSORS

B.1 Characteristics of AA type GMR Sensors

Nonvolatile Electronics Corporation’s (NVE Corporation) GMR sensors are used during building the sensing stage of the designed probe. AA type magnetic sensors are used for the designed probe. Part number is AA006-02 as per GMR sensors data book of NVE Corporation.

The basic AA series GMR sensors are general purpose magnetometers for use in a wide variety of applications. They exhibit excellent linearity, a large output signal with applied magnetic fields, stable and linear temperature characteristics, and a purely ratiometric output [30].

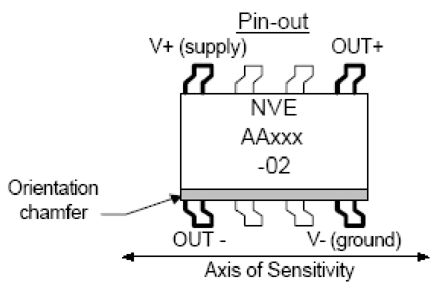

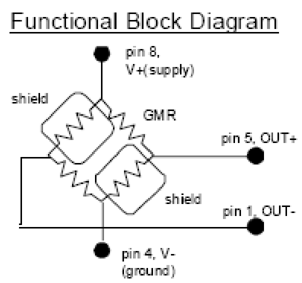

Figure B.1 NVE’s AAxxx-02 type GMR sensors [30]

Table B.1 Magnetic Characteristics [30]

Part Number	Saturation Field (Oe)	Linear Range (|Oe |)		Sensitivity (mV/V-Oe)		Resistance (Ohms)	Package	Die Size (μm)
		Min	Max	Min	Max			
AA002-02	15	1.5	10.5	3.0	4.2	5K ± 20%	SOIC8	436x3370
AA003-02	20	2.0	14	2	3.2	5K ± 20%	SOIC8	436x3370
AA004-00	50	5	35	0.9	1.3	5K ± 20%	MSOP8	411x1458
AA004-02	50	5	35	0.9	1.3	5K ± 20%	SOIC8	411x1458
AA005-02	100	10	70	0.45	0.65	5K ± 20%	SOIC8	411x1458
AA006-00	50	5	35	0.9	1.3	30K ± 20%	MSOP8	836x1986
AA006-02	50	5	35	0.9	1.3	30K ± 20%	SOIC8	836x1986

Table B.2 General Characteristics [30]

Property	Min	Typical	Max	Unit
Input Voltage Range	<1		± 25	Volts
Operating Frequency	DC		> 1	MHz
Operating Temperature Range	-50		125	°C
Bridge Electrical Offset	-4		+4	mV/V
Signal Output at Max. Field		60		mV/V
Nonlinearity			2	% (unipolar)
Hysteresis			4	% (unipolar)
TCR		+0.14		% / °C
TCOI		+0.03		% / °C
TCOV		-0.1		% / °C
Off Axis Characteristic		Cos β		
ESD Tolerance		400		V pin to pin HBM

In these tables;

- 1 Oersted (Oe) = 1 Gauss in air
- GMR AA Series sensors are pure ratiometric devices, meaning that they will operate properly at extremely low supply voltages. The output signal will be proportional to the supply voltage. Maximum voltage range is limited by the power dissipation in the package and the maximum operating temperature of the sensor.
- Unipolar operation means exposure to magnetic fields of one polarity, *e.g.,* 0 to 30 Gauss, or -2 to -50 Gauss, but not -20 to +30 Gauss (bipolar operation). Bipolar operation will increase nonlinearity and hysteresis.
- TCR is resistance change with temperature with no applied field. TCOI is the output change with temperature using a constant current source to power

the sensor. TCOV is the output change with temperature using a constant voltage source to power the sensor.

- Beta (β) is any angle from the sensitive axis.

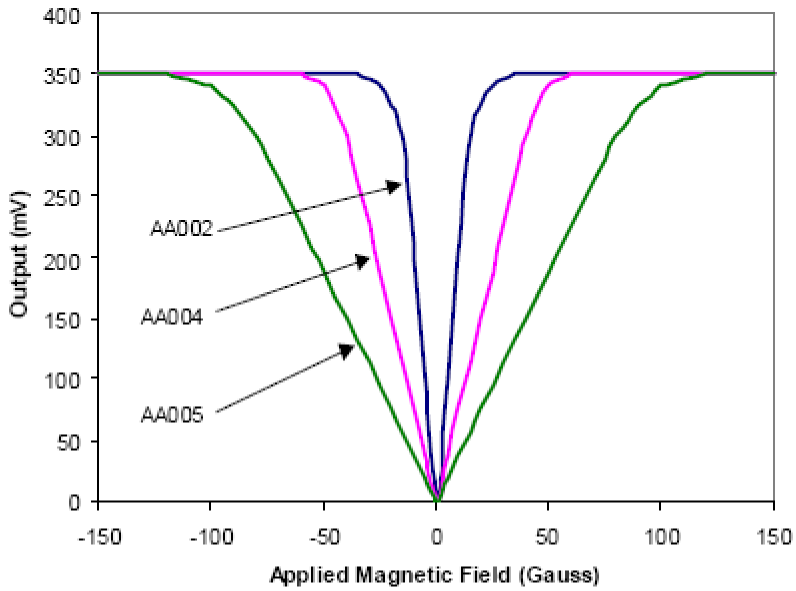

Figure B.2 GMR Voltage vs. Applied Magnetic Field Graph [30]

APPENDIX C

MATLAB DOCUMENTS OF THE KINEMATIC MODELS OF THE PROBES

C.1 M-File Program of the Kinematic Models of the Probes

In accordance with the acquired voltage data, via Least Squares Method (LSM), constant matrix A is found. Afterwards, using this constant matrix A, estimated displacement values are found. By virtue of this code, measured and estimated displacement values and the error amounts are plotted. Moreover, the magnitude of the error is calculated via Root Mean Square (RMS) method.

Table C.1 MatLab source code of the kinematical model.

```
GMR_A_sensor; GMR_B_sensor; GMR_C_sensor; close all
d = linspace(-1,1,11)'; dz = [0 0 0 0 0 0 0 0 0 0 0 0 0 0 0 0 0 0 0 0 0 0 0 0 0 0 0 0 0 0 0 0 0 0 0 0 0 0 0 0 0 0 0 0 0 0 0 0.2 0.4 0.6 0.8 1]';
VA_0  =[[flipud(Af_0(2:6));  Af_180]-Af_0(1)  [flipud(Ab_0(2:6));  Ab_180]-Ab_0(1)]*[.5 .5]';
VA_45   =   [[flipud(Af_45(2:6));   Af_225]-Af_45(1)   [flipud(Ab_45(2:6)); Ab_225]-Ab_45(1)]*[.5 .5]';
VA_90   =   [[flipud(Af_90(2:6));   Af_270]-Af_90(1)   [flipud(Ab_90(2:6)); Ab_270]-Ab_90(1)]*[.5 .5]';
VA_135  =  [[flipud(Af_135(2:6));  Af_315]-Af_135(1)  [flipud(Ab_135(2:6)); Ab_315]-Af_135(1)]*[.5 .5]';
VA_Z = [Af_Z Ab_Z]*[.5 .5]';
VB_0  =  [[flipud(Bf_0(2:6));  Bf_180]-Bf_0(1)  [flipud(Bb_0(2:6));  Bb_180]-Bb_0(1)]*[.5 .5]';
VB_45   =   [[flipud(Bf_45(2:6));   Bf_225]-Bf_45(1)   [flipud(Bb_45(2:6)); Bb_225]-Bb_45(1)]*[.5 .5]';
VB_90   =   [[flipud(Bf_90(2:6));   Bf_270]-Bf_90(1)   [flipud(Bb_90(2:6)); Bb_270]-Bb_90(1)]*[.5 .5]';
```

```
VB_135 = [[flipud(Bf_135(2:6)); Bf_315]-Bf_135(1) [flipud(Bb_135(2:6));
Bb_315]-Bf_135(1)]*[.5 .5]';
VB_Z = [Bf_Z Bb_Z]*[.5 .5]';
VC_0 = [[flipud(Cf_0(2:6)); Cf_180]-Cf_0(1) [flipud(Cb_0(2:6)); Cb_180]-
Cb_0(1)]*[.5 .5]';
VC_45 = [[flipud(Cf_45(2:6)); Cf_225]-Cf_45(1) [flipud(Cb_45(2:6));
Cb_225]-Cb_45(1)]*[.5 .5]';
VC_90 = [[flipud(Cf_90(2:6)); Cf_270]-Cf_90(1) [flipud(Cb_90(2:6));
Cb_270]-Cb_90(1)]*[.5 .5]';
VC_135 = [[flipud(Cf_135(2:6)); Cf_315]-Cf_135(1) [flipud(Cb_135(2:6));
Cb_315]-Cf_135(1)]*[.5 .5]';
VC_Z = [Cf_Z Cb_Z]*[.5 .5]';
Vxyz = [[VA_0; VA_45; VA_90; VA_135; VA_Z] [VB_0; VB_45; VB_90; VB_135;
VB_Z] [VC_0; VC_45; VC_90; VC_135; VC_Z]];
dx = [d*cos(0); d*cos(pi/4); d*cos(pi/2); d*cos(3*pi/4);0; 0 ; 0; 0; 0; 0];
dy = [d*sin(0); d*sin(pi/4); d*sin(pi/2); d*sin(3*pi/4);0; 0 ; 0; 0; 0; 0];
Kxyz = inv(Vxyz'*Vxyz)*Vxyz';
A = [(Kxyz*[d*cos(0); d*cos(pi/4); d*cos(pi/2); d*cos(3*pi/4);0; 0 ; 0; 0;
0; 0])'; (Kxyz*dy)'; (Kxyz*dz)'];
error_x = sqrt(mean((Vxyz*A(1,:)'-[d*cos(0); d*cos(pi/4); d*cos(pi/2);
d*cos(3*pi/4);0; 0 ; 0; 0; 0; 0]).^2))*1000;
error_y = sqrt(mean((Vxyz*A(2,:)'-dy).^2))*1000;
error_z = sqrt(mean((Vxyz*A(3,:)'-dz).^2))*1000;
disp(['RMS Error (x) = ' num2str(error_x) ' microns']);
disp(['RMS Error (y) = ' num2str(error_y) ' microns']);
disp(['RMS Error (z) = ' num2str(error_z) ' microns']);
subplot(321)
  plot([Vxyz*A(1,:)' [d*cos(0); d*cos(pi/4); d*cos(pi/2); d*cos(3*pi/4);0;
0 ; 0; 0; 0; 0]])
  ylabel('\deltax [mm]');
  subplot(322); plot((Vxyz*A(1,:)'-[d*cos(0); d*cos(pi/4); d*cos(pi/2);
d*cos(3*pi/4);0; 0 ; 0; 0; 0; 0]).*1000);
  hold on;
subplot(323)
  plot([Vxyz*A(2,:)' dy])
  ylabel('\deltay [mm]');
  subplot(324); plot((Vxyz*A(2,:)'-dy).*1000);
  hold on;
subplot(325)
  plot([Vxyz*A(3,:)' dz])
  ylabel('\deltaz [mm]');
  xlabel('Test number');
  legend('Estimated','Measured')
  subplot(326); plot((Vxyz*A(3,:)'-dz).*1000);
```

APPENDIX D

FIRST PROBE TEST RESULTS

The data obtained from tests are plotted in this section. As can be seen from the figures, solid lines indicate the voltage values through 0 º and 180 º, dashed lines indicate the voltage values through 45 º and 225 º, dotted lines indicate the voltage values through 90 º and 270 º and dash-dotted lines indicate the voltage values through 135 º and 315 º.

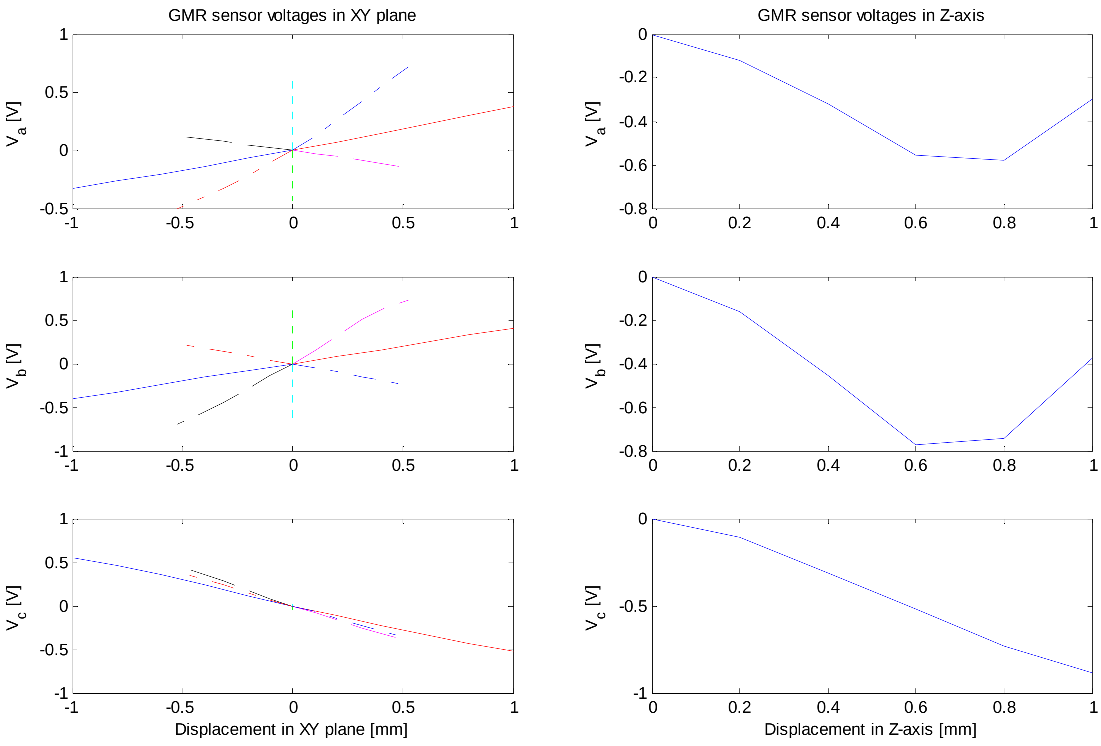

Figure D.1 SS-1(thickness: 0.40 mm) at equator

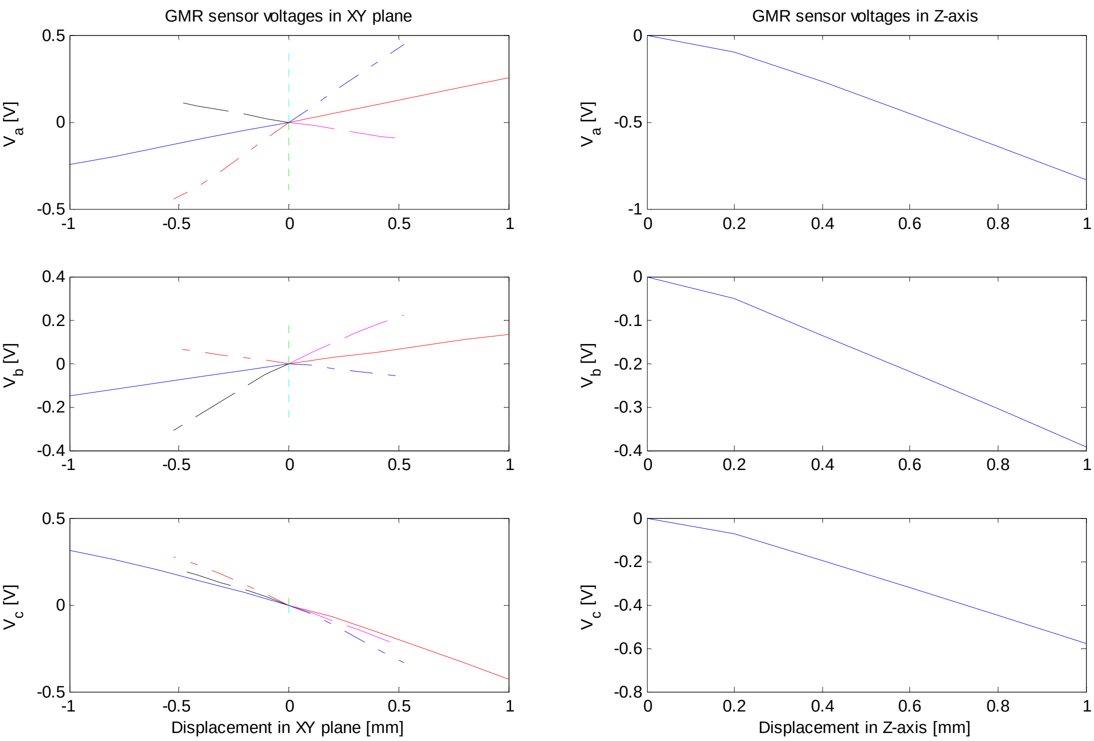

Figure D.2 SS-2(thickness: 0.30 mm) at equator

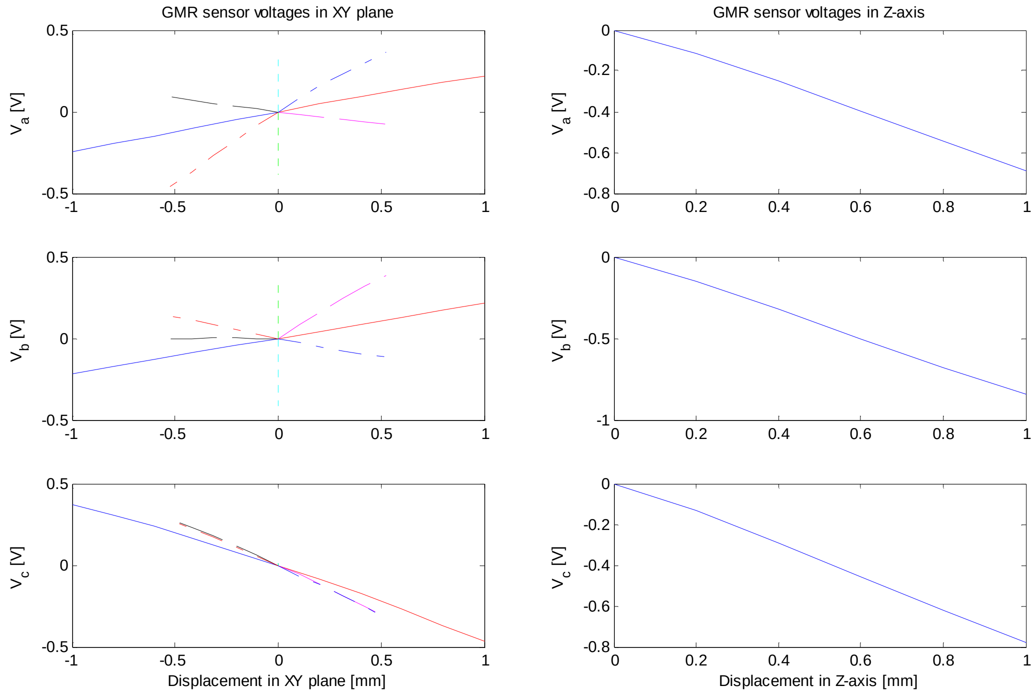

Figure D.3 SS-2(thickness: 0.40 mm) at equator

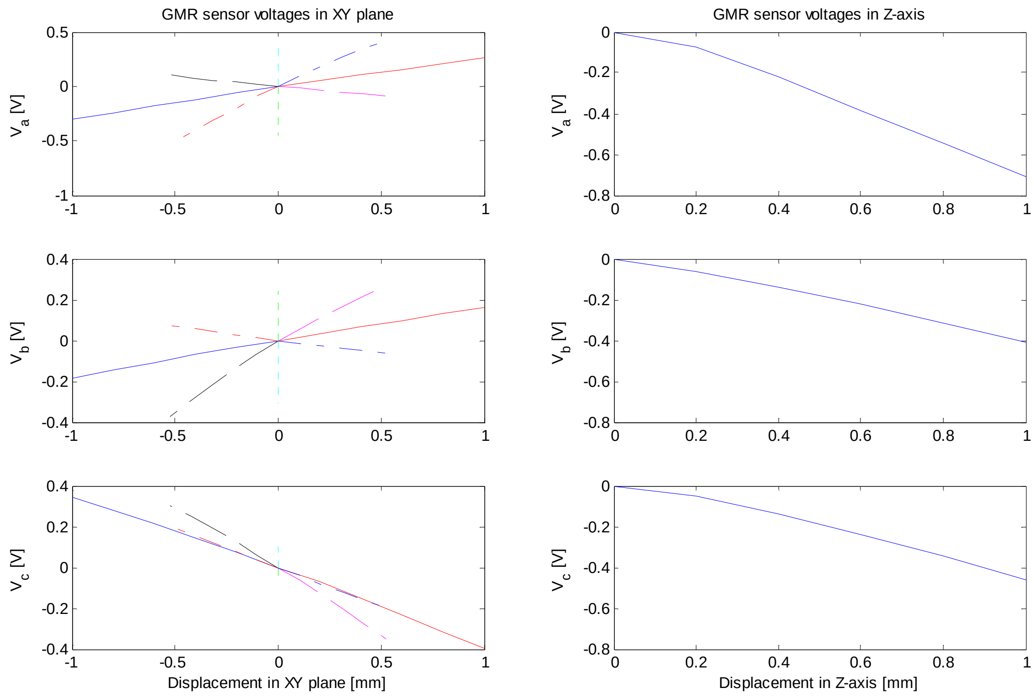

Figure D.4 SS-3(thickness: 0.30 mm) at equator

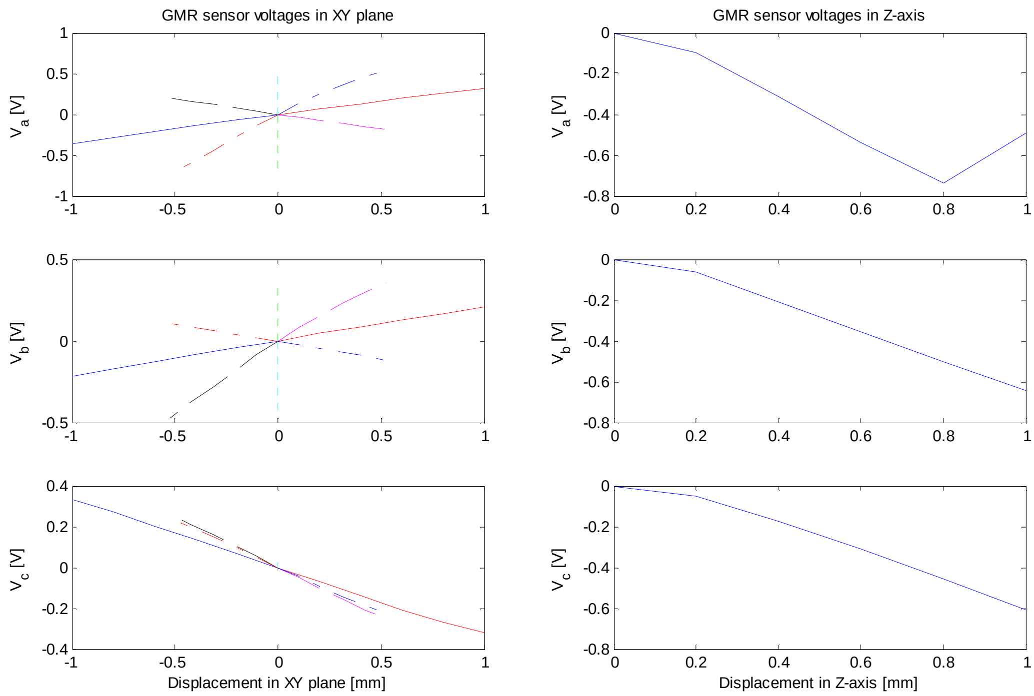

Figure D.5 SS-3(thickness: 0.40 mm) at equator

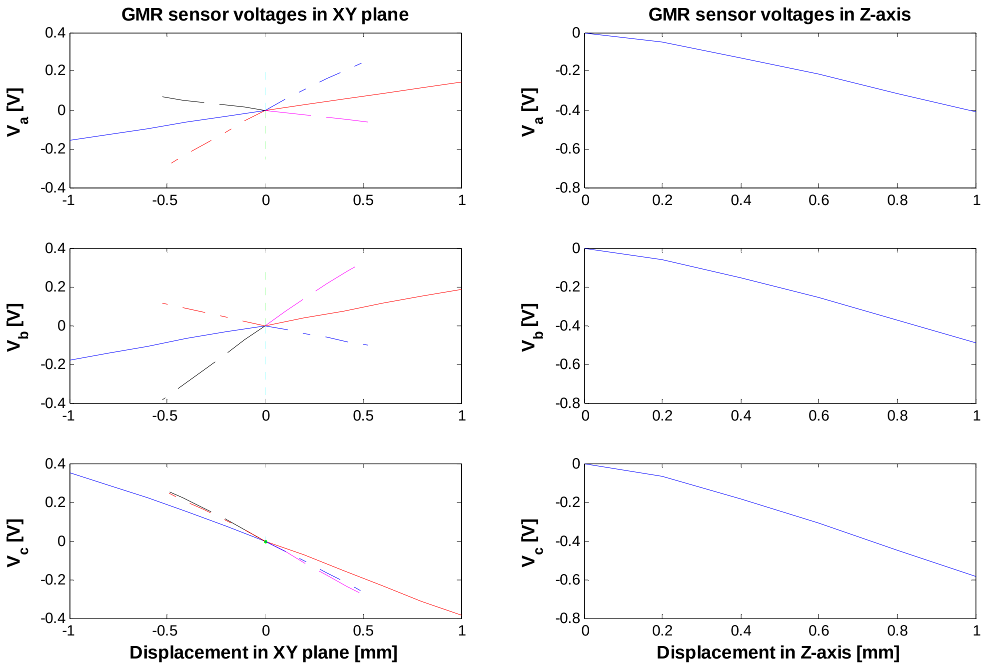

Figure D.6 SS-4(thickness: 0.30 mm) at equator

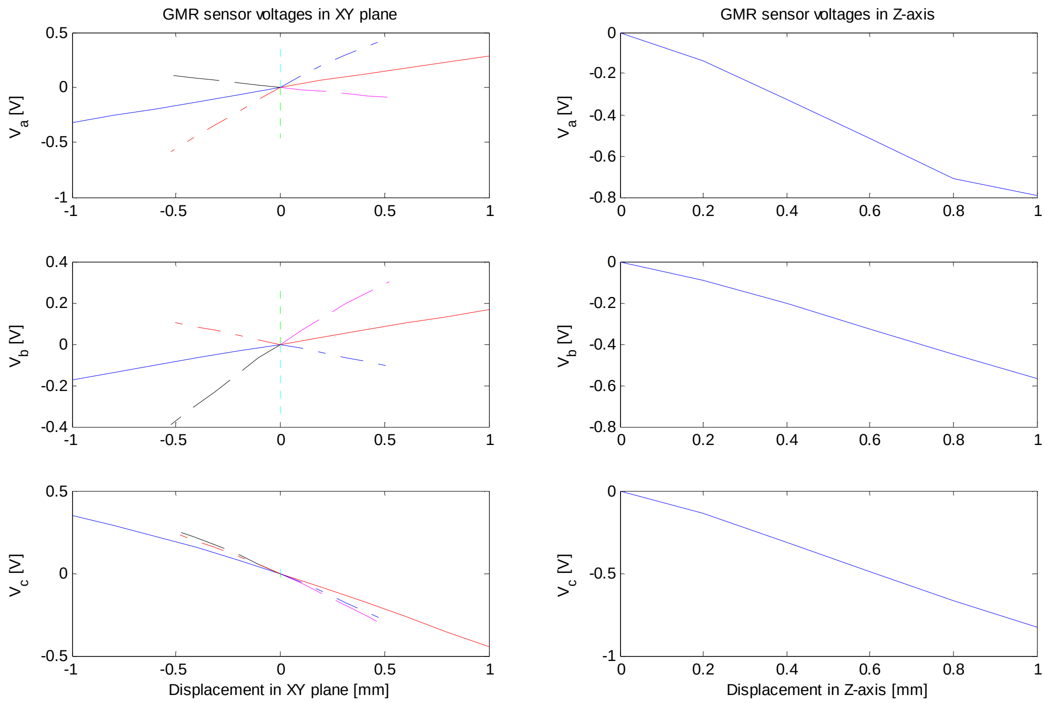

Figure D.7 SS-4(thickness: 0.40 mm) at equator

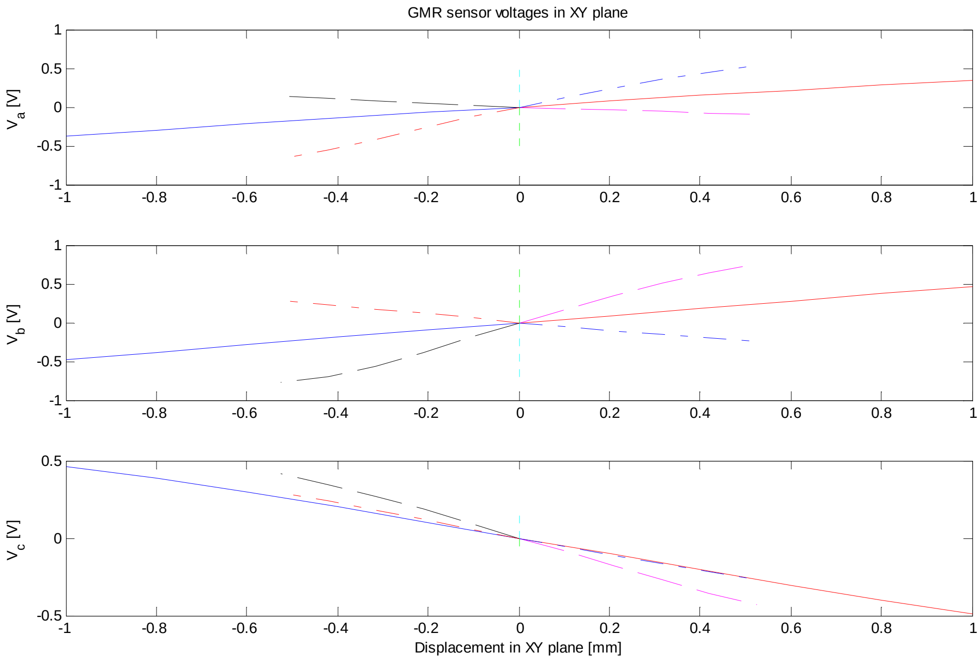

Figure D.8 SS-1(thickness: 0.40 mm) at latitude 22.5 º below equator

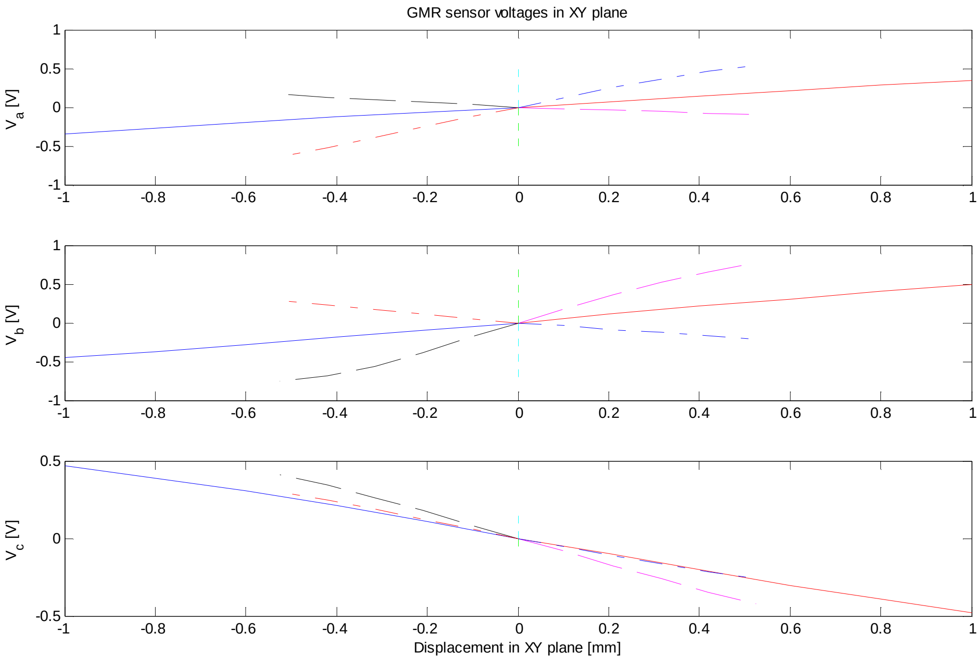

Figure D.9 SS-1(thickness: 0.40 mm) at latitude 45 º below equator

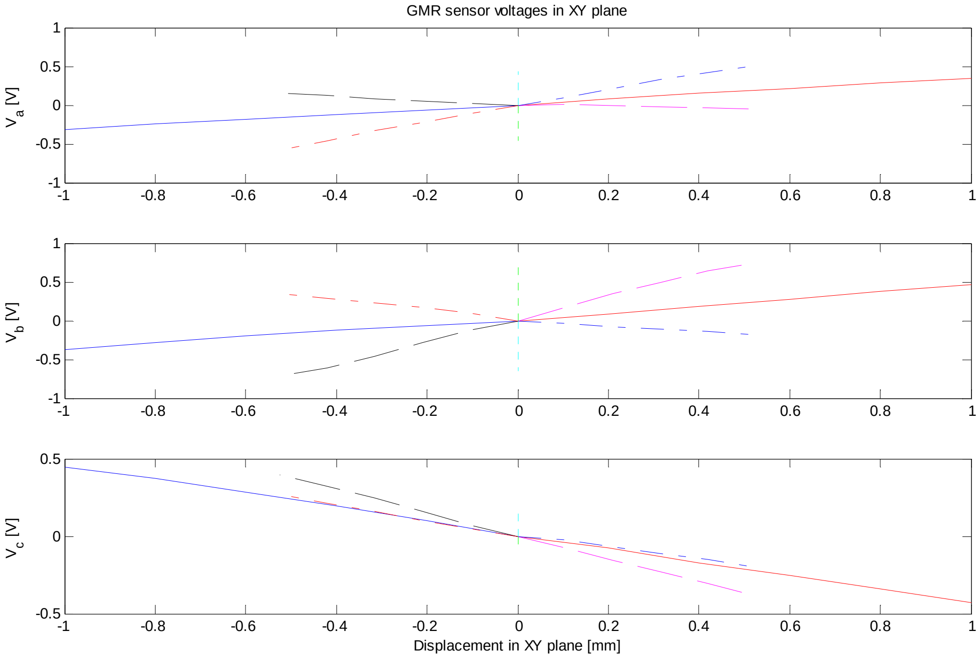

Figure D.10 SS-1(thickness: 0.40 mm) at latitude 67.5 º below equator

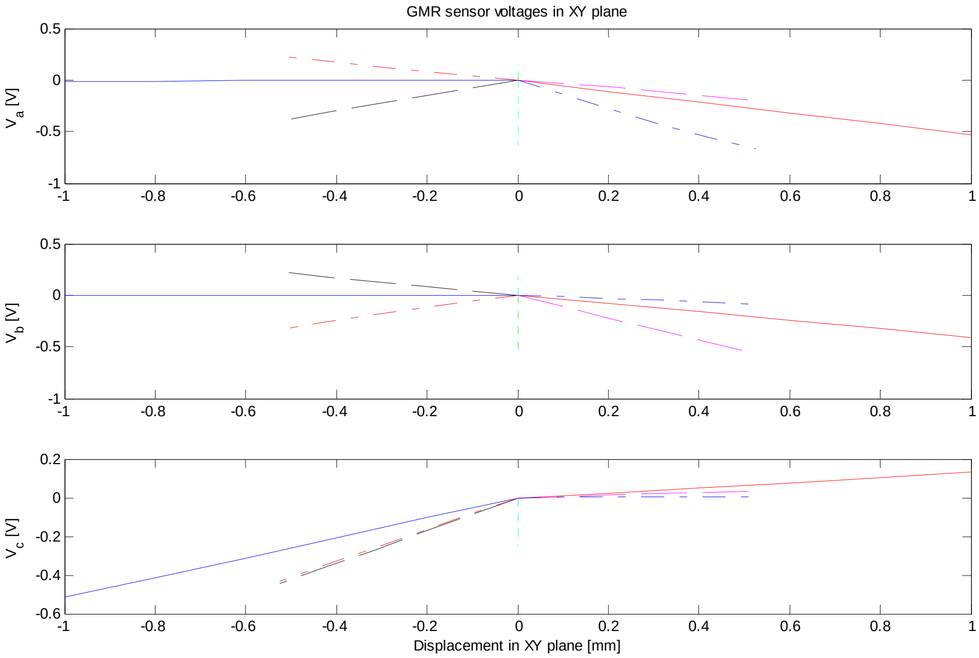

Figure D.11 SS-4(thickness: 0.30 mm) at latitude 22.5 º below equator

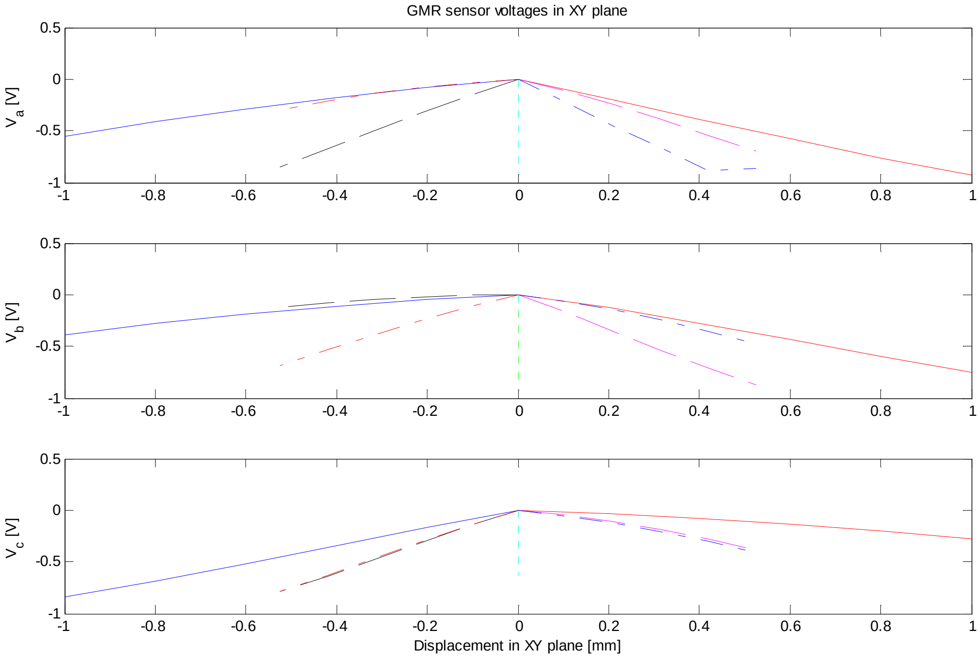

Figure D.12 SS-4(thickness: 0.30 mm) at latitude 45 º below equator

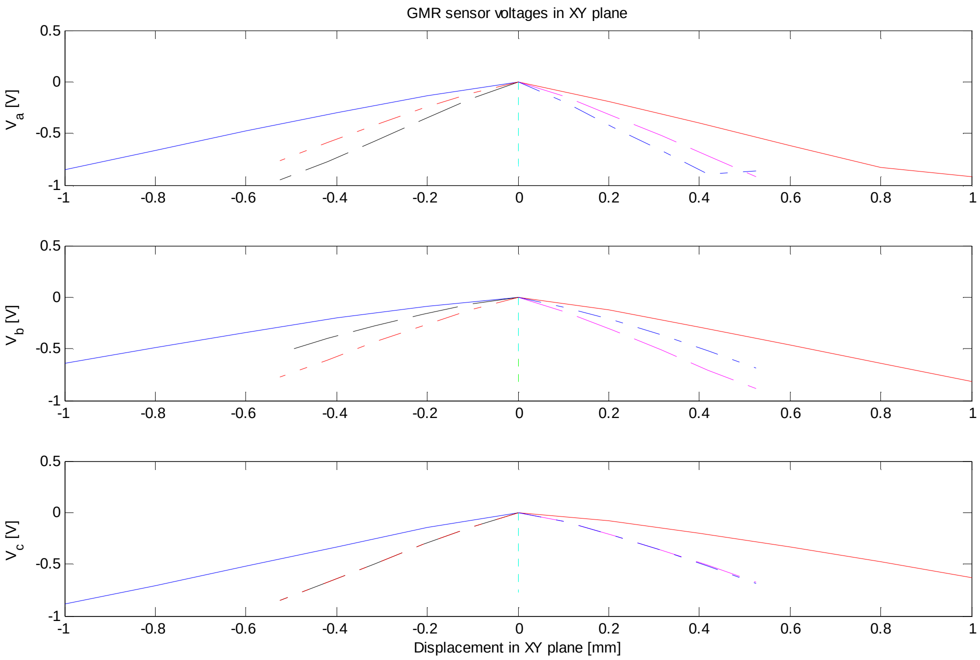

Figure D.13 SS-4(thickness: 0.30 mm) at latitude 67.5 º below equator

APPENDIX E

SECOND PROBE TEST RESULTS

The data obtained from tests are plotted in this section. As can be seen from the figures, solid lines indicate the voltage values through 0 º and 180 º, dashed lines indicate the voltage values through 45 º and 225 º, dotted lines indicate the voltage values through 90 º and 270 º and dash-dotted lines indicate the voltage values through 135 º and 315 º.

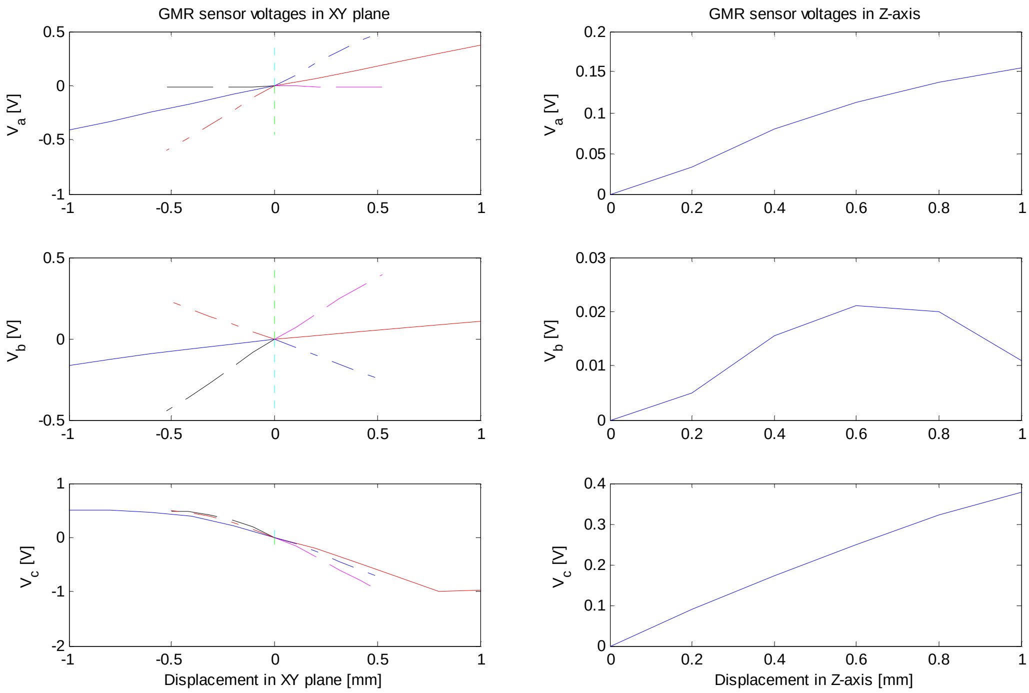

Figure E.1 SS-4(thickness: 0.30 mm) at equator

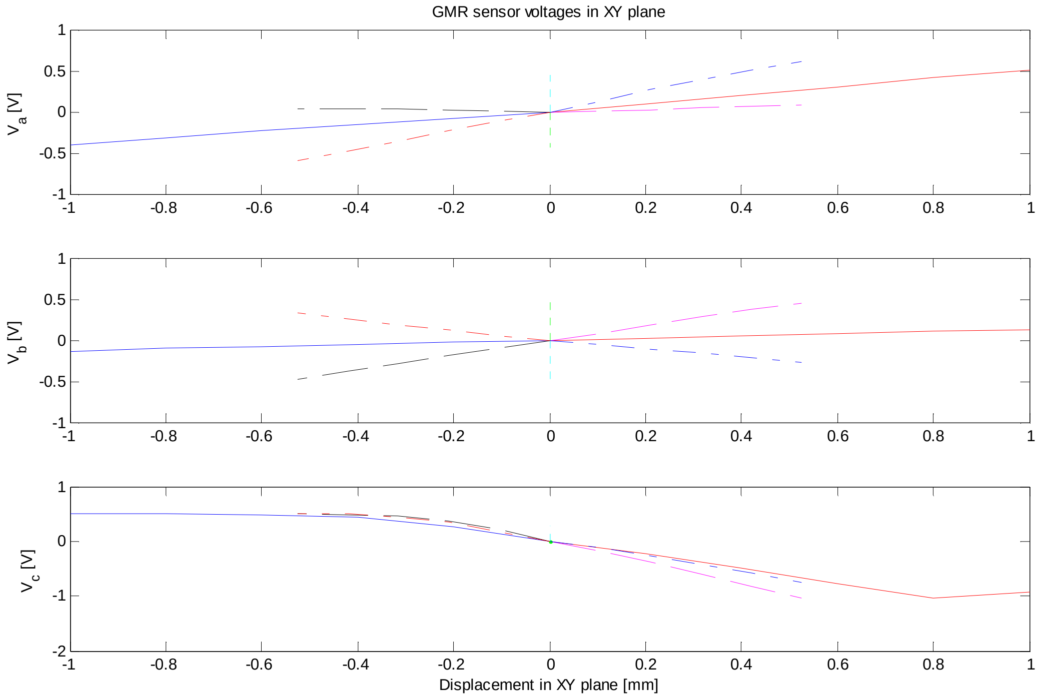

Figure E.2 SS-4(thickness: 0.30 mm) at latitude 22.5 ° below equator

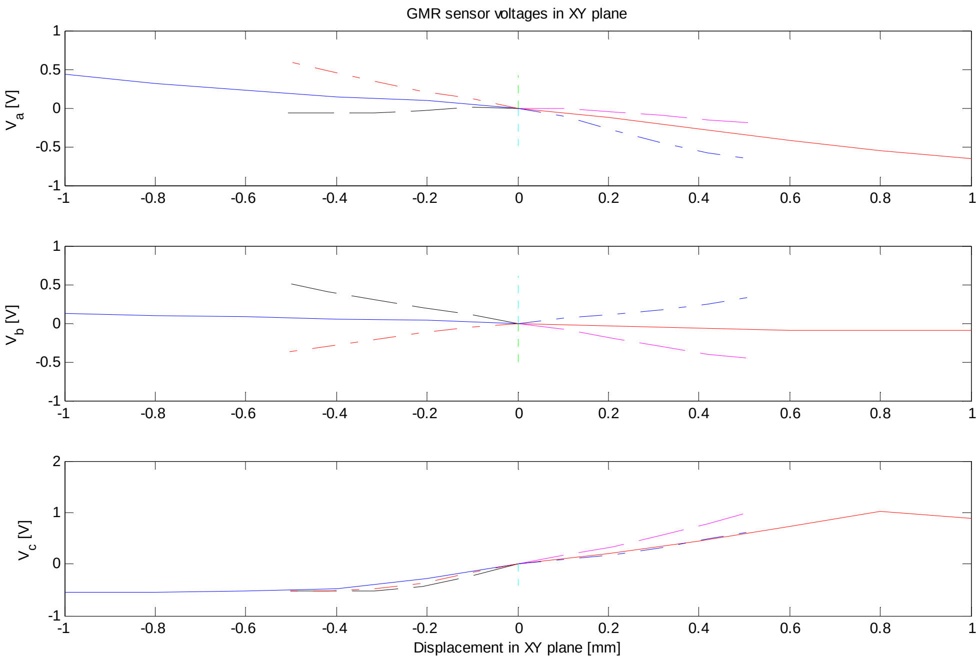

Figure E.3 SS-4(thickness: 0.30 mm) at latitude 45 ° below equator

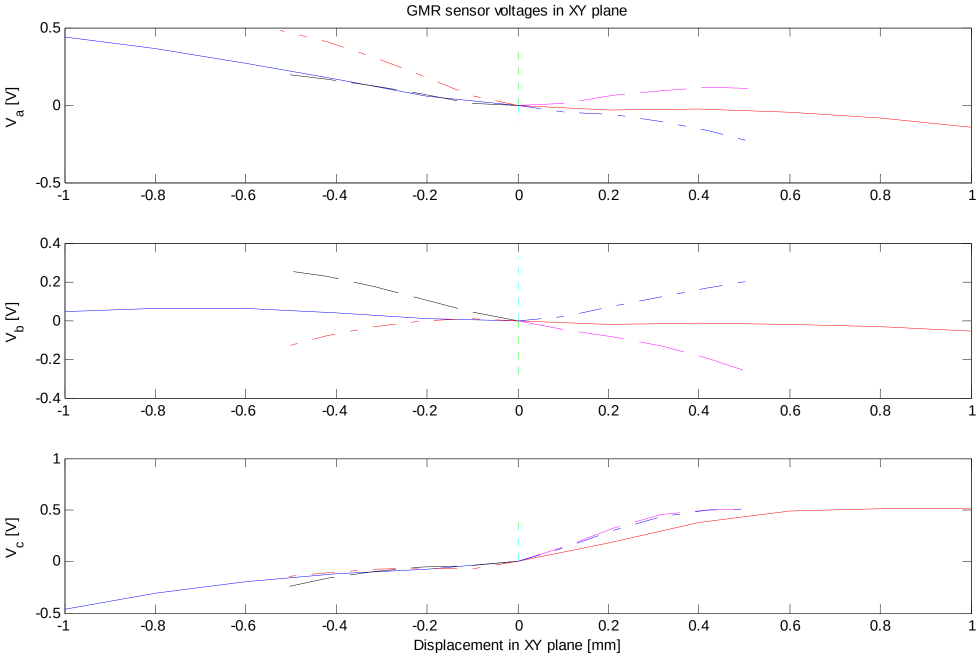

Figure E.4 SS-4(thickness: 0.30 mm) at latitude 67.5 ° below equator

REFERENCES

[1] J. A. Bosch, “Coordinate Measuring Machines and Systems”, Marcel Dekker, Inc., 1995.

[2] Steven D. Bittle and Thomas R. Kurfess, “An Active Piezoelectric Probe for Precision Measurement On a CMM”, Mechatronics, Vol. 7, No. 4, pp 337-354, 1997.

[3] Hales, A. M., “Automated Inspection For Flexible Manufacturing”, Manufacturing Systems, 3(12), 15-19, 1985.

[4] Butler, C., “Investigation into The Performance of Probes on CMMs”, Industrial Metrology , 2(1), 59-70, 1991.

[5] Goh, K. H., Philips, N. and Bell, R., “The applicability of a laser Triangulation Probe to Non-Contacting Inspection”, International Journal of Production Research, 24(6), 1331-1348, 1986.

[6] Somerville, L. and Mudjarred, A., “Laser Adds Light Touch To CMMs”, Machine and Tool Blue Book, 82(4), 55-57, 1987.

[7] Shen Y-L. and Zhang X., “Pretravel Compensation For Vertically Oriented Touch Trigger Probes with Straight Styli”, Int. J. Mach. Tools Manufacts., Vol. 37, No. 3, pp. 249-262, 1997.

[8] Weckenmann A., Estler T., Peggs G., McMurtry D., "Probing Systems in Dimensional Metrology", 54th CIRP General Assembly, Annals of the CIRP Vol. 53/2/2004, Keynote Papers.

[9] Salleh R. M., Yang P. Q., Joners B., "Finite Element Modeling and Simulation of Probe Systems", IMTC 2005 – Instrumentation and Measurement Technology Conference Ottawa, Canada, 17-19 May 2005.

[10] Busch, T., Harlow, R., Thomson, R., L., "Fundamentals of Dimensional Metrology" Delmar Publishers, 1998.

[11] Weckenmann, A., Ernst, R., Geuss, D.A., "Comparability of tactile and optical form measuring techniques with resolution in the nanometer range", Proceedingsof X. International Colloquium on Surfaces, p. 50-62, 2000.

[12] Weisig, S., Koch, K-P.,"Kombinierte optische und mechanische Antastung-erweitert die Einsatzmoeglichkeiten von Koordinatenmessgeraeten" Qualitaet und Zuverlaessigkeit, p. 450-454, 1989.

[13] Yang, Q., Butler, C.,"A 3-D non-contact trigger probe for coordinate measuring machines", Measurement, 17/1, p.39-44, 1996.

[14] Lin, Y-J., Murugappan, P., "A new algorithm for determining a collision free path for a CMM probe", International Journal of Machine Tools and Manufacture, 39/9, p. 1397-1408, 1999.

[15] Pfeifer, T., Zacher, M., Krohne, I., Glaser, U., Frankowski, G., "Einsatzgebiete und Vorteile von streifenprojektionsbasierten Messsystemen, insbesondere durch deren Integration in Koordinatenmessgerate", VDI-Berichte, 1618, p.61-73, 2001

[16] Kunzmann, H., Schaller, M., "Einfluss unterschiedlicher Sensoren auf die Bestimmung von Laengemassen", Technische Messen, 55/9, p. 337-340, 1988.

[17] Renishaw, Technical Article on Touch Triger Probes, http://www.renishaw.com/en/6652.aspx as viewed on 12/2004.

[18] Coleman, D., Waters, F., "Fundamentals of Touch Trigger Probing", Touch-trigger Press. 1997.

[19] Renishaw Touch Trigger Probing Technology powerpoint , http://www.renishaw.com/en/6652.aspx as viewed on 2/12/2007.

[20] Renishaw, www.renishaw.com, as viewed on 20/5/2006.

[21] Renishaw, http://www.renishaw.com/en/6670.aspx, TP 20 datasheet as viewed on 2/12/2007.

[22] Renishaw, http://www.renishaw.com/en/6671.aspx, TP200 datasheet as viewed on 2/12/2007.

[23] Renishaw, http://www.renishaw.com/en/6666.aspx, OTP6M non-contact optical probe system brochure as viewed on 2/12/2007.

[24] David H. Genest http://www.qualitydigest.com/jan97/probes.html, as viewed on 2/12/2007.

[25] Renishaw, http://www.renishaw.com/en/6656.aspx, Renishaw Scanning Technology Powerpoint as viewed on 2/12/2007.

[26] Renishaw, http://www.renishaw.com/en/6686.aspx, SP80 Brochure, as viewed on 2/12/2007.

[27] US 7,146,741 B2 12/2006………… Butter et al.

[28] Laser Design Inc., www.laserdesign.com, CMM laser scanning probe kit document paper, as viewed on 2/12/2007.

[29] Schwenke, H., Härtig, F., Wendt, K., Wäldele, F., "Future Challenges In Co-Ordinate Metrology: Addressıng Metrologıcal Problems For Very Small And Very Large Parts", IDW, Knoxville, May 7-10, page 7/12, 2001.

[30] NVE Corp., www.nve.com, GMR Sensors DataBook April 2003.

[31] G. Binasch, P. Gru¨nberg, F. Saurenbach, W. Zinn, "Enhanced magnetoresistance in layered magnetic structures with antiferromagnetic interlayer exchange", Phys. Rev. B 39, 4828–4830, 1989.

[32] M.N. Baibich, J.M. Broto, A. Fert, F. Nguyen Van Dau, F. Petroff, P. Etienne, G. Creuzet, A. Friederich, J. Chazelas, "Giant magnetoresistance of_001.Fer_001.Cr magnetic superlattices", Phys. Rev. Lett. 61, 2472–2475, 1988.

[33] K.-M.H. Lenssen, D.J. Adelerhof, H.J. Gassen, A.E.T. Kuiper, G.H.J. Somers, J.B.A.D. van Zon,"Robust giant magnetoresistance sensors", www.elsevier.nlrlocatersna, Sensors and Actuators, 85, 1-8, 2000.

[34] IBM Research, http://www.research.ibm.com/research/gmr.html, GMR, as viewed on 2/12/2007.

[35] http://www.wsrcc.com/alison/uxopaper/gmr.html, Physics of the Giant Magnetoresistance, as viewed on 2/12/2007.

[36] Western Digital, www.westerndigital.com, GMR Head Technology; Increased Areal Density and Improved Performance.

[37] http://www.pcguide.com/ref/hdd/op/heads/techGMR-c.html, The PC Guide, Giant Magnetoresistive (GMR) Heads, as viewed on 2/12/2007.

[38] Ling Zhou, EE 698A Advanced Electron Devices lecture Notes, Magnetic Sensors and Logic Gates.

[39] NVE Corp., www.nve.com, Application Notes for GMR Sensors.

[40] Rieger, G., Ludwig, K., Hauch, J., Clemens, W., "GMR sensors for contactless position detection", www.elsevier.nlrlocatersna, Sensors and Actuators A 91, 7-11, 2001.

[41] J.M. Daughton, Y.J. Chen, "GMR materials for low field applications", IEEE Trans. Magn. 29, 2705–2710, 1993.

[42] J.M. Daughton, "Weakly coupled GMR sandwiches", IEEE Trans. Magn. 30, 364–368, 1994.

[43] J. Daughton, J. Brown, E. Chen, R. Beech, A. Pohm, W. Kude, "Magnetic field sensors using GMR multilayer", IEEE Trans. Magn. 30, 4608–4610, 1994.

[44] Infineon Technologies AG, http://www.infineon.com/cms/us/product/index.html, as viewed on 12/2007.

[45] H.A.M. van den Berg, W. Clemens, G. Gieres, G. Rupp, W. Schelter, M. Vieth, "GMR sensor scheme with artificial antiferromagnetic subsystem", IEEE. Trans. Magn. 32, 4624–4626, 1996.

[46] H. Schewe, W. Schelter, “Industrial applications of magnetoresistive sensors”, Sens. Actuators, A 59, 165–167, 1997.

[47] H.A.M. van den Berg, W. Clemens, G. Gieres, G. Rupp, M. Vieth, J. Wecker, S. Zoll, “GMR angle detector with an artificial antiferromagnetic subsystem AAF”., J. Magn. Magn. Mater., 165, 524–528, 1997.

[48] W. Clemens, H.A.M. van den Berg, G. Rupp, W. Schelter, M. Vieth, J. Wecker, “Contactless potentiometer based on giant magnetoresistance sensors”, J. Appl. Phys. 81, 4310–4312, 1997.

[49] J.K. Spong, V.S. Speriosu, R.E. Fontana Jr., M.M. Dovek, T.L. Hylton, “Giant magnetoresistive spin valve bridge sensor”, IEEE Trans. Magn. 32, 366–371, 1996.

[50] P.P. Freitas, J.L. Costa, N. Almeida, L.V. Melo, F. Silva, J. Bernardo, C. Santos, “Giant magnetoresistive sensors for rotational speed control”, J. Appl. Phys. 85, 5459–5461, 1999.

[51] Giebeler, C., Adelerhof, D.J., Kuiper, A.E.T., Van Zon, J.B.A., Oelgeschlager, D., Schulz, G., “Robust GMR sensors for angle detection and rotation speed sensing”, www.elsevier.nlrlocatersna, Sensors and Actuators A 91, 16-20, 2001.

[52] Rhopoint Components Ltd., www.rhopointcomponents.com, Magnetic Sensors, GMR Application Notes.